Mass Transfer and Structural Analysis of Microfluidic Sensors

by

Thomas Gervais

B.Eng., École Polytechnique de Montréal, 2000

Submitted to the Department of Biological Engineering in partial fulfillment of the requirements
for the degree of

Doctor of Philosophy

at the

Massachusetts Institute of Technology

[February 2006]

September 2005

Author...
Thomas Gervais
Department of Biological Engineering
September 6, 2005

Certified by...
Klavs F. Jensen
Lammot DuPont Professor of Chemical Engineering
Professor of Materials Science and Engineering
Thesis Supervisor

Certified by...
Peter K. Sorger
Professor of Biology and Biological Engineering
Thesis Co-supervisor

Accepted by...
Alan J. Grodzinsky
Professor of Mechanical, Electrical and Biological Engineering
Thesis Chairman, Committee of Graduate Students

Mass Transfer and Structural Analysis of Microfluidic Sensors

by

Thomas Gervais

Submitted to the Department of Biological Engineering on August 10, 2005,
in partial fulfillment of the requirements for the degree of
Doctor of Philosophy in Biological Engineering

Abstract

Surface-based sensors take advantage of the natural high surface-to-volume ratios in microfluidic devices, low reagent consumption and high potential for integration in more complex micro total analysis systems (microTAS or μTAS). This thesis studies the fundamental limits of on-chip integrated microfluidic sensors. More specifically, it focuses on detection methods involving surface interaction in channels with thicknesses on the order of a few microns or less.

Through mass transfer analysis, we demonstrate that, for thin enough channels, sample detection is limited by the convective transport of analytes, and neither by diffusion nor reaction. The results provided extend the validity of transport models to include transport in the absence of mass transfer boundary layer. All existing analytic solutions to the Graetz problem are described and compiled. The analysis, complemented by finite element simulations, successfully predicts experimental observations made for on-chip immunoassays in micron-thick fluidic channels.

Subsequently, our study of on chip detection systems is carried on with emphasis on resonating cantilever sensors. In order to interpret the output signal from these devices, we develop a dynamic cantilever model to link spatially and temporally dependent mass adsorption with resonance frequency change. The mass adsorption is then directly related to the sensors' operating conditions via the mass transfer models previously developed. We then develop a 2D finite-element model capable of predicting the devices response and of extracting bimolecular rate constants.

Finally, since hydraulic resistance severely increases as channels get shallower, we provide a structural analysis of polymer-based microsystems. Through scaling and numerical simulations we demonstrate the effect of channel deformation on the flow conditions inside the device and vice versa. Finally, channel deformation is experimentally quantified using optical methods and compared with the models developed.

Throughout this thesis, the approach to physical modeling has been to use mathematical and numerical analysis as predictive tools in the design of integrated lab-on-a-chip systems. Whenever possible, scaling and analytic solutions are developed, since they provide a direct relationship between experimental observations, geometry and the multiple dependent variables in the system, and can be readily used as design criteria by the experimentalist.

Thesis Supervisor: Klavs F. Jensen
Title: Lammot du Pont Professor of Chemical Engineering and Professor of Materials Science and Engineering

Thesis Co-supervisor: Peter K. Sorger
Title: Professor of Biology and Biological Engineering

Thesis committee chair: Alan J. Grodzinsky
Title: Professor of Electrical, Mechanical and Biological Engineering

Acknowledgement

Early in my PhD experience, my advisor, Klavs Jensen, asked me whether I would want to pursue a career in Academia or Industry, and provided an insightful view of the important difference in skills that each of the two main PhD career tracks require. Having answered strongly in favor of Academia, he helped over the following years shape my malleable scientific mind into the one of a thinker and a problem-finder, beyond that of a problem-solver. In the process, his integrity, his respect for his student's scientific liberty, and his constant care for our personal well being have filled me with admiration.

To support Klavs' work, my committee members, Peter Sorger and Alan Grodzinsky, have provided me with much needed personal and scientific support. Al's innate pedagogical talent and Peter's eloquence as a public speaker will continue to inspire me throughout my life as a communicator.

For the technical aspects of my thesis, I could rely on the experimental support of Prof. Scott Manalis and his talented research group. Dr. Christine Tsau provided an invaluable support in experimentally confirming many of my predicted theoretical results. Thomas Burg's excellent work on resonating cantilevers became the cable that grounded my work into meaningful technological applications. Dr. Suzanne Gaudet and Dr. Ulrik Nielsen, from the Sorger lab, have been my principal sources of help on all matters in molecular biology.

The process of scientific research is that of a long series of failures punctuated by occasional success. To celebrate the successes, but mostly to help cope with the frustrations of daily failures, I could rely on the supportive work and friendship of the members of the Jensen Group. Dr. Jamil El-Ali served the double role of a skilled experimentalist and a great friend with whom working became simple and natural. Dr. Hang Lu became my informal graduate mentor. Axel, Nicolas, Nuria, Andrea and many others made me laugh like I would not have expected from work colleagues. It has been a pleasure to work with all of them.

To recognize herein all the people that I will be remembering with fondness from my MIT years is absolutely impossible, yet there are some people that simply cannot go unnoticed: Moving in with Jan De Mot was one of the best decisions of my PhD experience. His constant support and our deep connection made me grow up as a person. Ale Wolf-Yadlin will remain to me as a model of trust and kindness in friendships, without forgetting his inspirational dribbling skills in soccer. Meeting Molly Stevens was the key to a whole network of long lasting friendships. Maxine Jonas and Helene Karcher helped me renew with my French roots. I was happy to share my passion for cinema and novels with the cultivated minds of Alex Salcianu, Ji-Eun Kim, Frédéric Rochon, and Cansu Tunca. I will remember all of you with fondness.

Un grand merci à mes amis Québécois avec qui j'ai pu partager les petits détails si importants qui nous unissent : Tymon Barwicz, Benoit Charbonneau, Ariane Verdy, à mes Aminches de toujours et à bien d'autres.

Finally, I want to dedicate this thesis to all those who are born gifted but for whom poverty, combined with cast-like elitism, deprives the world of their hearts and intellects: to my parents and family.

The work contained in this thesis has been funded by the NIH, and the Governments of Québec (FCAR) and Canada (NSERC).

Table of Contents

List of Figures

List of Tables

List of Abbreviations and Symbols

Parameters

A	Cross section Area
c	Constant
C	Concentration
D	Diffusivity
Da	Damköhler number (surface-bimolecular)
E	Young's Modulus
e	Strain
f	Capture fraction (or frequency)
F	Force
Gr	Graetz number
i	Index variable
I	Area moment of inertia
h	Channel height
H	Heaviside function
j	Imaginary number
k	Rate constant (spring constant)
K	Equilibrium constant
l	Characteristic length
L	Length (stream wise) dimension
m	Mass
M	Kummer Function (or Mass)
n	Number (or normal unit vector)
N	Mass Flux
p	Pressure
Pe	Péclet number
Q	Volumetric flow rate
r	Resistivity
R	Reaction Rate
Sh	Sherwood number
t	Time
u	Normal unit vector
U	Average fluid velocity
V	Shear force
v	Velocity
W	Channel width (Bending Work)
x	Height position variable
y	Lateral position variable
z	Axial position variable

Greek Letters

α	Deformation fit parameter
β	Linear mass distribution
γ	Dimensionless sensor sensitivity
δ	Boundary layer Thickness (or Dirac delta function)
Δ	Differential variation symbol
ε	Volume-to-surface concentration ratio
ζ	Convective/diffusive Length scale
η	Normalized height
Θ	Normalized Concentration
κ	Spatial resonance frequency
λ	Eigenvalue
μ	Dynamic viscosity
M	Bending moment
ν	Poisson's ratio
ξ	Moving front variable
ρ	Mass density
σ	Standard deviation
τ	Normalized time
ω	Resonance frequency
Ω	Resonance energy

Superscripts/Subscripts

0	Initial
a	Analyte
acc	Acceleration
$asym$	Asymmetric
b	Bulk
c	Convection
$crit$	Critical
d	Diffusion
D	Dissociation
d/r	Diffusion/reaction
E	Entrance
eq	Equilibrium
eff	Effective
FD	Fully Developed
k	Kinetic
h	Hydraulic
L	At position z=L
max	Maximum
min	Minimum
off	Reverse (to bulk)
on	Forward (to surface)
p	Propagation
r	Reaction
s	Surface (or strain)
sat	Saturation
sym	Symmetric
v	Volume
w	Wall

Mass Transfer and Structural Analysis of Microfluidic Sensors

Chapter 1. General Introduction

1.1. Science Fiction on a Chip

It was a routine check-up like the ones healthy people perform every month. I lay my thumb on the healthcare module's sampling system connected to my computer, which painlessly withdraws a few blood droplets for analysis. Seconds later, my computer screen displayed the state of my hemostasis: red and white blood cell count, iron and glucose levels, hormones and cytokines levels, gene markers, all within normal physiological range. "I am in much better health than I used to be", I surprised myself voicing out loud.

Three years ago, these short diagnosis moments were not as easy to perform as today, and each measurement bore important emotional consequences for my family and myself. The few seconds spent by the device to separate the vital fluid into its cellular and molecular components and later to analyze them using a complex array of microsensors had turned into long, angst-ridden minutes. Back in these days, an abnormal increase in the activity of certain signaling peptides had started to appear in my blood serum. By comparing my personal data with the public health databases, I knew that these changes could bear the unfortunate omen of a genetic disease, perhaps cancer. After a visit to the hospital for further testing, I was diagnosed with an early, not yet visually observable, form of skin cancer and compelled to begin biochemical *treatments to fend off the disease while in its infancy. The frequency of my home-based check-ups was increased to once per week to monitor the effect of the medicine on my remission and results were directly communicated to my physician.*

Fortunately for me, the treatment was successful and, after a few months, I no longer observed on my computer monitor the worrisome signs of a potential genetic ailment. Everything for the moment seems to be all right. My only concern is that, with the abundance of information on my own body so rapidly available, I am wondering whether I am not becoming a little hypochondriac…

1.2. Systems Biology and Point-of-Care Analysis

No one has yet written a science fiction novel based on the technological breakthroughs provided by Lab-on-a-chip science, but many researchers have envisioned futuristic scenarios similar to the ones described above[*1-3*]. The commercialization of a portable healthcare module that can be linked to one's computer for the rapid, point-of-care analysis of biological samples would revolutionize the way medicine is practiced. In a way analogous and complementary to the sequencing of the human genome, portable bioanalytical systems, would contribute to transform biology from an empirical science to a holistic, information-based science where more attention is given to prevention and diagnosis rather than to hospitalization and treatment[*4*].

Even if the actual computer-based diagnostics device described above has yet to be realized, the identification of signaling peptides (cytokines) and proteins in human serum linked to skin cancer development remains, nevertheless, a real recent scientific discovery[*5*]. In general, advances in molecular and systems biology (i.e. the study of extra and intracellular communication leading to the emergence of systemic biological behaviors[*6, 7*]), bring to our attention many examples of diseases caused by the deregulation of intracellular signaling pathways at specific nodes[*8, 9*]. Most of the time, these nodes correspond physically to a key protein-protein interaction -such as the dimerization of a protein complex, kinase phosphorylation events, or protein-inhibitor/activator interactions[*10*]- for which a perturbation of its steady state leads to important consequences in the outcome of a cell decision process. They possess a high impact on cellular outcome and are therefore ideal parameters to monitor in an individual to diagnose certain diseases. For the same reasons, they are the points on which pharmaceuticals must act to cure a given ailment, thus playing a crucial role in drug development. For example, in colon cancer treatment, the binding of Tumor Necrosis Factor cytokine (TNF-α) at the cellular membrane is known to induce programmed cell death (apoptosis) [*11, 12*]. However, under certain circumstances, apoptosis can be inhibited by the joint effect of insulin in a complex, highly interconnected signaling cascade (Fig. 1.1). Monitoring the activity in time of critical protein kinases in this signaling pathway has provided insights in treating the side effects of colon cancer treatments[*13*].

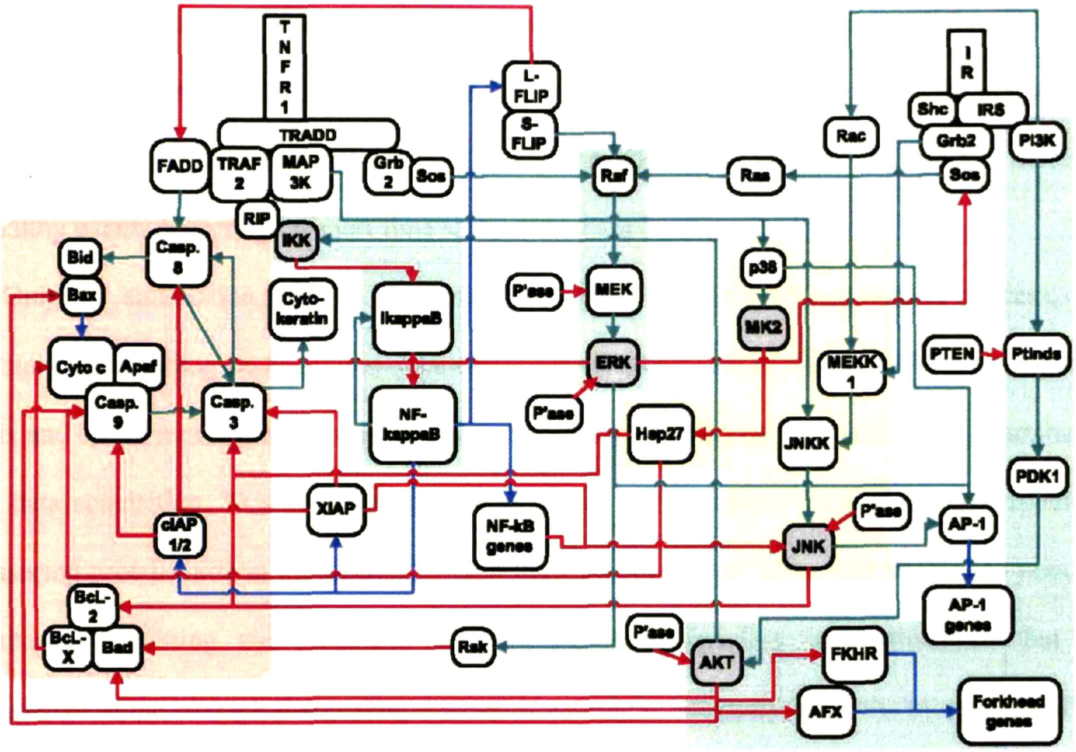

Figure 1.1: Example of systems biology network: A high-throughput assay of multiple endogenous kinase activities can monitor information flow through critical nodes in a signaling network. A, generalized network diagram describing pathways activated downstream of TNF-α and insulin: activating interactions (green arrows), inhibitory interactions (red arrows), transcriptional interactions (blue arrows). Gray nodes highlight kinases that are measured by the high-throughput multiplex kinase activity assay. Red regions indicate apoptotic pathways, green regions indicate survival pathways, and orange regions indicate stress pathways that can function to promote or inhibit apoptosis, depending on context. Note the extent of crosstalk in the network. Diagram is not implied to be comprehensive (e.g. location-dependent interactions have been abstracted). Courtesy of K.A. Janes.

One of the greatest challenges in getting access to this point-of-care information is the development of integrated devices that can perform rapid analysis of biological samples. Currently, the development of systems biology is limited by the intrinsic difficulty in acquiring data on protein abundance, activity and kinetics of interactions in signaling pathways. Western-blots, an immunoassay technique used to obtain data on protein concentration and activity in cells is the gold standard in proteomics. However, the method is slow and tedious, due mostly to the lack of automation of the process (performed manually by the biologist), and thus limits the amount of data generated (on the order of a few dozen data points over a week-long period[*14*]). The method not only limits the number of data points but also acquisition of time data series on signaling events occurring on short time scales (less than 5 minutes) [*15, 16*].

Only by automation, thereby increasing the speed of the data acquisition process, will physicians and biologists be able to obtain information on a given system at will, on a per patient basis and spend more of their work hours on diagnosis or data analysis rather than examination and data acquisition. This goal requires effort in two distinct areas. First, detectors capable of measuring protein-protein interaction kinetics must be developed. They will be used to populate databases containing the properties of protein-protein signaling interactions so that our knowledge of the biological signaling systems is complete. Secondly, once the biophysics of cell signaling processes is known, there will be a need for another kind of detectors capable of performing point-of-care analysis in a particular individual in real time.

1.3. Total Analysis Systems and Lab-on-a-Chip

In genomics and proteomics research, automated processes already exist and are commercially available in the form of liquid handling and sample preparation robots (Qiagen Inc., Valencia, CA, SSI Robotics, Tustin, CA), arrayers to either prepare DNA chips (ESI, Toronto, ON) or immunoassays (BioRobotics Inc. Woburn, MA). Robotics has produced significant progress in the field, but the solutions they propose are often nothing more than automation of the manual work that a biologist would perform in the lab. The throughput increase made by robots is thus only attributed to the higher precision and ability to perform repetitive tasks rapidly. A lot of room is left for optimization.

In the eighties, with the breakthrough in miniaturization science and microelectronics, engineers and scientists realized that silicon-based technologies could also be used to create sensors and actuators, known as Microelectromechanical Systems (MEMS) [*17*]. The advances in miniaturization and silicon processing also bore fruit in chemistry and chemical engineering. On-chip chromatographic columns were among the first on-chip analytical tools developed[*18, 19*]. It was quickly envisioned that the techniques of microfabrication could be used to generate devices in which rapid analysis of chemical and biological reactions can be performed and the concept of micro Total Analysis System (μTAS) was introduced by Manz[*20*].

Building chemical and biological analysis systems on chip possesses several advantages, notably that devices can directly be integrated with microelectronic circuits for continuous data acquisition and analysis. Other advantages stem from the devices' small size, such as higher efficiency, faster analysis and lower reagent consumption[*21*]. At the microscale, heat and mass transfer are also enhanced due to decreased diffusion and heat conduction length scales[*22*].

As the concept of μTAS evolved, highly creative thinking in the community expanded its premises to include on-chip cell culture, sample preparation, reagent production, and delivery to form an integrated device capable of emulating the work performed by an entire laboratory on a single chip[*23*](Fig. 1.2).

Figure 1. 2: Schematics of an integrated μTAS. The system consists of several integrated sample preparation modules, such as cell culture, cell lysis, protein and organelle separation, followed by a detection module located downstream of the processing cascade. The arrow represents the order in the process. Even though the process described here is linear, μTAS are not limited to linear systems and allow the parallelization of assays for higher throughput or more complex functions.

1.4. Microfluidics: Thinking Inside the Box

Since a large part of the chemical sciences and the whole of biology is essentially liquid-based, all lab-on-a-chip prototypes rely on more or less complex miniature plumbing networks to carry samples to and from the detection zone rapidly, to branch out in a separation process or merge to mix two reagents together. Furthermore, flow in sub-millimeter fluidic channel networks is completely dominated by viscous forces[*24*], thus imposing limits and creating opportunities for applications which are different from their macroscale counterpart. At such small scales, turbulence does not occur, making the mixing of two fluid streams running side-by-side diffusion-controlled -a slow process[*25, 26*]. On the other hand, one can take advantage of such immiscibility to separate biological components into different streams and carry them towards different analysis modules on the same chip[*27*].

The need for a technological toolbox to address these issues in a reliable way gave birth to the field of microfluidics: the ensemble of science and technology enabling fluid routing and control in sub-millimeter channels in an integrated fashion to perform various analytical tasks[*28, 29*]. Among these tools, the development of polymer-based lithography –or soft lithography- has brought microfabrication outside the clean rooms and into the chemistry and biology labs[*30-32*]. The elastomer of choice in most applications is poly(dimethylsiloxane) -or PDMS- due to its transparency, biocompatibility, ease of sealing, and affordability[*33*]. It's high elasticity enabled scientists to use it to build valves and pumps[*34*], as well as to realize applications that were not possible using conventional silicon machining[*35, 36*].

1.5. Surface Properties and Surface-based Sensing

Another singular characteristic of microfluidic systems is the high importance of surface interactions on device properties. Fluid flow in microdevices has been observed to be extremely dependent on surface hydrophilicity[*37*]. Surface properties possess even higher impact on chemical transport and reactions performed in microfluidic channels. Surface functionalization, either to prevent protein and cell adsorption or to selectively enhance it, remains one of the greatest challenges in engineering reliable μTAS[*38-42*].

One of the most important applications of surface control is to develop highly sensitive protein detectors. In microfluidics devices, surface-based detectors are the most common and practical form of sensors since they take advantage of the high surface to volume ratios present in microchannels. Consider the following example as an illustration of the importance of surface interactions: a tube-shaped sensor possesses a surface concentration of 10^4 receptors per square micrometer (a common number for proteins) while a solution of 1μM (600 molecules per cubic micron) of analyte (i.e. the molecule susceptible to bind to the receptor) flows over the surface. In a 50 μm-wide capillary, the diameter of a human hair, the number of surface receptors available per analyte molecules amounts to 1.3. Reducing the diameter to 1μm increases the number of receptors available per analyte to 67.

As the channel diameter decreases, any analyte in a random distribution becomes statistically much closer to the wall, thus increasing the potential of interaction, be it desirable or not. Outside the sensor region, one would try to minimize surface interaction with the analyte, as non-specific adsorption leads to sample depletion and therefore decreases the achievable signal-to-noise ratio in sensors located downstream. On the other hand, when designing a sensor surface, it is desirable to maximize the surface's adsorptivity to a selected analyte to improve signal.

1.5.1. On-chip protein detectors

The challenge of measuring the concentration of analytes in an integrated fashion is at the core of the microfluidic science. Without highly sensitive and reliable detectors, computer healthcare modules such as the one described in section 1.1 cannot be realized. In an ideal world, the quintessential on chip sensor would possess the following characteristics:

1- It can selectively detect small amounts of analytes dispersed in a sample containing several thousand types of molecules in various states, such as in a typical cell lysate;
2- It must be either fully reusable or cheap and disposable, and the surface properties between detectors must be constant and reproducible;
3- It possesses a high time resolution allowing the measurement of kinetic rate constants between receptor and analyte;
4- It is built and operated in such a way that mass transfer limitations are minimized, meaning that the amount of time required by an analyte to reach sensing region is much smaller than the time for the analyte to react with the surface.

Creative bioengineering solutions are being developed to approximate the ideal detector described above. The most common methods are summarized briefly in the following sections.

a) On chip Immunoassays

Taking advantage of the naturally evolved selectivity of the human immune system, immunoassays are by far the most commonly used and selective method to detect a given biomolecule. They were essential to the development of Western blotting techniques[*14*], immunoprecipitation[*43*] and enzyme-linked immunosorbent assays (ELISA) [*44, 45*] assays. They can be conveniently integrated on-chip by immobilizing antibodies onto the channel walls and running a sample containing its corresponding antigen[*46*]. The technique's main disadvantage is that antibodies must be developed for every target of interest. Immunoassays do not provide direct sample detection but only sample retention. The technique must therefore be coupled to an existing sensing method as described below.

b) Fluorescence-based detection

Perhaps the most commonly used detection techniques, fluorescence-based immunoassays lend themselves well to miniaturization. They provide sensitivities well into the picomolar range[*47*] and can be integrated on-chip in array format[*46*]. Their main drawback is that detection requires the fluorescence labeling of the detected molecule. Whenever measurements are made on real biological systems (e.g. protein detection using cell lysates), the labeling of the detected antigen is not possible and a third labeled antibody must be used to perform detection. Even though this type of sandwich immunoassays (antibody-antigen-fluorescent antibody) is highly sensitive[*48*], it introduces an extra detection step, thus increasing the complexity of any on-chip assay. For that reason, label-free techniques (see below) are often preferred. Other light-emitting detection methods include chemiluminescence and bioluminescence assays [*49*], quantum-dots labeling[*50, 51*], and Fluorescence Resonant Energy Transfer (FRET) assays[*52*].

c) Surface Plasmon Resonance and Other Optical Sensing Methods

Other detection methods monitor the change of optical properties of materials with protein adsorption[*53*]. Using this principle, researchers in the μTAS community have developed evanescent waveguides sensitive to the amount of protein mass deposited on its surface[*54, 55*]. Grating couplers have also been developed for sensitive biomolecular sensing[*56, 57*].

Among all optical detection methods, the most commonly used and well characterized device is the surface plasmon resonance (SPR) sensor [*58*]. The physical principle underlying molecular sensing is the change in resonance energy of surface electrons in thin gold films due to mass adsorption[*59*]. Typical sensor cells are 50 μm thick by 2 mm long, and the fluid velocity used on the order of fractions of meters per second to avoid mass transfer limitations. Commercially available SPR sensors (Biacore Inc., Uppsala, Sweden) report mass sensitivity on the order of 1

pg/mm^2 (<1 $femtomol/mm^2$ for most proteins). Furthermore, when the surfaces are functionalized with a specific molecule, SPR sensors can measure fast bimolecular reaction kinetics rate constants with high reliability. Currently, they are the standard against which any other surface-based sensor is compared in the field of kinetic measurements. They share the disadvantage of requiring complex optics, which makes them hard to integrate on a chip. They also require a large sample volume to perform a measurement in order to overcome intrinsic diffusion limitations in the device (as will be explained in chapter 2).

d) Dynamic Mass sensors

In a mass-spring system, a slight increase in the mass results in a linear decrease in the system's oscillation frequency. This basic principle of classical mechanics is at the origin of a whole class of microfluidic systems: resonant mass sensors. The simplest and most common form of resonator sensors are Quartz Crystal Microbalances (QCM), where a piezoelectric quartz film is driven at its resonance frequency (in the MHz range) and mass adsorption at its surface is monitored through small variations in output frequency signal. Macroscopic version of these sensors are commercially available (Elchema, Potsdam, NY, QCM Research, Laguna Beach, CA)[*60*] and research on miniaturization and integration of these sensors into lab-on-a-chip modules is already fairly advanced[*61-63*].

In a similar way, resonating cantilevers have been used as integrated sensors to detect cells and proteins in aqueous solutions[*64-66*]. They possess the advantage of being developed using conventional microfabrication and they are therefore easy to fabricate in mass. In addition, cantilever sensors can also be operated in non-resonant mode, where signal transduction is performed via the surface stress-induced bending[*67*].

Finally, in an attempt to combine the features of mass sensors within an integrated microfluidic network, novel suspended microresonator sensors (SMS) [*68*] were developed. In this type of devices, a fluidic channel runs inside a resonating cantilever such that the binding occurs within the cantilever and viscous damping by the surrounding fluid can be avoided. The development of such an integrated mass sensor not only brings forth new fabrication techniques, but also new theoretical challenges to interpret its output signal.

1.6. Single-Micron-Scale Sensing

Following a reasoning analogous to the one employed in microelectronics, there has been a constant push in microfluidic science towards smaller and smaller footprint sensors[*69, 70*]. As the device is reduced in size, analysis time scales tend to decrease, the sensor requires smaller amounts of reagents, and more of them can be packed on the same chip to create parallel sensor arrays capable of monitoring multiple analytes at the same time.

Table 1.1: Scaling of key parameters in microfluidics devices, assuming fixed pressure-driven flow and a channel width much larger than the channel thickness. Specific values for these quantities are provide for varying channels height under typical protein flow inside tubes (L=10 mm, D= 5e-5 mm^2/s, Δp= 1 atm).

Effect	Variable	Scaling*	Channel height h		
*Scaling values for pressure driven flow			**1 μm**	**10 μm**	**100 μm**
Fluid Velocity	U (mm/s)	$\sim h^2L^{-1}$	0.8	80	8×10^3
Diffusion time	t_d (s)	$\sim h^2$	0.02	2	200
Residence Time	t_R (s)	$\sim L^2h^{-2}$	10	0.1	1×10^{-3}
Mass transfer entrance length	L_E (mm)	$\sim h^4L^{-1}$	0.2	200	2×10^6
Shear Stress	τ (Pa)	$\sim hL^{-1}$	10^2	10^3	10^4
Taylor Dispersion	K/D (s.u.)	$\sim h^6L^{-2}$	2	10^6	10^{12}

However, the possible advantages of venturing into the single micron world (1-10μm length scale) or even in the nanoworld are met by new difficulties and device behavior that need to be understood further. This behavior can be captured by looking at the strong height dependence of key sensing parameters which will be studied in details in this work (Table 1.1). A quantitative example is also provided in Fig. 1.3, where the three most important time scales in any detection process are compared for various channel thickness and sensor areas in a conventional on-chip immunoassay. In order to be able to measure binding kinetics directly in a sensor the reaction time scale must always be the slowest one, such that other processes do not hide – or convolve, in scientific terms- the intrinsic reaction rates. In thick sensors (50μm or more), protein transport to a surface is almost always diffusion-limited since diffusion time scales vary as the square power of the channel thickness. In these circumstances, mass transfer effects must be accounted for to extract and quantify intrinsic reaction kinetics[*71, 72*]. Furthermore, under some operating conditions, mass transfer will completely mask surface kinetics, thus making the device unusable.

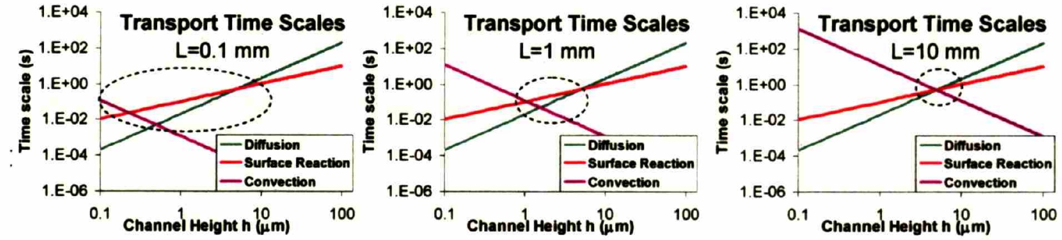

Figure 1.3: Comparison of Diffusion ($t_d=h^2/D$), surface-reaction ($t_r=h/k_{on}C_{s0}$) and convection ($t_c=L/U$) times scales in a conventional on-chip immunoassay (see details in Chapter 2, Fig. 2.1D). The channel is assumed much larger than high and the pressure driving the flow is fixed at Δp=1 atm. Left: The sensor length is 0.1 mm. The convection-time scale is fast enough that transport is reaction limited. Kinetics is therefore directly measurable inside the dashed circle. Middle: The sensor's length scale is increased to 1 mm, raising the overall convection time scale. Kinetics becomes measurable directly only in a small channel height interval. Right: Setting the sensor length to 10mm creates a situation in which transport is either convection or diffusion-limited for all channel geometries.

In Fig. 1.3 (left), when the thickness is decreased to less than 10μm, the surface reaction time scale becomes larger than the diffusion scale and kinetics becomes directly observable. However, for channels shallow enough, transport becomes limited by the rate of analyte flow inside the microchannel and no longer by either diffusion or convection. This situation becomes predominant as the length of the sensing zone increases since the convection time scales increases accordingly (Fig. 1.3 middle and right). Up to now, the study of convection limitations on transport in microchannels has been neglected in the μTAS community since technical development only allowed recently to design and test micron-size sensors[*68, 73*]. It will be addressed in details in the present work.

1.7. Thesis Outline

This thesis describes how device geometry, specifically channel height, influences transport phenomena and the ability to resolve kinetics in microfluidic sensors. Most problems addressed in this work lie at the interface between well established theoretical fields. The approach and the main contributions are summarized in Fig. 1.4.

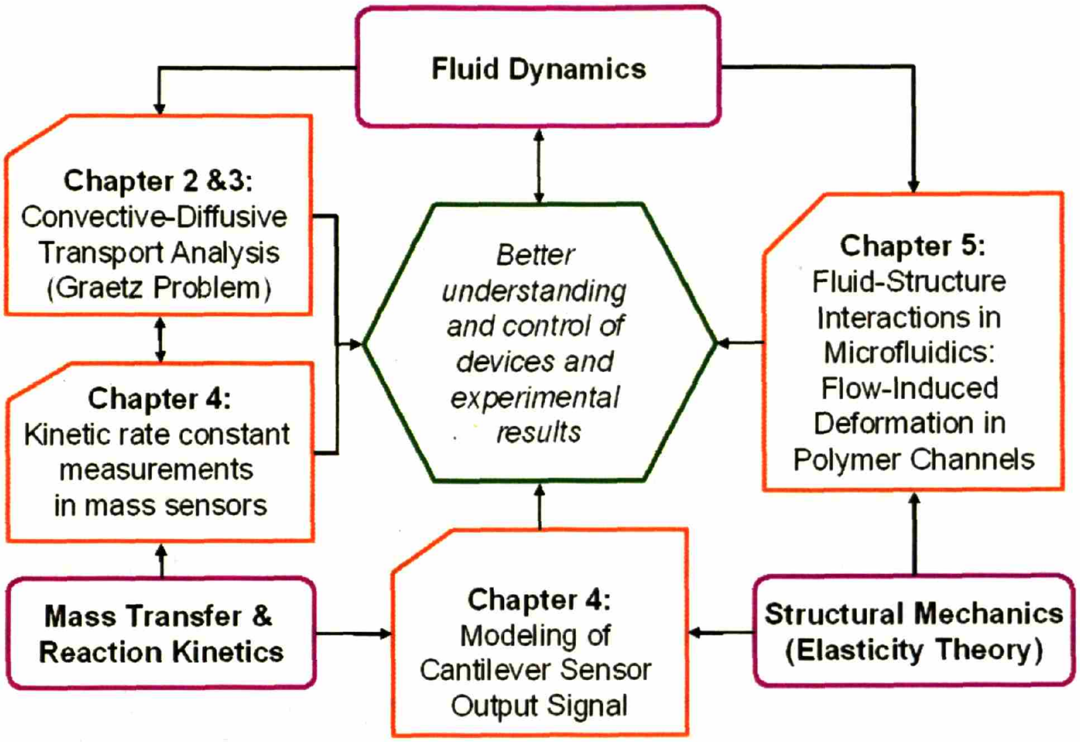

Figure 1.4: Organization of the thesis work. Most problems addressed in surface-based sensing require the support from theoretical groundwork in 3 distinct fields (Purple). The theoretical and technical work developed in this thesis lies at the interface between these well-established fields (Orange). The central research objective is to be able to understand, characterize, predict and control the quality and efficiency of microfluidic sensors (Green).

In chapter 2, we demonstrate that transport at the single micron scale rapidly exhibits convection limitations under normal operating conditions. Through mathematical analysis and numerical simulations, we formally predict the performance of microfluidic sensors, in terms of efficiency, detection limits and resolution, and time scales. Furthermore, we discuss the pros and cons of operating in convection-limited regime in microsensors.

The theoretical predictions are supported by experimental confirmation of the existence of this transport behavior. The discussion of the conditions under which convection-limited transport occurs experimentally constitutes the essential of chapter 3.

In chapter 4, we focus on the case study of a typical single micron scale sensor: the suspended microresonator sensor as developed by T.P. Burg [*68*]. Through mathematical analysis we develop the theory required to relate the output frequency signal of resonating sensors with the surface concentration profiles studied in chapter 2. We proceed then to predict shape of the output frequency under various experimental conditions taken from the literature and demonstrate how it is possible to extract information on binding kinetics from this class of sensors.

Avoiding either convection or diffusion transport limitations can, in principle, be achieved by increasing fluid flow velocity. However, in practice, the flow rate is limited by the amount of pressure a device can tolerate. In single micron scale devices, increasing the analyte's influx velocity requires very high pressures to overcome the high hydraulic resistance of such small channels. In the particular case of sensors created through soft lithography, the high pressure in microchannels can lead to channel deformation. The analysis of such deformation constitutes the principal topic of chapter 5. Through structural analysis, we demonstrate that single micron scale sensors made out of elastomers are susceptible to deformation under high flow rates. This effect is shown to vanish as channels get thicker. The results are supported by numerical simulations and experiments.

Throughout this thesis, the approach taken consists of using mathematical analysis and numerical modeling as predictive tools rather than for post processing data analysis. When the design of time consuming or expensive sensors is at stake, a thorough understanding of the underlying physical phenomena and engineering principles is key to rapidly reach specific design requirements. Furthermore, whenever possible, emphasis is set on analysis rather than simulations. Analytic solutions provide direct relationships between experimental observations, geometry and the multiple operating condition variables in a system. These direct relationships, often in the form of dimensionless numbers, help understand and control experimental results. In contrast, numerical simulations typically provide only a solution to a problem under specified conditions.

Chapter 2. Mass Transport and Surface Reactions in Microfluidic Systems

Chapter Abstract

We provide analysis of different regimes of diffusion and laminar flow convection combined with bimolecular surface reactions relevant to biochemical assays performed in microfluidic devices. Analytic solutions for concentration fields are compared to predictions from two-dimensional finite element simulations for the various operation regimes. The analytic and numerical results extend the transport models beyond the models commonly used to interpret results from surface plasmon resonance (SPR) experiments. Particular emphasis is placed on the characterization of transport in shallow microfluidic channels in which the fully developed transport regime dominates rather than the mass transfer boundary layer transport typically encountered in SPR. Under fast reaction and diffusion conditions, the surfaces saturate in a wave-like manner similar to that observed in chromatographic columns. Two key parameters relevant to on-chip biochemical assays and microfluidic sensors are studied and compiled: the capture fraction of the bulk analyte at the surface and the saturation time scale of the reactive surfaces. The physical processes in the different regimes are illustrated with data from the relevant microfluidics literature.

2.1. Introduction

Mass transfer over reactive surfaces in microfluidic devices is central to exploring and quantifying biochemical reactions, such as DNA hybridization and antigen-antibody binding. The small length scales lead to laminar flows [*24, 74*] and the corresponding high surface-to-volume ratio implies that understanding transport and reactions at surfaces requires special consideration. Many applications depend on the accurate prediction of cell-cell, protein-cell or protein-protein interaction at interfaces. Examples include controlling surface passivation [*75*], understanding cell attachment and release from surfaces [*76*] and performing general biochemical assays for sensing applications [*77*]. The surface plasmon resonance (SPR) sensor (Biacore, Uppsala, Sweden) (Fig. 2.1A) represents an example of surface-based detection systems that monitors adsorption of biological molecules onto the surface of a gold film [*59, 78, 79*]. High frequency quartz microbalances (Fig. 2.1B) have also been used in similar adsorption studies [*80*]. Hollow cantilever-based biosensors (Fig. 2.1C) are also developed as techniques for measuring adsorption kinetics [*81*]. Other chip-based detection systems include fluorescence immunoassays and DNA hybridization on patterned surfaces, either based on soft lithography microfabrication [*46*] or spotting techniques [*47, 82*]. These devices share the common features of a flow-through channel with reactive surfaces (Fig. 2.1D). In all cases, the sample to be analyzed is directed to the sensor element (the reactive surface) by a convective flow and analytes diffuse to binding sites on the surface.

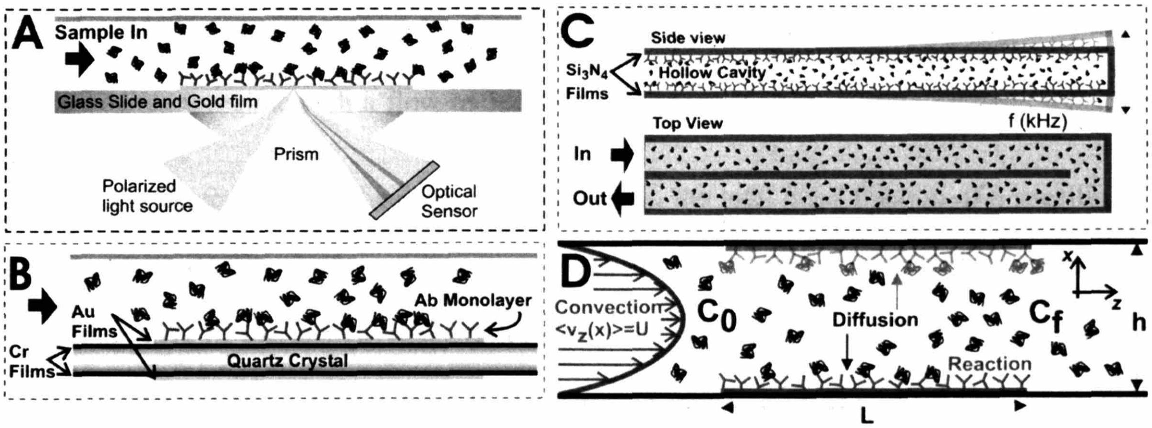

Figure 2.1: Microfluidic applications involving convection, diffusion and surface reaction in a flat plat geometry under fully developed parabolic flow conditions. A) Surface Plasmon Resonance (SPR) optical sensor (Biacore Inc.). B) Quartz Crystal Microbalance (QCM). C) Suspended Microresonator (Hollow Cantilever). D) General schematics describing the transport to surface in microdevices. The initial concentration of sample before the reaction patch is given to be C_0 and the final, well-mixed concentration is C_f. The capture fraction of the analyte passing over is thus given by $f(L,t)=1-C_f(L,t)/C_0$. Asymmetric reactions (as for A and B) involve a reaction at the bottom wall only, while symmetric reactions (as in C) involve an identical reaction at both top and bottom walls.

The steady-state diffusion-limited transport to a surface in a pressure-driven flow is known as the Graetz Problem and it is usually divided into two main operation regimes: the "entrance region" implying the presence of a mass transfer boundary layer* and the "fully developed region", with bulk depletion of the sample [*83*]. In the context of microfluidic systems, the entrance region has been studied in greater details since it is relevant to most SPR systems [*84-86*]. Two-compartment models, approximating the mass transfer in the entrance region, have provided additional insight into transport in SPR systems by taking into account surface saturation over time and reaction-limited conditions [*72, 87*]. With the increasing computing power available, the simplified numerical approach represented by two-compartment models is being replaced by detailed finite element simulations of the complete transport equations.

From a practical point of view, operating a device in the entrance regime, as is often done in SPR, leads to low sample capture fractions. For example, in a typical SPR experiment operating in the boundary regime with a flow of $5\mu\ell$/min through a channel of cross section $50\text{x}500\mu\text{m}^2$ over a 1mm detection zone, the capture fraction *f*, i.e., the total mass fraction of a specific bulk protein captured at the surface, is estimated to be 7% under diffusion limiting conditions. The remaining 93% of the analyte mass flows above the capture region and is lost for detection purposes. In this regime, f is expected to vary with the flow rate Q as $f \sim Q^{-2/3}$ [*88*]. Thus, as the fluid velocity increases, more sample needs to be consumed in order to obtain a sufficient signal to noise ratio, and consequently, more material is lost the medium. In general, microfluidic

---

* In this contribution, the term boundary layer strictly applies to mass transfer boundary layers and never to momentum boundary layers. The latter are not present since the flows are fully developed laminar flows as a consequence of the small dimensions in microfluidic channels.

devices aim to minimize sample consumption, yet operating in the entrance region goes against this goal. However, when channels reach the micron scale and the regime switches to "fully developed", the capture fraction becomes much higher, thus minimizing the detection losses.

The standard entrance region model provides poor estimates for intermediate to high capture fractions. High capture fractions are likely to be needed when expensive or short (small) plug-like samples are to be used. These samples can come from discrete sources, such as a single cell analysis device [*85*], or a sample released from a picoliter compartment [*35*] to a detection surface. In these circumstances, the models developed for standard SPR are not appropriate. Laminar flow transport models are needed to describe systems with channels widths approaching a few micrometers as in recent lab-on-a-chip systems [*69*].

The main goal of this article is therefore to develop, summarize and discuss expressions for all regimes of operation relevant to flow-through microfluidic devices involving surface reaction. Particular emphasis is set on understanding transport in the fully developed region of the Graetz problem, an oft-encountered but seldomly studied regime in microfluidics. Through analysis and numerical simulations, we demonstrate that, for sufficiently thin channels, surface transport in microfluidic channels occur in a wave-like fashion, much similar to the transport in chromatographic columns. The models are illustrated with experimental examples and kinetic data from the microfluidics literature. The overall analytic procedure provides criteria for designing and operating continuous microfluidic sensors based on convection, diffusion and reaction of multiple species, from cells to small molecules.

2.2. Physical Model

2.2.1. Continuum Transport Model Formulation

The general conservation equations, including a bulk reaction term, take the form:

$$\frac{\partial C_i}{\partial t} = -\vec{\nabla} \cdot \vec{N}_i + R_{vi}, \tag{2.1}$$

where the molar flux $\vec{N}$ is

$$\vec{N} = -D_i \cdot \vec{\nabla} C_i + \vec{v} C_i. \tag{2.2}$$

Here, C_i is the volume concentration of the i^{th} species, D_i is the diffusivity of the solute, $\vec{v}$ is the fully developed velocity profile and R_{vi} is the volumetric rate of species creation in the bulk. For all surfaces, the boundary conditions on the molar flux $\vec{N}$ represent the balance between flux to the surface and surface reaction.

$$\vec{u} \cdot \vec{N} = R_{si}. \tag{2.3}$$

$\vec{u}$ is the surface unit vector (perpendicular and pointing inward). R_{si} is the inward flux of species i into the bulk, such that surface adsorption indicates a negative R_{si} term.

Solutions to these equations have been developed for various geometries, but only the case of flat plates will be considered here. The lithographic, embossing and ablation techniques [*89*] used to create most microfluidic systems produce broad and shallow channels. These channel shapes are desirable in most applications requiring readout of the surface-bound analyte. The fully developed three-dimensional (3D) laminar axial velocity profile *v*(*height,width*) can be represented as a simple function *v*(*height*) except close to the channel's side walls [*90*]. For studies of mass transfer in channels with cross sections of different geometries, such as triangular channels produced from anisotropic etching of silicon [*91*], or semi elliptical channels obtained through isotropic etching in glass [*92*], solutions for simple cases have been provided in the literature for the fully developed region [*93*].

To further simplify the analysis, constant diffusivity is assumed for all species, even though the diffusivity in protein-dense biological media, such as cellular media, can be non-linear and highly dependent on protein size, shape and charge [*94*]. Bimolecular surface reactions involving reversible binding of species are considered as being sufficiently general to encompass the majority of surface association/dissociation reactions encountered in molecular biology. The rate equation takes the form

$$\frac{\partial C_s}{\partial t} = k_{on} C_w (C_{s0} - C_s) - k_{off} C_s , \tag{2.4}$$

Where C_w is the analyte concentration (proteins, DNA oligomers, etc.) in the channel near the reactive wall. C_s, the concentration of surface bound analytes, is a function of position on the surface. C_{s0} is the total number of binding sites. k_{on} and k_{off} are respectively the association and dissociation rate constants of the bimolecular reaction (with units $M^{-1}s^{-1}$ and s^{-1}).

Table 2. 1: Complete equation system describing diffusion, convection, and reaction in a 2D channel in dimensional and scaled form.

Coordinates	**x=[-h/2, h/2] , z=[0, L]** **(O at center left of channel)**	**x=[0, h] , z=[0, L]** **(O at lower wall left of channel)**
2D Bulk Transport	$\frac{\partial C(x,z,t)}{\partial t} = D\frac{\partial^2 C(x,z,t)}{\partial x^2} + D\frac{\partial^2 C(x,z,t)}{\partial z^2} - v(x)\frac{\partial C(x,z,t)}{\partial z}$	
Surface Reaction	$\frac{\partial C_s(z,t)}{\partial t} = k_{on}C(x = x_w, z, t)\cdot\left(C_{s0} - C_s(z,t)\right) - k_{off}C_s(z,t)$	
Normalized Bulk Transport	$\frac{\partial\Theta}{\partial\tau} = \frac{\partial^2\Theta}{\partial\eta^2} + \frac{1}{Pe^2}\frac{\partial^2\Theta}{\partial\zeta^2} - \frac{3}{2}(1-4\eta^2)\frac{\partial\Theta}{\partial\zeta}$	$\frac{\partial\Theta}{\partial\tau} = \frac{\partial^2\Theta}{\partial\eta^2} + \frac{1}{Pe^2}\frac{\partial^2\Theta}{\partial\zeta^2} - 6\eta(1-\eta)\frac{\partial\Theta}{\partial\zeta}$
Surface reaction	$\frac{\partial\Theta_s}{\partial\tau} = \varepsilon Da\cdot\left[\Theta_w(1-\Theta_s) - \bar{K}_D\Theta_s\right]$	
	both walls	one wall only
Boundary condition #1	$\left.\frac{\partial\Theta}{\partial\eta}\right\rvert_{\eta=0} = 0$ (symmetry)	$\left.\frac{\partial\Theta}{\partial\eta}\right\rvert_{\eta=0} = -\frac{1}{\varepsilon}\frac{\partial\Theta_s}{\partial\tau}$ (reaction at wall 1)
Boundary condition #2	$\left.\frac{\partial\Theta}{\partial\eta}\right\rvert_{\eta=1/2} = -\frac{1}{\varepsilon}\frac{\partial\Theta_s}{\partial\tau}$ (reaction at walls)	$\left.\frac{\partial\Theta}{\partial\eta}\right\rvert_{\eta=1} = 0$ (insulation at wall 2)
Initial and axial conditions	$\Theta(\eta,\zeta,\tau=0)=0$, $\Theta_s(\zeta,\tau=0)=0$, $\Theta(\eta,\zeta=0,\tau)=1$, $\left.\frac{\partial\Theta}{\partial\zeta}\right\rvert_{\zeta=\infty}=0$	

With the assumptions that the channel must be broad and shallow ($W>>h$), and considering that bulk reaction is negligible compared to surface reactions ($R_{vi} = 0$), the transport equations and boundary conditions simplify to a 2D problem (Table 2.1). It is useful to scale the equations in order to reveal the dimensionless parameters governing the system. The resulting scaled equations take the form:

$$\frac{\partial\Theta(\eta,\zeta,\tau)}{\partial\tau} = \left(\frac{\partial^2\Theta(\eta,\zeta,\tau)}{\partial\eta^2} + \frac{1}{Pe^2}\frac{\partial^2\Theta(\eta,\zeta,\tau)}{\partial\zeta^2}\right) - v(\eta)\frac{\partial\Theta(\eta,\zeta,\tau)}{\partial\zeta}, \tag{2.5}$$

$$\frac{\partial\Theta_s(\zeta,\tau)}{\partial\tau} = \varepsilon Da\cdot\left[\Theta(\eta=0,\zeta,\tau)\cdot\left(1-\Theta_s(\zeta,\tau)\right) - \bar{K}_D\Theta_s(\zeta,\tau)\right], \tag{2.6}$$

with the dimensionless parameter groups for axial position $\zeta = zh^{-1}Pe^{-1}$, channel height $\eta = x/h$, normalized transverse diffusion time $\tau = Dt/h^2$, relative adsorption capacity $\varepsilon = C_0h/C_{s0}$ and concentrations $\Theta_i = C_i/C_{i0}$. $Pe = Uh/D$ and $Da = k_{on}C_{s0}h/D$ are respectively the Péclet (*Pe*) and Damköhler number (*Da*). $\bar{K}_D = k_{off}/(k_{on}C_0)$ is the dimensionless equilibrium dissociation constant and $v(\eta)$ is the normalized fully developed laminar flow velocity profile depending solely, in 2D, on the normalized height parameter η (Table 2.1). Eq. (2.5) and (2.6) are coupled by a flux balance at the wall ($\vec{u}$ pointing inward)

$$\left.\frac{\partial\Theta(\eta,\zeta,\tau)}{\partial\eta}\right|_{\eta=[0,1]} = -\frac{1}{\varepsilon}\frac{\partial\Theta_s(\zeta,\tau)}{\partial\tau}. \tag{2.7}$$

2.2.2. Physical interpretation of ζ, *Da* and ε

The dimensionless parameters appearing in eqs. (2.5), (2.6) and (2.7) simplify the equations and reveal important characteristics of the physical system. $\varepsilon = C_0h/C_{s0}$ corresponds to the relative density of analytes between the bulk and the fully saturated surfaces (a measure of surface adsorption capacity relative to the bulk). It arises when matching the units of surface concentration and bulk concentration. A small ε indicates a high relative surface capacity leading to a longer saturation time. When *Da*>>1, the transport to the surface is strongly diffusion-limited, while at *Da*<<1, the transport becomes limited by the reaction at the surface and a flat (constant) concentration profile can be expected across the channel.

The diffusion/convection length scale $\zeta = zh^{-1}Pe^{-1} = z/U \cdot D/h^2$ is an important parameter in this paper as it controls the transitions in mass transfer from the entrance region to the fully developed region. Physically, at $\zeta=1$, the time scale required for diffusion across the channel height becomes the same as the time scale required for crossing a distance z at velocity *U*. For $\zeta<1$, the convection time scale is shorter than the diffusion time scale and a portion of the analytes in the channel are not able to "reach" the reactive surface exiting the sensing region.

The result is the appearance of a mass transfer boundary layer. For $\zeta>1$, analytes have plenty of time to diffuse to the reactive surfaces and no mass transfer boundary layer develops. In the case of a reactions on both top and bottom walls, the diffusion time scale becomes $\bar{t}_d = h^2/4D$ as a molecule is at most half a channel height away from a reactive wall. Nevertheless, for consistency, the scaling of τ and ζ based on reactive surface will be used throughout this paper. In many notations, when evaluated at $z=L$, the number $\zeta_L=DL/Uh^2$ is called the Graetz number and is written *Gr*.

Table 2.2 provides typical operating conditions and corresponding dimensionless parameters for three often studied microfluidic applications, antibody-antigen (Ab-Ag) interaction, Streptavidin-Biotin affinity, and DNA hybridization. These examples span the range of applications, typical density of immobilized probes or “reactive sites”, and lengths scales (μm to mm).

Table 2. 2: Three typical examples of microfluidic applications

	Protein A33 immunoassay	Streptavidin/bBSA binding in suspended microresonator	Single mutation detection using DNA- oligomer hybridization
Flow rate Q	1 μℓ·min^{-1}	0.0024 μℓ·min^{-1}	1 μℓ·min^{-1}
Width W	0.5 mm	0.02 mm	0.5 mm
Height h	0.05 mm	0.001 mm	0.05 mm
Average Velocity U	0.67 mm·s^{-1}	2 mm·s^{-1}	0.67 mm·s^{-1}
Diffusivity D	~10^{-4} mm^2/s	6x10^{-5} mm^2/s	4.3x10^{-5} mm^2/s
Length of Bed L	0.1 mm	2 mm	400 μm (round spot)
$\zeta_L = \frac{L \cdot D \cdot w}{Q \cdot h}$	0.007	60	0.01
k_{on}	2.4x10^5 M^{-1}s^{-1}	1.2x10^5 M^{-1}s^{-1} *	~1.2x10^5 M^{-1}s^{-1}**
k_{off}	3.5x10^{-3} s^{-1}	~0	~2.1x10^{-4} s^{-1}**
C_{s0}	70 fmol·mm^{-2}	70 fmol·mm^{-2} *	8 fmol·mm^{-2}
C_0	0.1 μM†	0.1 μM†	0.1 μM†
$\varepsilon = C_0 h / C_{s0}$	0.07	0.0014	0.6
$Da \equiv k_{on} C_{s0} h / D$	~10	0.14	~1
$Pe = Uh/D$	335	17	335
$\bar{K}_D = k_{off} / k_{on} C_0$	0.14	~0	0.02
Reference	*(Catimel et al. 1997)*	*(Burg 2004)*	*(Wang et al. 2003)*

* Reference: [*95*]**reference [*80*]

† Arbitrarily defined to correspond to an order of magnitude commonly found in cell signaling proteins

2.3. Analytic Solutions and Numerical Simulations

The non-linear convection/diffusion/reaction problem summarized in Table 2.1 can be solved numerically (e.g., by using finite element methods) to provide an accurate solution to a specified set of parameters. Analytic solutions, when feasible, provide insight into the relationship between parameters (space, time, rate constants, etc.) and dependent variables (bulk and surface concentration, capture fraction, etc.). No complete analytic solutions exist to the whole problem due to the non-linear surface reaction term, but the solution space can be segmented into physically relevant parameter regimes for which analytic solutions exist. In particular, the transport equations can be decomposed in two accurate analytic solutions for $\zeta >> \zeta_{crit}$ and $\zeta << \zeta_{crit}$, where ζ_{crit} represents the critical value from which the two analytic models have the same relative error compared to the numerical solution. These solutions can be subdivided once more depending on whether the surface Damköhler number is finite (partially reaction-limited) or infinite (fully diffusion-limited). The numerical simulations and analytic solutions provide complementary physical insights into coupled transport and reaction phenomena in microfluidic applications while also serving as a firm basis for device design.

The complete transport problem with a bimolecular reaction at one or both surfaces (Table 2.1) was simulated by finite element methods implemented in FEMLAB (Comsol AB, Stockholm, Sweden). Since many studies have been conducted for the entrance case – $\zeta << 1$, which is particularly relevant to SPR [*85, 86, 96*], the present simulations primarily aimed to characterize the fully developed region.

2.3.1. The Graetz problem in mass transfer

In most applications involving high relative adsorption capacity (low ε), the bulk concentration reaches a steady state value much before the surface has been significantly saturated. The transport in the bulk can then be assumed to be in pseudo steady state with respect to the surface at all times. Moreover, in most microfluidic applications, the axial convection is much faster than the axial diffusion, i.e., $Pe >> 1$. Pe is usually on the order of 10^2-10^4. As a result axial diffusion can be neglected and the simplified, scaled, transport problem, known as the Graetz problem in heat transfer, then takes the form:

$$\frac{\partial^2 \Theta(\eta,\zeta)}{\partial \eta^2} = v(\eta)\frac{\partial \Theta(\eta,\zeta)}{\partial \zeta}. \tag{2.8}$$

The coupled, nonlinear boundary condition found in eq. (2.6), implies that the system composed of eqs. (2.7), and (2.8) generally has to be solved numerically. However, in cases where $C_s << C_{s0}$ (at sufficiently small times), the bimolecular surface reaction, eq. (2.4), reduces to a pseudo first order reaction and the boundary condition becomes linear:

$$\left.\frac{\partial\Theta(\eta,\zeta,\tau)}{\partial\eta}\right|_{\eta=0} = Da\cdot\Theta(\eta=0,\zeta,\tau)\,. \tag{2.9}$$

The linear system, which is relevant to practical cases - when operating under the surface saturation threshold ($C_0 << K_d$ or $t << \bar{t}_{sat}$), can be solved analytically (Table 2.3) using the method of separation of variables to obtain an eigenfunction expansion of the solution [*97*]. The exact form of the eigenfunction expansion has been provided for the circular pipe and parallel plate geometry with rapid reaction at both walls [*98*]. In Table 2.3, we also introduce the exact form of the eigenfunction expansion for the case of parallel plates with reaction at only one wall, including the first 5 expansion coefficients and eigenvalues for the fully diffusion-limited case.

Table 2. 3: The scaled Graetz problem for a first order reaction on both walls (symmetric case) and one wall (asymmetric case). For more details on the development of the fully analytic solutions, consult Appendix A1.

Coordinates	**Symmetric Case**	**Asymmetric case**
	η=[-1/2, 1/2], ζ = [0, $^{L}/_{hPe}$] **(O at center left of channel)**	**η=[0, 1], ζ = [0, $^{L}/_{hPe}$]** **(O at lower wall left of channel)**
Bulk Transport Graetz Problem	$\frac{\partial^2\Theta}{\partial\eta^2}=\frac{3}{2}(1-4\eta^2)\frac{\partial\Theta}{\partial\zeta}$	$\frac{\partial^2\Theta}{\partial\eta^2}=6\eta(1-\eta)\frac{\partial\Theta}{\partial\zeta}$
Boundary condition #1	$\left.\frac{\partial\Theta}{\partial\eta}\right\|_{\eta=0}=0$ (symmetry)	$\left.\frac{\partial\Theta}{\partial\eta}\right\|_{\eta=0}=-\frac{1}{\varepsilon}\frac{\partial\Theta_s}{\partial\tau}$ (reaction at wall 1)
Boundary condition #2	$\left.\frac{\partial\Theta}{\partial\eta}\right\|_{\eta=1/2}=-\frac{1}{\varepsilon}\frac{\partial\Theta_s}{\partial\tau}$ (reaction at walls)	$\left.\frac{\partial\Theta}{\partial\eta}\right\|_{\eta=1}=0$ (insulation at wall 2)
Surface reaction	$\frac{\partial\Theta_s}{\partial\tau}\approx\varepsilon Da\Theta_w$, valid for $\Theta_s(\zeta,\tau)<<1$ (unsaturated surface, pseudo first order)	
Axial boundary Conditions	$\Theta(\eta,\zeta=0)=1$	
General form of solution	$\Theta(\eta,\zeta)=\sum_{i=1}a_iG_i(\lambda_i,\eta)\exp\left(-\frac{\lambda_i^2\zeta}{6}\right)$	
Basis Function $G_i(\lambda_i, \eta)$ =	$\exp(-{}^{\lambda_i\eta^2}/_{2})\cdot M\left(\frac{1}{4}-\frac{\lambda_i}{16},\frac{1}{2},\lambda_i\eta^2\right)^*$	$\frac{1}{2}\exp\left(\frac{\lambda_i\eta(1-\eta)}{2}\right)\cdot\left\{\overline{M}\left(\frac{1}{4}-\frac{\lambda_i}{16},\frac{1}{2},\lambda_i(1/2-\eta)^2\right)-Cst(\lambda_i)\cdot(1-2\eta)\cdot\overline{M}\left(\frac{3}{4}-\frac{\lambda_i}{16},\frac{3}{2},\lambda_i(1/2-\eta)^2\right)\right\}^\#$
Velocity-averaged solution	$\Theta_b(\zeta)=\sum_{i=1}^{\infty}A_i\exp(-\frac{\lambda_i^2\zeta}{6})$, where $A_i=\int_{\eta=0}^{\eta=1}a_iG_i(\lambda_i,\eta)\cdot v(\eta)d\eta$	

* $M(a,b,\zeta)=\sum_0^\infty\frac{(a)_k}{(b)_k}\frac{\zeta^k}{k!}$ is the confluent hypergeometric function, or Kummer M function [99].

\# $\overline{M}\left(a,b,\lambda_i({}^{1}/_{2}-\eta)^2\right)=\frac{M\left(a,b,\lambda_i({}^{1}/_{2}-\eta)^2\right)}{M\left(a,b,{}^{1}/_{4}\lambda_i\right)}$ is the Kummer M function normalized to 1 at η=0 and η=1.

The constant for the asymmetric basis functions reads:

$$Cst(\lambda)=\frac{(\lambda-4)\cdot M(\frac{1}{4}-\frac{\lambda}{16},\frac{1}{2},\frac{\lambda}{4})+(\lambda+4)\cdot M(-\frac{3}{4}-\frac{\lambda}{16},\frac{1}{2},\frac{\lambda}{4})}{(\lambda-12)\cdot M(\frac{7}{4}-\frac{\lambda}{16},\frac{3}{2},\frac{\lambda}{4})+(\lambda+4)\cdot M(\frac{3}{4}-\frac{\lambda}{16},\frac{3}{2},\frac{\lambda}{4})}\times\frac{M(\frac{3}{4}-\frac{\lambda}{16},\frac{3}{2},\frac{\lambda}{4})}{M(\frac{1}{4}-\frac{\lambda}{16},\frac{1}{2},\frac{\lambda}{4})}$$

Table 2. 4: Results Summary. Decomposition of the Graetz problem, with bimolecular surface reaction, in its various asymptotic solutions. Parameters of interest are the fraction of the total number of analytes captured by the surface *f(ζ)* and the time required to saturate the surface in various regimes. In intermediate cases, where an analytic solution is not possible, an upper bound is given and reference to further analysis is provided.

Regime	**Characteristics**	**Capture fraction** $f(\zeta,t)=1-\Theta_{bulk}(\zeta,t)$	**Surface Concentration** $\Theta_s(\zeta,t)$ **or effective rate constant** $\frac{\partial\langle\Theta_s\rangle}{\partial t}=k_{on}^{eff}C_0\left(1-\langle\Theta_s\rangle\right)-k_{off}^{eff}\langle\Theta_s\rangle$	**Surface saturation time constant** $\Theta_s(\zeta,T_{0.95})=0.95\Theta_{s-eq}$ $T_{0.95}(\zeta,\bar{t}_d,\bar{K}_D,\varepsilon);$	**Applications (Microfluidics)**	**Method Reference**
Entrance Region $\zeta<\zeta_{crit}$ $n_w=1$ (asym. reaction) $n_w=2$ (sym. reaction)	***Da= ∞,***	$1-\exp\left\{-\frac{3n_w}{\Gamma(1/3)}\left(3\zeta/2\right)^{2/3}\right\}$ Fully Analytical solutions	$\Theta_s\approx0.98\frac{\varepsilon\cdot t}{\bar{t}_d\cdot\zeta^{1/3}}\Theta_b(\zeta)$ valid for $Da\,(1-\Theta_s)\zeta^{1/3}>>1$	$T_{0.95}\approx0.97\frac{h^2}{\varepsilon D(1+K_D)}\zeta^{1/3}$ valid for $Da\,(1-\Theta_s)\zeta^{1/3}>>1$	Surface Plasmon Resonance (SPR) , high flow rates in thick channels,	Deen (1998), Lok (1983)
	Da = finite.	$1-\Theta_b(\zeta,t)$ Numerical Solutions	$k_{on}^{eff}=\frac{k_{on}}{1+0.95Da\left(1-\langle\Theta_s\rangle\right)\zeta_L^{1/3}}$ $k_{off}^{eff}=\frac{k_{off}}{1+0.95Da\left(1-\langle\Theta_s\rangle\right)\zeta_L^{1/3}}$	Numerical Solutions	SPR, on chip DNA hybridization, Ab-Ag complexes	Mason(1999)
Fully Developed Region $\zeta>\zeta_{crit}$	***Da arbitrary, unsaturated surface*** $\Theta_s<<1$	$f(t)=1-\exp\left\{-n_w\bar{k}_{d/r}(Da)\zeta\right\}$ (valid for pseudo first order reactions) (See figure 3 for $\bar{k}_{d/r}$)	$\Theta_s\approx\frac{\bar{k}_{d/r}\cdot\varepsilon\cdot t}{\bar{t}_d}\Theta_b(\zeta)$ with $\Theta_b(\zeta)=\exp\left\{-n_w\bar{k}_{d/r}\zeta\right\}$	Numerical Solutions	Heat/Mass Transfer in long, narrow channels (non specific adsorption control)	Shah & London (1978)
	Da>>1, **(Wave Regime)**	$f(t)=1-\Theta_b\left(\bar{\xi}_L+\bar{\xi}_{shift}\right)$ $\bar{\xi}_L=\frac{L}{Pe\cdot h}-\frac{U_{eff}\cdot t}{U\cdot\bar{t}_d},\ \bar{\xi}_{shift}=\frac{1}{\varepsilon(1+\bar{K}_D)}$,	$\Theta_s(\bar{\xi})\cong\frac{\Theta_b(\bar{\xi})}{1+\bar{K}_D}$ and $\Theta_b(\bar{\xi})=\exp\left\{-n_w k_{d/r}\bar{\xi}\right\}$	$T_{1.00}\approx L/U_{eff}$ where $U_{eff}=\frac{\varepsilon U}{\varepsilon+n_w\left(1+\bar{K}_D\right)^{-1}}$ with wave regime valid for $L>>\frac{U\bar{t}_d}{n_w\cdot\bar{k}_{d/r}}$	Mass transfer in long, narrow channels: Non specific adsorption, single cell analysis, passivation arbitrary wall resistance, fine structures	Rhee & Amundson (1989)
	Da<<1, **(Wave Regime)**	$f(t)=1-\Theta_b(\bar{\xi}_L)$, $\sigma=\sqrt{\frac{2}{\pi}}\frac{1}{n_w\bar{k}_{d/r}(Da_{eff})}$	$\Theta_s(\bar{\xi})\cong\frac{\Theta_b(\bar{\xi})}{1+\bar{K}_D}$ and $\Theta_b(\bar{\xi})=\frac{1}{2}\mathrm{erfc}\left\{\bar{\xi}/\sqrt{2}\cdot\sigma\right\}$			Cazes & Scott (2002) This paper
Full Solutions: ***ζ arbitrary***	***Varies***	Mostly Numerical Solutions			High concentration of analytes (non conventional geometries,Complex kinetics, non linear diffusion)	Varies

These analytic solutions converge slowly: after a 5 term expansion, the maximum relative error on the concentration is still ~5%. However, the complete set of functions is only necessary when the full 2D concentration profile must be mapped. For most practical applications, the time scale of saturation of the substrate or the fraction of mass bound to the surface is of primary interest rather than the detailed concentration profile in the fluid channel. In those cases, the general solution can be separated according to different parameter regimes and analytic solutions calculated with respect to the velocity-weighted, or "mixed-cup" bulk concentration

$$\Theta_b(\zeta,\tau) = \int_{\substack{cross \\ \sec tion}} \Theta(\eta,\zeta,\tau)\cdot v(\eta)d\eta\,, \tag{2.10}$$

where $v(\eta)$ is the normalized velocity profile (see Table 2.3).

2.3.2. Capture fraction of a bed and saturation time scales

The total capture fraction of a bed of length L represents the fraction of analytes adsorbed on the surface after one passage, specifically:

$$f(L) = \frac{C_0 - C(L)}{C_0} = 1 - \Theta_b(L)\,. \tag{2.11}$$

The saturation time scale is defined herein as the time required for saturating 95% of the available binding sites for the analyte. When the reaction is fully diffusion-limited, solutions depend only on the diffusivity, and for reaction limited situations, only the reaction constant is involved. For intermediate case, the saturation time will depend on both diffusion and reaction rates, making it therefore possible to be expressed as a function of Da. This parameter and the diffusion/convection length scale ζ, are the two main parameters for characterizing surface capture and transport phenomena in microfluidic devices. The possible regimes are summarized in Table 2.4 and discussed in detail in the following sections.

2.3.3. Solutions for fully diffusion-limited situations

2.3.3.1. Entrance Region (ζ<<1) and $Da \to \infty$

The mass transfer entrance region arises when the diffusion time scale ($\bar{t}_d = h^2/D$) is much greater than the axial convection time scale ($\bar{t}_c = z/U$), such that $\zeta = \bar{t}_c/\bar{t}_d << 1$ and a mass transfer boundary layer of thickness $\delta << h$ appears. This problem was analyzed early in the SPR literature [*88*]. It is also common in flow-through devices, such as quartz microbalances and any other surface-based sensors.

The bulk concentration along the channel length can be computed using a mass transfer coefficient approach [*100*]

$$\frac{\partial \Theta_b(\zeta,\tau)}{\partial \zeta} = -n_w Sh \cdot (\Theta_b(\zeta,\tau) - \Theta_w(\zeta,\tau)), \tag{2.12}$$

where the Sherwood number *Sh*, is the mass transfer coefficient (k_m) scaled by the characteristic length scale (*l*) and the diffusion coefficient (*D*) (*i.e.* $Sh \equiv k_m l/D$). The Sherwood number, is defined as the ratio of the gradient at the wall divided by the driving force for mass transport:

$$Sh \equiv \frac{\left(\partial \Theta(\eta,\zeta) \big/ \partial \eta \right)_{wall}}{\Theta(\eta,\zeta)_{bulk} - \Theta(\eta,\zeta)_{wall}}. \tag{2.13}$$

The Sherwood number is expressed on a per wall basis. The index n_w takes into account the number of walls participating in the reaction, $n_w = 1$ for the asymmetric reaction case and $n_w = 2$ for the symmetric case.

Assuming the surface concentration is 0 ($Da \to \infty$) the Sherwood number of the entrance (E) region yields the well known result:

$$Sh_E = \frac{3}{\Gamma(1/3)}\left(\frac{3\zeta}{2}\right)^{-1/3} = 0.978 \cdot \zeta^{-1/3}. \tag{2.14}$$

The dependence on $\zeta^{-1/3}$ indicates that, as $\zeta \to 0$, mass transfer to the surface will become very large and the system will become reaction-limited. Consequently, this regime of operation is preferred for the determination of reaction rate constant (as in SPR systems).

By solving eq. (2.12) with the expression of the Sherwood number found in eq. 14, and using the axial boundary condition, $\Theta_b(\zeta = 0) = 1$, the bulk concentration remaining after a distance ζ can be expressed as

$$\Theta_{bE}(\zeta) = \exp\left\{-\frac{3n_w}{\Gamma(\frac{1}{3})}\left(\frac{3\zeta}{2}\right)^{\frac{2}{3}}\right\} = \exp\left\{-1.467 n_w \zeta^{\frac{2}{3}}\right\} \tag{2.15}$$

For sufficiently large *Da*, the flux to the surface is mass transfer-limited and constant at any given position down the channel. As a result, the surface concentration increases linearly in time and the saturation time can be expressed as

$$\left.\frac{n_w}{\varepsilon}\frac{\partial \Theta_s}{\partial \tau} + \frac{\partial \Theta_b}{\partial \zeta}\right|_{z=L} = 0 \;\Rightarrow\; \Theta_s = \frac{\varepsilon}{n_w} Sh_E(L) \cdot \Theta_b(L) \cdot \tau. \tag{2.16}$$

For small ζ, $\Theta_b(\zeta) \to 1$. The time scale for which the surface becomes 95% saturated, i.e. $\Theta_{s-sat} \to 0.95 \cdot (1 + \bar{K}_D)^{-1}$, is thus given by

$$T_{0.95} = \frac{h^2\varepsilon}{D(1+\bar{K}_D)\Theta_b(L)}\frac{0.95}{0.978}\zeta^{1/3} \approx 0.97\frac{h^2\varepsilon}{D(1+\bar{K}_D)}\zeta^{1/3}. \tag{2.17}$$

This expression is valid when the transport is strongly diffusion limited. This situation arises in the case of slow diffusing species such as DNA strands or large proteins flowed over a bed of highly concentrated probes.

2.3.3.2. Fully developed region (ζ>>1), $Da \to \infty$

For the fully developed region, diffusivity is fast enough compared to the convective time scale so that no boundary layer appears. The linearization of the flow profile made in section 2.3.3.1 no longer holds since the whole channel now participates in the reaction, and the full solution to the transport equations found in Table 2.1 must be considered.

For the fully developed region, the mass transfer coefficient can be calculated using the definition of the Sherwood number in eq. (2.13). By integrating the eq. (2.8), a relation between the bulk concentration and the flux at the wall is found to be

$$\frac{\partial \Theta_b(\zeta)}{\partial \zeta} = -n_w \left(\frac{\partial \Theta(\eta,\zeta)}{\partial \eta} \right)_{walls} . \tag{2.18}$$

Using these relations and applying them to the eigenfunction expansion (Table 2.3), the analytic expression for the Sherwood number for large ζ ($Da \to \infty$) is given by [93]

$$Sh_{FD} = \frac{\lambda_1^2}{n_w 6} = \begin{cases} 2.4304 & \text{asymmetric reaction case} \\ 3.7704 & \text{symmetric reaction case} \end{cases} \tag{2.19}$$

The first eigenvalue λ_1 of the solution expansion is different whether symmetric or asymmetric reaction is assumed.

Substituting the fully developed Sherwood number in the general mass transfer, eq.(2.12), the expression of the bulk concentration as a function of distance becomes

$$\Theta_{bFD}(\zeta) = \exp\left(-n_w Sh_{FD}\right) = \exp\left(-\frac{\lambda_1^2 \zeta}{6} \right) . \tag{2.20}$$

2.3.4. Critical ζ value and mass transfer regime change

The successful design and characterization of a sensor will necessarily require the use of the proper transport model within the device. The absolute maximum error committed by selecting the wrong model (between eq. (2.15) and eq. (2.20)) goes as high as 18% while the relative error ("model value"/"numerical value") goes to infinity (Fig. 2.2).

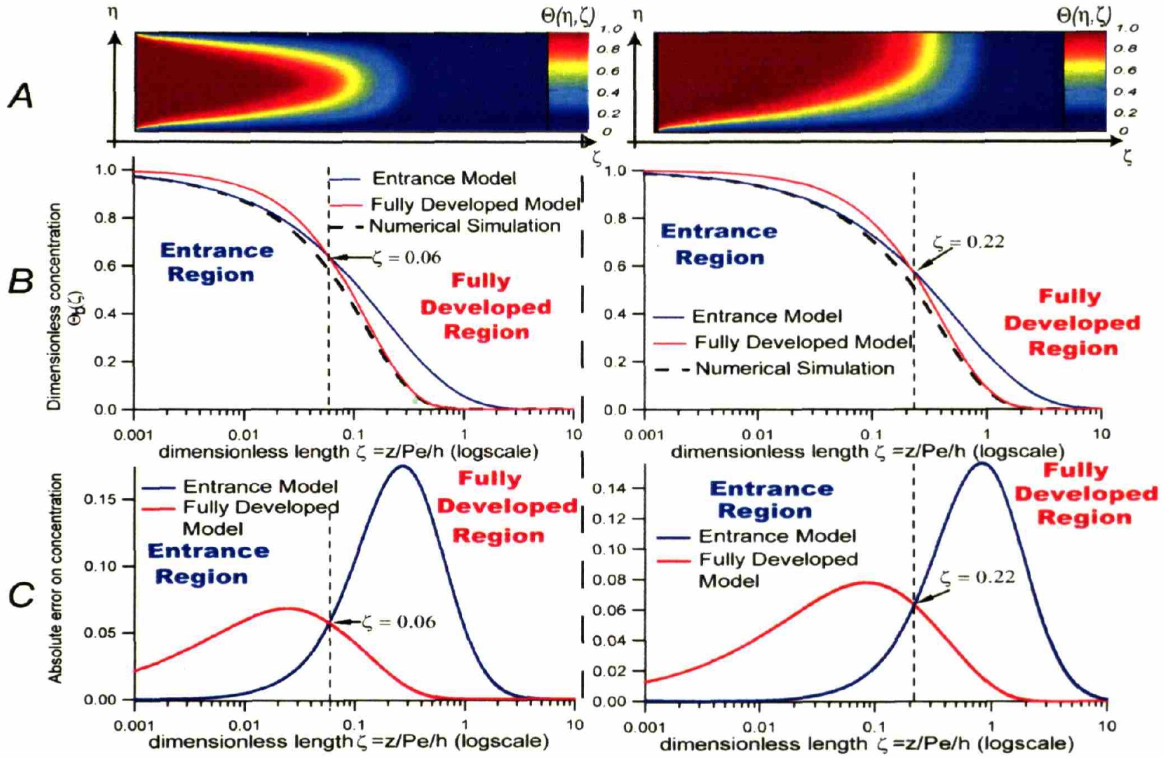

Figure 2.2: Numerical Simulation of the Graetz problem for parallel plate geometry and diffusion limited reaction at both walls. Left: symmetric reaction, Right: Asymmetric reaction. A) Numerical simulation of the concentration profile in dimensionless units ($\eta=x/h$, $\zeta=z/Pe/h$). The ζ axis is presented in logarithmic scale to emphasize the boundary layer at $\zeta<<1$. B) Plot of the normalized bulk concentration $\Theta_b(\zeta)$. Comparison of the asymptotic models for small ζ (grey, entrance region, see eq. (2.15)) and large ζ (black, fully developed region, see eq. (2.20)) with the numerical model (black dotted line) over 4 log units in ζ. C) Absolute error on the bulk concentration $\Theta_b(\zeta)_{\text{analytic}}$ - $\Theta_b(\zeta)_{\text{numerical}}$.

The simulation presented in Fig. 2.2 establishes the domain of validity of the two asymptotic models in the fully convective ($Pe \to \infty$) and diffusion-limited ($Da \to \infty$) regime at steady state (Graetz Problem, eq. (2.8)). The absolute error on $\Theta_b(\zeta)$ on both models is plotted as a function of ζ (Fig. 2.2) for the case of reaction at one or both walls. The point at which the error is the same for both models is identified as the transition point (ζ_{crit}) between the entrance region and the fully developed region. Its value was found to be ζ_{crit}=0.06 and ζ_{crit}=0.22 for the symmetric and asymmetric reaction cases respectively. These values are consistent since, as mentioned earlier, the real height scale in the case of the symmetric reaction is $h/2$ which explains why ζ_{crit} is smaller by a factor of ~4 in the symmetric case.

2.3.5 Solutions for partially diffusion-limited situations

2.3.5.1. Entrance Region: Bimolecular reaction or finite *Da* numbers

Typically in biology, binding reactions are not sufficiently fast to be assumed purely mass transfer-limited. Bimolecular surface Damköhler numbers range from less than 1 for very thin structures and slow binding species, such as DNA, to more than 10 for faster surface reactions, such as protein-protein interactions. In general, the higher the probe density at the surface (C_{s0}), the faster the effective reaction will be and the higher the Damköhler number.

For first order reactions with finite Damköhler numbers or bimolecular reaction kinetics, a similarity solution is no longer possible and only a partially analytic solution can be found [*101*]. Nevertheless, this regime, which is a generalization of the one described in 3.3.1, is useful under a much larger set of reaction conditions often appearing in SPR analysis or any sensor operating in a mass transfer boundary layer regime.

In the past, several two-compartment numerical models have been designed to compute the effective saturation time scales for this type of problem [*72, 87*]. Using a semi analytical approach, others have obtained similar results [*86, 102*]. They defined the effective reaction rate equation to be

$$\frac{\partial\langle\Theta_s\rangle}{\partial t}=k_{on}^{eff}\left(1-\langle\Theta_s\rangle\right)-k_{off}^{eff}\langle\Theta_s\rangle. \tag{2.21}$$

$\langle\Theta_s\rangle$ is the average concentration along the reaction zone of length L. The effective association and dissociation first order rate constants are found in Table 2.4. A high Sherwood number, indicating fast mass transport, brings these equations back to the simple bimolecular rate equation found in eq.(2.4). Analytic expressions for the capture fraction and saturation time only exist for the cases of fully diffusion-limited reaction at the surface. In this case, due to the dependence in Θ_s of the effective reaction rates, the rate equation has to be solved numerically.

2.3.5.2. Fully developed region: Bimolecular reaction or finite *Da*

For transport outside the boundary layer regime, the solution derived here is much more tractable than the one presented in section 2.3.5.1. Furthermore, as Da decreases, the error on the numerical model provided by the fully developed asymptotic model decreases, thus making it much more useful than the boundary layer model under certain conditions. The derivation of the results is analogous to the ones in section 2.3.3.2 and 2.3.5.1. The Robin boundary condition at the walls, eq.(2.9), is used to link the flux at the wall to the concentration near the wall $\Theta_w(\eta,\zeta)$ in eq. (2.18). Using these relations, the expression of the effective Sherwood number for an arbitrary first order reaction becomes

$$Sh_{FD}(Da)\equiv\frac{1}{\frac{1}{\bar{k}_{d/r}}+\frac{1}{\bar{k}_s}}\rightarrow\left(\frac{1}{\frac{\lambda_1^2(Da)}{6n_w}}+\frac{1}{Da}\right)^{-1}, \tag{2.22}$$

This result is analogous to the mass transfer coefficient approach used in the boundary layer theory [*100*]. The two terms represent to mass transfer rates $\bar{k}_{d/r}$ (bulk) and $\bar{k}_s$ (surface) added in series such that, when $Da \rightarrow \infty$, $Sh_{FD}(\infty) \rightarrow \lambda_1^2 / 6n_w$ and when $Da \rightarrow 0$, $Sh_{FD}(0) \rightarrow 0$. In this case however, the partially reaction limited bulk transfer coefficient $\bar{k}_{d/r}$ depends not only on the flow and diffusion properties in the bulk, but also on the reaction rate at the surface. The diffusion/reaction mass transfer coefficient (per surface) $\bar{k}_{d/r}$ as we define it here

$$\bar{k}_{d/r}(Da) = \frac{\lambda_1^2(Da)}{n_w 6} \tag{2.23}$$

is therefore a function of Da.

Replacing the value of Sh with $Sh_{FD}(Da)$ in eq. (2.12) and the value of value of Θ_w by its flux value using eq. (2.9), then eq. (2.18), an alternative notation for the transport coefficient involving both diffusion and reaction is found to be

$$\frac{\partial \Theta_b(\zeta)}{\partial \zeta} = -n_w Sh_{FD}(Da) \cdot (\Theta_b(\zeta) - \Theta_w) = -n_w \cdot \bar{k}_{d/r}(Da) \cdot \Theta_b(\zeta) \tag{2.24}$$

The value of $\bar{k}_{d/r}(Da)$ is plotted in Fig. 2.3.

Using an identical approach as in section 2.3.3.2, the generalized bulk concentration profile along the axis for an arbitrary first order reaction is

$$\Theta_{bFD}(\zeta) = \exp\left(-n_w \bar{k}_{d/r} \zeta\right) = \exp\left(-\frac{\lambda_1^2(Da)}{6} \zeta\right) \tag{2.25}$$

This time, the first eigenvalue λ_1 will vary with respect to Da and will have to be determined numerically, using the basis function described in Table 2.3 and applying the second boundary condition, found in eq. (2.9). The eigenvalue equation which provided the numerical values of $\lambda_1^2 / 6n_w$ *vs* Da in Fig. 2.3 is intractable analytically due to its algebraic complexity. To allow a quick approximate calculation of $\bar{k}_{d/r}$, we therefore provide an approximation of its numerical solution by a three parameter fit (see Fig. 2.3).

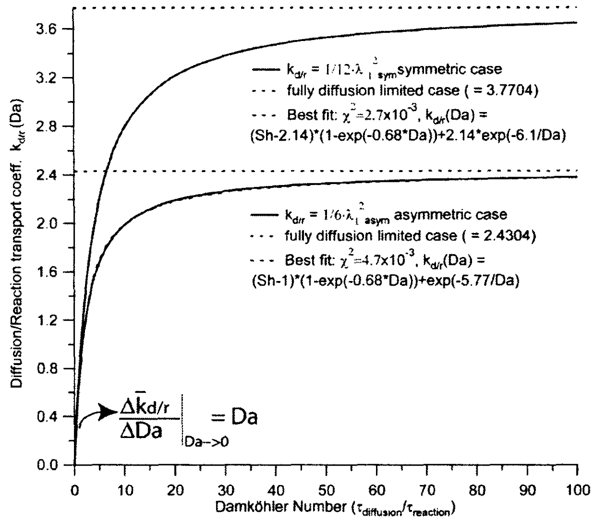

Figure 2.3: Plot of the effective diffusion/reaction transport coefficient $\bar{k}_{d/r}$ of the Graetz problem as a function of the *Da* number (i.e. including finite first order reaction rate) for the asymmetric case (lower) and the symmetric case (upper). The dotted horizontal lines mark the respective maxima, equivalent to the Sherwood number $Sh_{sym} = 3.7704$, $Sh_{asym} = 2.4304$). The dotted curves represent the best fit according to a two-parameter model: $\bar{k}_{d/r}(Da) \approx (\bar{k}_{d/r}(Da \to \infty) - \gamma)\exp(-\kappa_1 \cdot Da) + \gamma \exp(-\kappa_2 / Da)$ and the χ^2 error estimation is given. From the numerical calculations, we also observe that, when $Da \to 0$, $\bar{k}_{d/r}(Da) \approx Da$ and the relation becomes even simpler to use.

Eq. (2.27) will only be valid when the surface is not saturated, such that the pseudo first order reaction approximation can be used. For very long capture beds, it implies that the saturation time constant of the bed can no longer be evaluated by assuming a pseudo steady state profile above the bed. Instead a moving front, or wave-like, approach has to be used and the saturation time has to be deduced from the velocity of the resulting wave front (see below).

2.3.6. Critical ζ value and regime change for finite Da

The critical value of ζ at which the boundary layer model is no longer better than the fully developed model cannot be determined using a straight forward approach in the case of finite Damköhler numbers since no analytic solution exists for the entrance region case. The limit needs to be computed numerically for every value of *Da* which renders the process tedious. However, it is important to note that the usefulness of the fully developed model over the entrance region model increases as *Da* decreases. This can be justified by showing that the error on the model decreases as *Da* decreases. This behavior is presented graphically in Fig. 2.4. The algebraic details of the proof are presented in section 2.7.1. The error on $\bar{k}_{d/r}(Da)$ by keeping only the first term of the expansion is thus 4 to 6 times less when $Da \to 1$. The repercussion on Θ_b is to reduce the error caused by using the fully developed region model over for the entrance region by one order of magnitude (Fig. 2.4B).

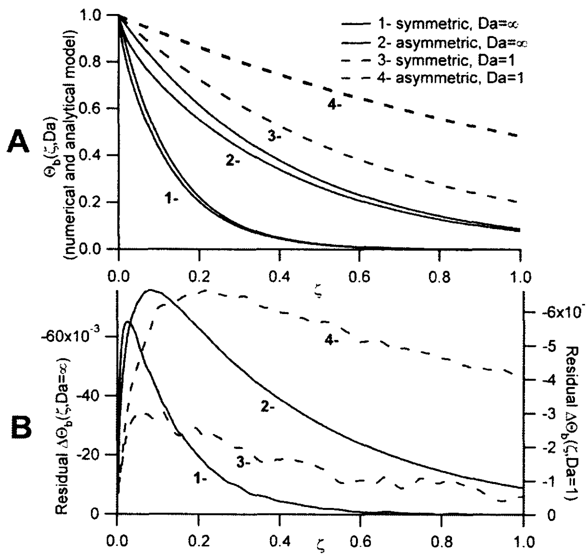

Figure 2.4: Numerical Simulation of surface transport with a first order surface reaction for parallel plate geometry in the fully developed region. A) Plot of the normalized bulk concentration $\Theta_b(\zeta)$ for the fully diffusion-limited case ($Da=\infty$) and for a partially reaction-limited case ($Da=1$). Comparison of the asymptotic models with the numerical models (lowest in the pair of lines for $Da=\infty$, difference undistinguishable for $Da=1$) for both symmetric and asymmetric reaction cases in the fully developed region. B) Absolute error on the bulk concentration $\Delta\Theta_b(\zeta)= \Theta_b(\zeta)_{\text{numerical}} - \Theta_b(\zeta)_{\text{asymptotic-FD}}$. The error for the case where $Da=1$(dashed lines), is one order of magnitude lower than for $Da=\infty$, which explains why the asymptotic and numerical models coincide in A.

2.4. Wave-Like Propagation of Bulk Concentration

2.4.1. Convection-limited transport

Reactions in long and thin structure naturally yield higher ζ and lower Da compared to the usually thicker microfluidic channels. The suspended microresonator device introduced by Burg et al. has this characteristic (see Table 2.2, entry 2). Physically, these numbers (ζ=60, ε =10^{-3}, Da=0.1) indicate a rapid axial depletion of the bulk and a diffusion time scale smaller than the reaction time scale. At low enough flow rates, the residence time in the device will also be much longer than the time required for the analyte to bind at the surface, such that we also enter in a convection-limited regime. This behavior can be characterized by a convection/reaction number,

$$\zeta_L \cdot Da = \frac{DL}{Uh^2} \cdot \frac{k_{on} C_{s0} h}{D} = \frac{k_{on} C_{s0} L}{Uh}, \tag{2.26}$$

which compares the time scale for an analyte molecule to either react at the surface or exit the surface reaction area by convection, assuming fast axial diffusion. In certain notations, this convection/reaction number is known as Damköhler's first number (the diffusion/reaction Damköhler number (Da) used throughout this paper being the second one). When $\zeta_L \cdot Da << 1$, the transport is reaction limited, while it becomes convection-limited for $\zeta_L \cdot Da >> 1$. In the latter case, binding occurs near the entrance, totally depleting the bulk. As the surface saturates, more sample will move further down the channel to bind and saturate the walls. The result is a bulk concentration front propagating in a wave-like fashion throughout the channel. This behavior can be derived from the transport equations (Table 2.1) and characterized using a kinematic wave – or shock solution – approach [*103*].

2.4.2. Determination of the propagation velocity

When an analyte solution is flowed over a high capacity surface ($\varepsilon << 1$), the solution profile in the bulk of the channel reaches a quasi steady-state above the reaction surface. After a time on the order of the reaction time scale has elapsed, the surface starts to saturate and a pattern is created which propagates axially at a constant velocity smaller than the fluid velocity U. This behavior can be simply modeled for limit cases very far behind and ahead of the moving front. It can be interpolated for cases in between. The analytical approach to this task is analogous to capture in a packed bed in liquid chromatography, since both cases exhibit high surface to volume ratio. The elution time for the solution can therefore be calculated using a similar approach and depends on the relative adsorption capacity ε and the tightness of binding $\bar{K}_D$.

A simple model of the adsorption can be derived from a mass balance between the bound mass and the bulk mass along the channel. By integrating the normalized transport equation found in eq. (2.5) across the channel height and using the normalized boundary condition in eq. (2.7), the bulk transport equation becomes

$$\frac{\partial \Theta_b(\zeta)}{\partial \zeta} + \frac{\partial \overline{\Theta}(\zeta,\tau)}{\partial \tau} + \frac{n_w}{\varepsilon} \cdot \frac{\partial \Theta_s(\zeta,\tau)}{\partial \tau} = 0, \tag{2.27}$$

where $\overline{\Theta}(\zeta,\tau)$ is the cross section-averaged concentration and $\Theta_b(\zeta,\tau)$ is given in eq. (2.10). Applying a dimensionless variable change of the form

$$\xi = \zeta - \frac{U_{eff}}{U}\tau, \tag{2.28}$$

the problem can be expressed in the referential of the moving concentration front.

$$U\frac{\partial\Theta_b(\bar{\xi})}{\partial\bar{\xi}}-U_{eff}\frac{\partial\overline{\Theta}(\bar{\xi})}{\partial\bar{\xi}}-U_{eff}\frac{n_w}{\varepsilon}\cdot\frac{\partial\Theta_s(\bar{\xi})}{\partial\bar{\xi}}=0, \tag{2.29}$$

The effective propagation velocity U_{eff} can be determined by finding a relationship between $\overline{\Theta}(\zeta,t)$, $\Theta_b(\zeta,\tau)$, and $\Theta_s(\zeta,\tau)$ and by applying the boundary conditions very far upstream and downstream of the moving front to yield

$$U_{eff}=\left(1+\frac{n_w}{\varepsilon\cdot(1+\overline{K}_D)}\right)^{-1}U. \tag{2.30}$$

The front of bulk concentration $\Theta_b=1$ will thus propagate at a velocity much inferior to the fluid velocity when $\varepsilon \ll 1$, which is normally the case. Moreover, it can be observed that U_{eff} is minimal when $\overline{K}_D \to 0$. This is to be expected since in this case, no ligand escapes the bed. The mathematical derivation of this result from the full transport equations is provided in section 2.7.2.

2.4.3 Wave profile determination for limiting cases

The analysis provided in the previous subsection only provides the propagation velocity but does not reveal anything about the profile of the kinematic wave inside the device. For arbitrary transport conditions, the exact shape of the wave front can only be determined numerically. However, two limiting cases exist whether the transport to the surface is diffusion or reaction-limited. These wave profiles are necessary to predict the capture fraction in a device and are discussed below.

2.4.3.1. Fully diffusion-limited wave profiles

Under fully diffusion-limited conditions, the flux to the surface can be assumed constant throughout the device, as in eq. (2.16). In the reference frame of the moving concentration front, the bulk concentration profile propagating inside the channel can therefore be approximated by a two piece-wise continuous profile:

$$\Theta_b(\bar{\xi}) \sim \begin{cases} 1, & \bar{\xi} < -\bar{\xi}_{shift} \\ \Theta_b(\bar{\xi}), & \bar{\xi} > -\bar{\xi}_{shift} \end{cases}, \tag{2.31}$$

where $\bar{\xi}_{shift}\bar{t}_d = \left[\varepsilon(1+\bar{K}_D)\right]^{-1}\bar{t}_d$ is the saturation time of the surface under diffusion-limited conditions, and Θ_b is given in eq. (2.25). The peak shift $\bar{\xi}_{shift}$ is explained by the time delay required for the surface to reach its steady state profile in the reference of the wave front before it starts propagating.

Numerical simulations presented in Fig. 2.5 confirm both the profile predicted by eq. (2.31) and the peak shift $\bar{\xi}_{shift}$ from the origin $\bar{\xi} = 0$. The time dependent capture fraction of a bed of length L therefore becomes

$$f(t) \equiv 1 - \frac{\Theta_b(L)}{\Theta_b(0)} = \left\{1 - \Theta_b\left(\frac{L}{Pe \cdot h} - \frac{U_{eff} \cdot t}{U \cdot \bar{t}_d} + \frac{1}{\varepsilon(1+\bar{K}_D)}\right)\right\} \text{ when } Da >> 1. \tag{2.32}$$

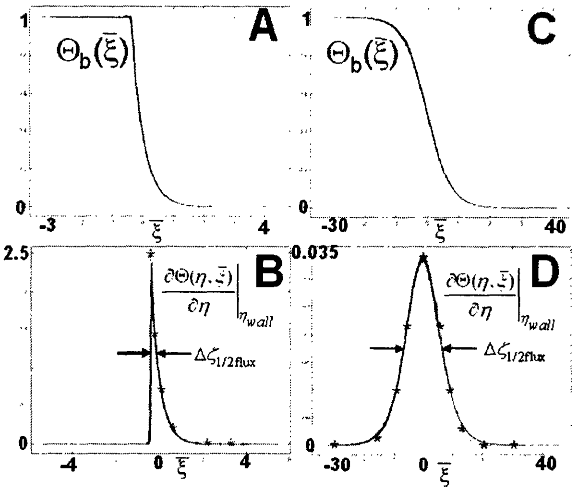

Figure 2.5: Numerical simulation of bulk concentration and flux peak profiles for limiting transport situations (n_w=2). A-B) Fully reaction-limited case. Da=0.14, $\overline{K}_d$=0. C-D) Fully mass transfer-limited case. Da=100, $\overline{K}_d$=0. The star-dotted curves in B and D represent the analytic models derived respectively in eq. (2.52)and eq. (2.31).

2.4.3.2. Fully reaction-limited wave profiles

When the transport is fully (reaction-limited, the concentration profile resembles one found in chromatography columns under continuous sample feed [*104*]. The wave front can be accurately approximated by a complementary error function [*99*] of the form

$$\Theta_b = \frac{1}{2} erfc\left(\xi / \sqrt{2}\sigma\right). \tag{2.33}$$

Where the standard deviation, representing the sharpness of the front (sharpest when $\sigma \rightarrow 0$), is given by

$$\sigma = \sqrt{\frac{2}{\pi}} \cdot \frac{1}{n_w \overline{k}_{d/r}(Da_{eff})}. \tag{2.34}$$

Da_{eff} is the effective Damköhler number found at the point of half saturation of the surface, or

$$Da_{eff} = \frac{k_{on}(C_{s0} - C_{eq}/2)h}{D} = Da \cdot \frac{1/2 + \overline{K}_D}{1 + \overline{K}_D}. \tag{2.35}$$

The details of the derivation are found in section 2.7.3. In Fig. 2.5B, the concentration profile found in eq. (2.33) is confirmed by numerical simulations. The corresponding capture fraction by a bed of length L is therefore expressed by

$$f(\tau)=1-\frac{\Theta_b(L)}{\Theta_b(0)}=\frac{1}{2}\left(1+erf\left\{\frac{\zeta_L-U_{eff}\tau/U}{\sqrt{2}\sigma}\right\}\right),\text{for } Da<<1. \tag{2.36}$$

In all cases, for these profiles to be observed, the condition of fully developed regime for ζ (see Fig. 2.2 and Fig. 2.4), must be respected.

2.4.4. Numerical simulation of the propagating front

A 2D model was created in FEMLAB (Appendix A2) to confirm the theoretical prediction of the propagation velocity of the concentration front and its general profile. The model is based on the general case of protein depletion from a solution in a binding assay performed in a narrow device in the fully developed region. To make the simulations physically relevant, the geometry, the experimental conditions, and the data on protein kinetics are taken from the literature (Table 2.2). The first simulation characterizes the passivation of channel walls using biotinylated bovine serum albumin (BSA) reacting with a wall coating of streptavidin in the conditions of a suspended microresonator. The parameters describing the model are, in this case, $Da=0.14, Pe=17, \varepsilon=0.001$ and $\overline{K}_D\sim 0$ (Table 2.2, entry 2). The reaction occurs equally at both walls and is therefore symmetric. Modeling results are presented in Fig. 2.6 in terms of the bulk concentration $\Theta_b(\zeta,t)$, the normalized flux at the wall $\partial\Theta(\eta_w,\xi,t)/\partial\eta$, and the surface concentration of bound BSA normalized to the total number of binding sites $\Theta_s(\zeta,t)$. The time scale chosen is from 100 to 2000 seconds where each curves is taken at a 50s interval. In each of these curves, the time scale $\bar{t}_{sat}=(k_{on}C_0+k_{off})^{-1}$~85s appears to be the time necessary for the wave to enter its self-propagating steady state (see discussion section).

In Fig. 2.6C, the emphasis is on early times (<0.15 s) to capture the development of the flow on the time scale of diffusion across the channel height. In this time frame, the steady state value of the bulk concentration in the absence of surface saturation is also plotted (Fig. 2.6A, line with star markers). The approximation is in agreement with the numerical model when a few diffusion time scales have elapsed (section 2.3.5.2.).

A similar analysis is provided in Fig. 2.7 for the case of affinity capture at the bottom wall of a 50-μm thick microfluidic channel. Given the larger diffusive time scale due to the increased channel thickness, the fully developed region will be reached at much higher length scales in this simulation. Indeed, to obtain this effect, the length of the capture bed would have to be of at least L=1cm ($\zeta \sim 0.7 >> \zeta_{crit}$) instead of 0.1 mm as presented in the original BIACORE experiment [*105*]. In such a device, a ζ value of 5 corresponds to a length L=7.5cm. The simulation parameters for this particular application are then defined by $Da = 10$, $Pe = 335$, $\varepsilon = 0.07$ and $\bar{K}_D = 0.14$ (Table 2.2, entry 1). The reaction takes place only on one side wall in this case.

In both cases, if the transport of the solution above the reactive surfaces can indeed be characterized using an expression depending only on ε and $\bar{K}_D$, as derived in eq. (2.32), all the time lines should merge into the same curve, representing the shape of the wave front, when they are presented in the reference frame of the propagating wave. To illustrate this behavior, the data is presented again with the variable change introduced in eq. (2.28). Results are presented in Fig. 2.6C'-E' and Fig. 2.7C'-E'. They clearly indicate such a convergence after long enough times after the analyte has entered the channel.

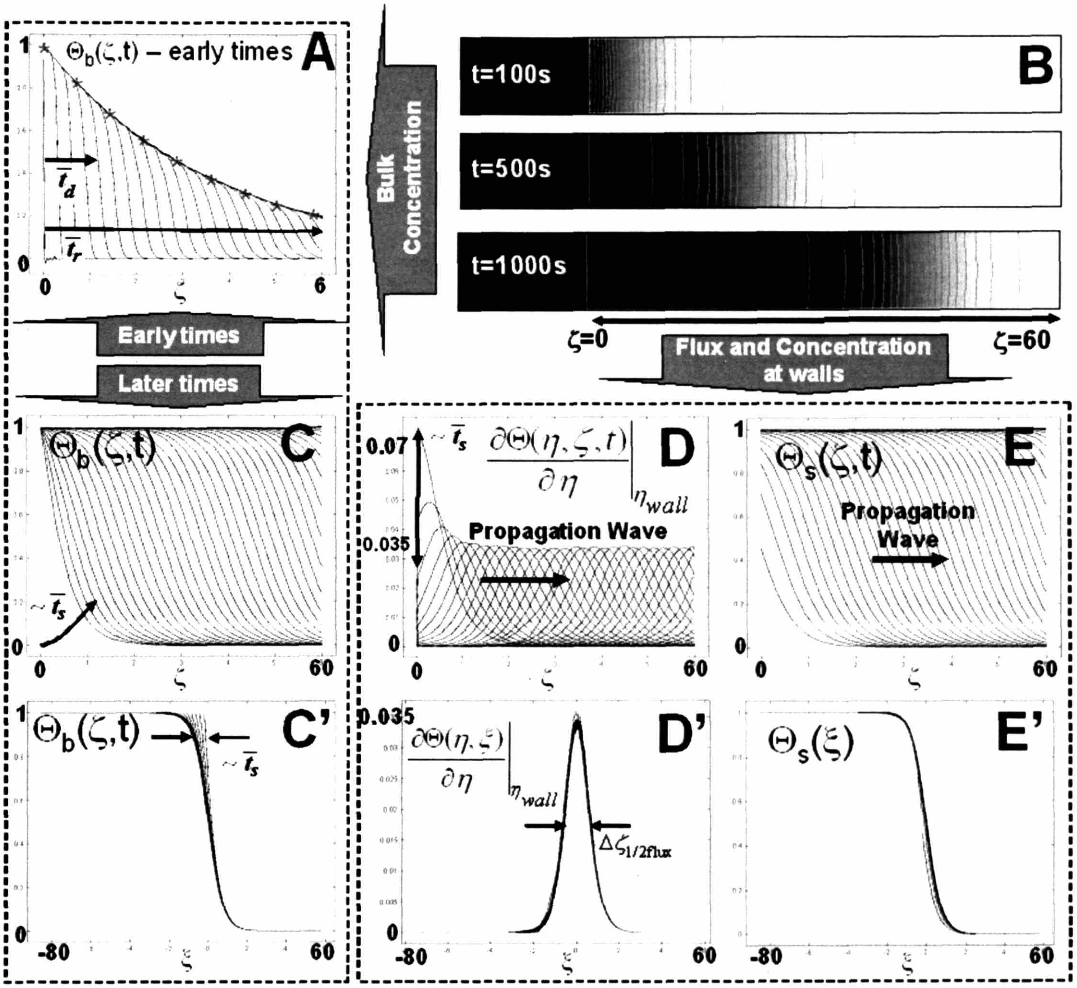

Figure 2.6: Numerical simulation of flow of biotinylated bovine serum albumin (BSA) between streptavidin-coated walls. The geometry and experimental conditions are taken to simulate the suspended microresonator. A) Bulk Concentration profile for times ranging from 0 to 0.15s (Δt=0.005s). The star-dotted line is a fit of the fully developed model for Da=0.14 ($n_w \bar{k}_{d/r} = 0.27$). B) FEMLAB simulations of flow for three different time points: 100s (about the saturation time scale), 500s and 1000s (above saturation time scale and in the propagation wave regime). The gray lines represent concentration isotherms. C) Bulk Concentration $\Theta_b(\zeta,t)$ as a function of ζ for times ranging from 50 to 2000s (Δt=50s). D) Normalized flux at the walls for a time range identical to A. E) Normalized surface concentration of bound BSA (with respect to the total number of binding sites). Time range identical to A. C'-E') Transport simulation in the reference frame of the propagation wave of velocity U_{eff}, where $U_{eff}/U = 5\times10^{-4}$. The various time lines converging to a same value after a few time scales $\bar{t}_{sat} = (k_{on}C_0 + k_{off})^{-1}$ illustrate clearly the development of a kinematic wave.

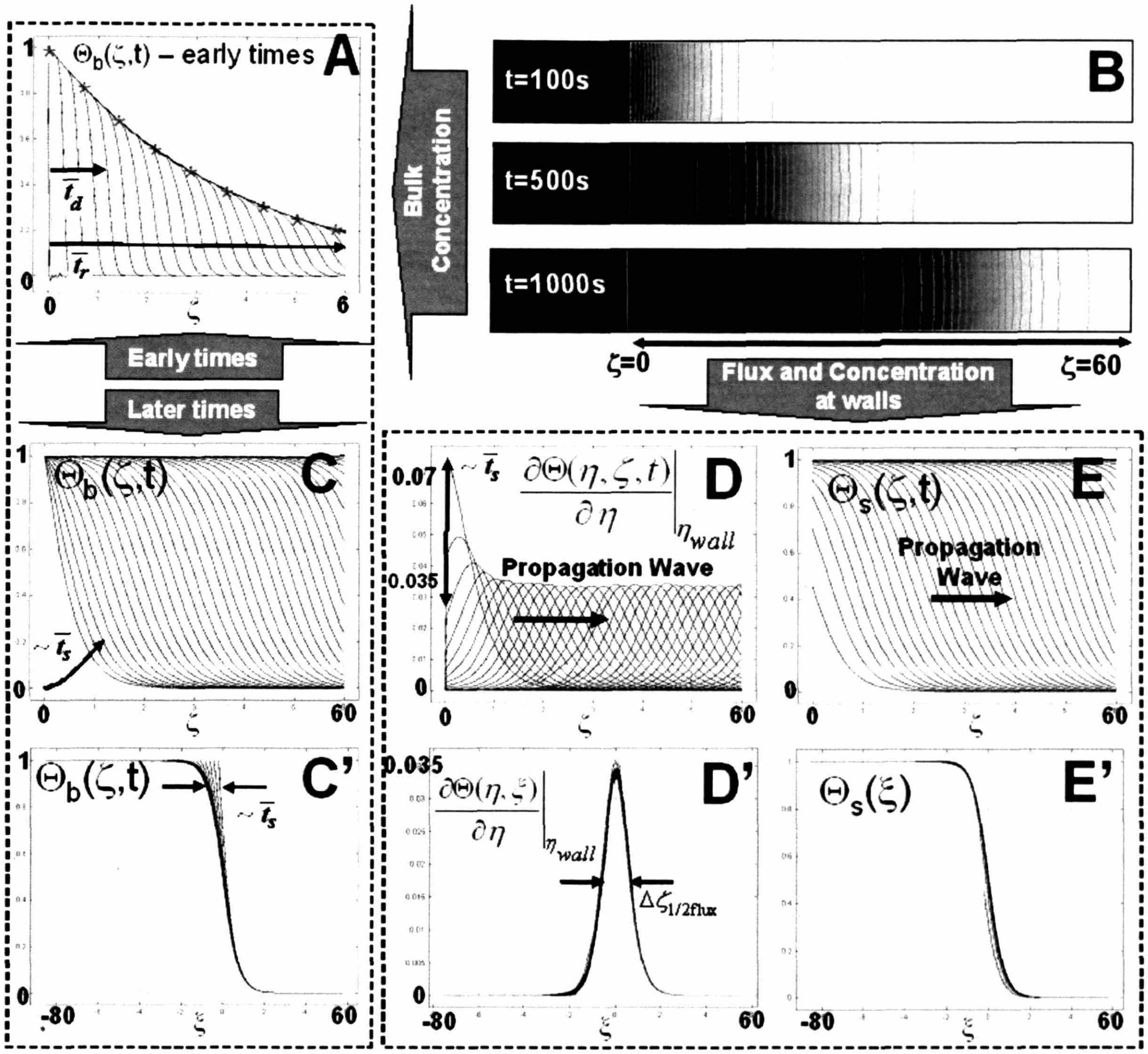

Figure 2.7: Numerical simulation of flow of antigens (A33 protein) in a 50 -μm thick channel in the fully developed regime. The lower wall is coated with corresponding antibody (asymmetric reaction). A) Normalized bulk concentration $\Theta_b(\zeta,t)$ as a function of the diffusive/convective length ζ for early time points (t= [0, 50] by steps of 10s). The star-dotted line is a fit of the fully developed model for Da=10 ($n_w\bar{k}_{d/r}$=1.99). B) FEMLAB™ simulation of flow for three different time points: 100s, 500s and 1000s. The gray lines represent concentration isotherms. C) $\Theta_b(\zeta,t)$ vs ζ for time points in the propagation wave regime (t= [0,2000] by steps of 50s). D) Normalized flux at the antibody bed (same time points as C). E) Normalized surface concentration of bound antigen. C'-E') Transport simulation in the reference frame of the propagating front, where $U_{eff}/U = 0.074$.

2.5. Discussion

In microfluidics, most analyses assume that, at high enough flow rates, a mass transfer boundary layer will exist in the device and that the models developed for the kinetic analysis of the Biacore sensor will apply. This is not always the case. As the channels become thinner, depletion from the bulk becomes important and the "entrance region" assumption can no longer be used. Inspection of Fig. 2.2 indicates that the model breaks down much before $\zeta = 1$. By plotting the absolute error of the bulk concentration for the fully numerical model versus the existing asymptotic solution, a model-selection criterion, i.e., a critical value of ζ above which the fully developed model provided a better approximation than the entrance model, arose naturally. The critical values are ζ_{crit}=0.06 and ζ_{crit}=0.22 for the symmetric and asymmetric reactions, respectively. This transition physically corresponds in the channel to the disruption of the mass transfer boundary layer to enter the regime where the depletion in the bulk becomes significant (see Fig. 2.2A). Therefore, the validity of the entrance region models developed for most real-time detection systems, including SPR systems, breaks down at ζ_{crit}.

Reducing the channel height also drives the transport towards the reaction-limited or even convection-limited regimes. The reaction-limited regime is captured in the Damköhler number. Since $Da \equiv k_{on} C_{s0} h / D$ for bimolecular surface reactions, as the channel height increases, Da will decrease correspondingly, to a point where the mass transfer will become fully reaction-limited for thin enough structures. Alternatively, the reaction can be limited by convective transport ($\zeta \cdot Da >> 1$) or not ($\zeta \cdot Da << 1$) inside the device. Once again, this effect is more likely to appear at small channel height since the convection/reaction number $\zeta \cdot Da \propto h^{-1}$.

The two examples modeled and presented in the results section are used to demonstrate the existence of the convection-limited regimes. Though they are of different length, channel height and kinetic properties, both fulfill the criterion $\zeta \cdot Da >> 1$. Further physical insights can be gained from considering the 5 time scales present in this transport problem (diffusion $\bar{t}_d$, reaction $\bar{t}_r$, convection $\bar{t}_c$, saturation $\bar{t}_{sat}$, and propagation $\bar{t}_p$). For the convection-limited (or wave) regime to occur, both the time taken for the analyte to diffuse across the channel ($\bar{t}_d$) and the time for it to react at the surface ($\bar{t}_r$) must be smaller than the time for the analyte to exit the reactive region ($\bar{t}_p$). No restriction is required on the relationship between $\bar{t}_d$ and $\bar{t}_r$. Consequently, any Da can yield a convection-limited regime.

In the case of reaction in the suspended microresonator [*68*], the diffusion time scale $\bar{t}_d = h^2/D \sim 20\,\mathrm{ms}$ is the shortest of all and represents the time scale after which steady state is reached in the bulk and, therefore, the Graetz formulation of the problem can be used (Fig. 2.6A). The second time scale, $\bar{t}_r = (k_{on}C_{s0}/h)^{-1}$=0.12s, is still much smaller than the convection time scale $\bar{t}_c = L/U = 1\,\mathrm{s}$, such that $\bar{t}_d << \bar{t}_r << \bar{t}_c$. The saturation time constant $\bar{t}_{sat} = (k_{on}C_0 + k_{off})^{-1}$ ~85s shows how quickly the propagation wave will develop throughout the device. Since we are in the convection-limited regime, the propagation time constant of the wave front is physically meaningful and can be calculated to be $\bar{t}_p = L/U_{eff}$ ~1530s. The ratio $\bar{t}_p/\bar{t}_c = U/U_{eff}$ indicates by how much the flow of analytes is retarded compared to the fluid flow. This ratio is analogous to the number of theoretical plates used in chromatography to determine a column's separation efficiency (see section 2.7.2). In this case, the retardation factor is of 1530 times. In other words, while the fluid will take one second to traverse the reactive region, we predict that the analyte will propagate through the channel in 24 minutes given the values of ε and $\bar{K}_D$ provided. The modeling results are presented (Fig. 2.6C'-E') in the reference frame of the bulk solution propagating at velocity U_{eff} by using the change of variable introduced in eq. (2.28). The quick convergence of the lines into one proves the accuracy of the approximation on U_{eff} made in eq. (2.30).

The on-chip immunoassay described in Fig. 2.7 can be analyzed in the same fashion. The various time scales in this case are $\bar{t}_d$=25s, $\bar{t}_r$=3s (now transport to surface is diffusion-limited), and $\bar{t}_c = 112\text{s}$. Though the propagation time scale $\bar{t}_c$ is much larger in this second case, the retardation factor, $U/U_{eff} = 13.5$ is 113 times smaller in this case. Thus the wave front travels faster in the immunoassay than in the resonator, though the fluid velocity is higher in the latter. This behavior can be explained by the lower adsorption capacity (higher ε), the lower equilibrium capture fraction (87% instead of 100%), and the presence of only one reactive wall in the former case (Fig. 2.7).

In the perfectly convection-limited case, the propagating front is a step function between a region where $\Theta_b(z < U_{eff}t) = 1$ and $\Theta_b(z > U_{eff}t) = 0$. However, operating in non ideal conditions, the front of concentration $\Theta_b = 1$ will be preceded by a region where the surface is partially saturated whose characteristic length can be estimated. Thus the scaling of eq. (2.25) implies that a concentration decay length scale $\zeta_p \sim (n_w \cdot \bar{k}_{d/r})^{-1}$ will be perturbed during the formation of the wave. From this diffusive/convective length scale, it is possible to extract the propagation length scale required before the wave is fully formed

$$l_p \sim \frac{U \cdot \bar{t}_d}{n_w \cdot \bar{k}_{d/r}}, \tag{2.37}$$

For instance, in the structure analyzed in Fig. 2.6, $n_w \cdot \bar{k}_{d/r}(Da = 0.14) = 0.27$, $U = 2$ mm/s and $\bar{t}_d = 0.02$ s, which yields $l_p \sim 0.2$ mm (10% of the channel length).

Once the wave profile has reached steady state, the same scale can be used to determine the length of the partially saturated moving front. Indeed, when $\bar{t}_r << \bar{t}_d$ (or Da>>1) as in Fig. 2.5B, the flux curves are exponential in nature and their full width at half maximum (FWHM) becomes

$$\Delta\zeta_{1/2\,\text{flux}} \sim \frac{2\ln 2}{n_w \cdot \bar{k}_{d/r}(Da)} = \frac{1.39}{n_w \cdot \bar{k}_{d/r}(Da)}. \tag{2.38}$$

The case of the immunoassay falls in that category (*Da*=10), and $n_w \cdot \bar{k}_{d/r}(Da) = 1.99$ (from Fig. 2.3), $U = 0.67$ mm/s and $\bar{t}_d = 25$ s, which yields $l_p \sim 8.3$ mm and $\Delta\zeta_{1/2\text{flux}} \sim 1.39 / k_{d/r}(Da)$=0.82.

However, when $\bar{t}_d << \bar{t}_r$ (or Da<<1) the flux curves are Gaussian in shape and their FWHM is therefore approximated by

$$\Delta\zeta_{1/2\,\text{flux}} \approx 2\sigma\sqrt{2\ln 2} = \frac{1.88}{n_w \cdot \bar{k}_{d/r}(Da_{eff})}. \tag{2.39}$$

Thus for the width at half maximum of the flux peak in the resonator (*Da*=0.14), we obtain $\Delta\zeta_{1/2\text{flux}} = 1.88 / \bar{k}_{d/r}(Da/2) = 13.7$.

In all cases, for a wave to be observed, the condition on the reaction zone length $L >> l_p$ must be respected. Given also that $l_p \propto h^2$, a wave front is therefore much less likely to appear in thicker microfluidic channels. As for the case of open-tubular (capillary) chromatography, it is known that the presence of a normalized dissociation constant $\bar{K}_D$ which depends on the bulk concentration would yield asymmetric peaks in a separation process (Scott 1992). Under these circumstances, the chromatographic analysis becomes much more difficult.

2.6. Conclusion

Transport problems involving flow through devices and surface capture abound in the field of microfluidics. It can be difficult to select the appropriate model to characterize device performance as devices vary greatly in geometries and operation ranges. In many applications, it is not possible (or simply not desirable) to operate under conditions that yield a mass transfer boundary layer. This contribution establishes the limits of the entrance region models developed for SPR (Biacore) analysis. Through fully numerical simulations and analysis of the classical transport equations, the intervals of validity of these models were established. Most importantly, the analyses and modeling in this paper focus on fully characterizing transport to surfaces in the absence of boundary layer and proposes a simple approach to obtain the diffusion/reaction mass transfer coefficient $\overline{k}_{d/r}(Da)$. Application of these coefficients allows accurate mapping of the bulk and surface concentrations along the channel and helps determine the expected time for a surface to saturate. The formation of a moving concentration front in long channels is also investigated and its propagation velocity is linked directly to common experimental parameters. Finally a few examples from the microfluidics literature provide concrete examples of the use of the models.

As the field of total biochemical analysis evolves, fluidic modules are bound to be integrated on a very large scale, both in series and in parallel, and analysis times will need to be controlled carefully. Saturation time scales and capture fractions in flow through reactions will be important parameters to optimize. Moreover, devices will tend to shrink in size to yield faster analysis times and more portability, but at the same time, will render boundary layer models useless as the length scale of these layers would be significantly larger than the channels themselves. This study represents a start towards systematizing the existing knowledge and identifying the key parameters to consider when designing microfluidics-based systems.

2.7. Analytic Supplement to Chapter 2

2.7.1. Algebraic proof of the faster convergence of transport coefficients at lower Damköhler numbers

The proof is made by showing that the higher order contributions to the transport coefficients are given a lesser weight (coefficients $A(Da)_i$) in the sum as Da decreases. To do so, the generalized reaction/diffusion transport coefficients are expanded using eq. (2.13) and the eigenfunction expansion found in Table 2.3 to give

$$\bar{k}_{d/r}(Da,\zeta)=\frac{1}{n_w}\frac{\sum_{i=1}^{\infty}A(Da)_i\frac{\lambda_i^2(Da)}{6}\exp(-\frac{\lambda_i^2(Da)}{6}\zeta)}{\sum_{i=1}^{\infty}A(Da)_i\exp(-\frac{\lambda_i^2(Da)}{6}\zeta)} \tag{2.40}$$

When $\zeta\to0$ and $Da\to\infty$, , eq. (2.40) slowly converges to the value of the entrance region Sherwood number Sh_E found in eq. (2.14). Since $\lambda_{i+1}^2/\lambda_1^2\approx i^2$, all terms but the first ones can be neglected. Keeping the first two terms of the expansion, the order of magnitude of the error on $\bar{k}_{d/r}(Da,\zeta)$ will be determined by the ratio of the two first expansion coefficients A_2/A_1 at $\zeta=0$, assumed to be small (yet much larger than $A_{i>2}/A_1$).

$$\bar{k}_{d/r}(Da,\zeta=0)\approx\frac{\lambda_1^2(Da)}{6}\cdot\left(\frac{1+\frac{A_2}{A_1}\frac{\lambda_2^2(Da)}{\lambda_1^2(Da)}}{1+\frac{A_2}{A_1}}\right)\approx\frac{\lambda_1^2(Da)}{6}\left\{1+\left(\frac{\lambda_2^2(Da)}{\lambda_1^2(Da)}-1\right)\frac{A_2}{A_1}+O\left(\frac{A_2^2}{A_1^2}\right)\right\} \tag{2.41}$$

where the leading order corresponds to the relative error on $\bar{k}_{d/r}(Da)$

$$\mathrm{err}(\%) \sim \left(\frac{\lambda_2^2(Da)}{\lambda_1^2(Da)} - 1 \right) \frac{A_2}{A_1} \tag{2.42}$$

From eq. (2.40), we observe that the error on $\bar{k}_{d/r}(Da,\zeta)$ is maximum at $\zeta=0$, implying that the error calculated in eq. (2.42) represents an upper bound. The error on $\bar{k}_{d/r}(Da)$ is computed and compared in Table 2.5 for $Da \to \infty$ and $Da = 1$, and for both symmetric and asymmetric reactions. It shows that the first term approximation become even more appropriate at smaller Damköhler numbers, as the first expansion coefficient $A(Da)_1$ will tend to 1, while A_2/A_1 decreases.

Table 2.5: Numerical values of eigenvalues and eigenfunction expansion coefficients for selected Damköhler numbers. The reaction/diffusion transport coefficient and the maximum relative error committed by using the fully developed region asymptotic model instead of the entrance region model is also provided.

	$[a_1, a_2]$	$[A_1, A_2]$	$[\lambda_1, \lambda_2]$	$\bar{k}_{d/r}(Da)$	Error
Symmetric, $Da \to \infty$	[1.20083, -0.299161, 0.160826, -0.107437, 0.0796461]	[0.910352, 0.0531425, 0.0152789, 6.80881E-3, 3.73980E-3]	[6.72638, 22.6794, 38.6730, 54.6706, 70.6695]	3.77035	60%
Symmetric, $Da \to 1$	[1.05440, -0.0702248, 0.0231974, -0.0116351, 7.04946E-3]	[0.996534, 3.00272 E-3, 3.20666E-4, 8.02227E-5, 2.93823E-5]	[3.10203, 17.9834, 33.7725, 49.6771, 65.6209]	0.801883	10%
Asymmetric, $Da \to \infty$	[1.24843, -0.383224, 0.226317, -0.160582, -0.124437]	[0.895561, 0.0604998, 0.0180406, 8.17716E-3, 4.53590E-3]	[3.81867, 11.8972, 19.9241, 27.9383, 35.9473]	2.43036	59%
Asymmetric, $Da \to 1$	[1.80850, -0.0177920, 0.0897772, -2.03146E-3, 0.0321345]	[0.992098, 6.67512E-3, 8.26276E-4, 2.19425E-4, 8.30061E-5]	[2.08371, 9.67057, 17.5723, 25.5244, 33.4952]	0.723641	14%

2.7.2. Development and calculation of the propagation velocity of a kinematic concentration wave front

After several diffusion or reaction time scales have elapsed, whichever the longest, the bulk concentration profile, in the reference frame of the propagating wave front, will reach a steady-state due the constant adsorption along the walls. The velocity-averaged and cross section-averaged concentration will become the same, and $\overline{\Theta}(\zeta,\tau)=\Theta_b(\zeta,\tau)$ can be assumed valid at all time $t >> \bar{t}_d$. However, this simplification is not required to obtain the general result for the propagation velocity.

The propagation wave aspect appears when the equations are expressed with respect to the reference frame moving at a velocity U_{eff}, at which the concentration profile propagates once it has reached steady state. This approximation is valid for times for ζ sufficiently large and for $t >> (k_{on}C_0 + k_{off})^{-1}$ the saturation time scale at the surface. This velocity is now unknown but can be determined by first using the change of variable

$$\xi = z - U_{eff}t, \tag{2.43}$$

in such a way that the solution can be represented by an ordinary differential equation with dependent variables of the form

$$\Theta(z,t) = \Theta(\xi), \tag{2.44}$$

These satisfy the new boundary conditions

$$\Theta_b = \overline{\Theta} = 1,\ \Theta_s = \frac{1}{1+\bar{K}_D},\ \frac{d\Theta_b}{d\xi} = \frac{d\overline{\Theta}}{d\xi} = \frac{d\Theta_s}{d\xi} = 0 \text{, as } \xi \to -\infty \tag{2.45a}$$

$$\Theta_b = \overline{\Theta} = \Theta_s = 0, \frac{d\Theta_b}{d\xi} = \frac{d\overline{\Theta}}{d\xi} = \frac{d\Theta_s}{d\xi} = 0 \text{, as } \xi \to \infty. \tag{2.45b}$$

In a first order ODE, these conditions cannot be satisfied all at once. However, if the problem exhibits a kinematic wave behavior, then eqs. (2.43) and (2.44) are appropriate. The solution found is a shock (or weak solution), exhibiting a discontinuity. An extensive study of their behavior and applications is provided by Rhee and Amundson [*103*].

With the new change of variable, and expressing ζ and τ in terms of z and t, the flux balance in eq. (2.27) becomes

$$N_{tot}(\xi) = U\frac{d\Theta_b(\xi)}{d\xi} - U_{eff}\frac{d\overline{\Theta}(\xi)}{d\xi} - n_w\frac{U_{eff}}{\varepsilon}\frac{d\Theta_s(\xi)}{d\xi} = 0, \tag{2.46}$$

giving a differential expression of $\Theta_s(\zeta, t)$ as a function of $\Theta_b(\xi)$ and $\overline{\Theta}(\xi)$.

When one is not interested in knowing the exact profile of the propagation wave (i.e. $\Theta_b(\xi)$ and $\Theta_s(\xi)$), but only the velocity of the resulting wave, it can be readily obtained by integrating eq. (2.46) over the whole domain ($\xi = [-\infty, \infty]$). The integration gives

$$\int_{-\infty}^{\infty} N_{tot}(\tilde{\xi})d\tilde{\xi} = n_w\frac{U_{eff}}{\varepsilon}\cdot\left[\Theta_s(\xi)\right]_{-\infty}^{\infty} - U\cdot\left[\Theta_b(\xi)\right]_{-\infty}^{\infty} - U_{eff}\cdot\left[\overline{\Theta}(\xi)\right]_{-\infty}^{\infty} = 0, \tag{2.47}$$

Using the boundary conditions expressed in eq. (2.45a), the result can be rearranged to obtain the key result found in eq. (2.32). To pursue an analogy with chromatography theory, the ratio

$$\frac{U}{U_{eff}} = 1 + \frac{n_w}{\varepsilon}\cdot\left(1 + \overline{K}_D\right), \tag{2.48}$$

represents here the number of theoretical plates in a capillary column inside which bimolecular surface saturation is permitted. However, the standard capillary columns assume purely first order kinetics and further simplify the analysis by assuming that the walls never saturate [*106*] and the standard definition of the number of theoretical plates is defined with K_D replacing $\overline{K}_D$ in eq. (2.48) and assuming the surface never saturates.

2.7.3 Analytic characterization of the wave front and flux peaks under reaction-limited transport

Contrary to the chromatography models, where no surface saturation is assumed, the problem here tackled is in reality highly non linear and the exact expression of the curve shape can only be found through numerical modeling. However, by assuming pseudo steady state in the concentration curves (Fig. 2.6C',5E' and Fig. 2.7C',6E'), the total flux (or the slope of the concentration curve) near the inflection point can be approximated accounting for the partially saturated surface

$$\left.\frac{\partial\Theta_b}{\partial\bar{\xi}}\right|_{\bar{\xi}=0} = -n_w\bar{k}_{d/r}(Da_{eff})\left.\Theta_b\right|_{\bar{\xi}=0} = -n_w\bar{k}_{d/r}(Da_{eff})/2. \qquad (2.49)$$

We note that $\Theta_b = 1/2$ at the inflection point.

We also observe that Fig. 2.6C', 2.5E' and Fig. 2.5C', 2.6E', the curves representing the bulk and surface concentration in the referential of the wave front behave like the complementary error function [*99*]

$$\frac{1}{2}erfc(\bar{\xi}/(\sqrt{2}\cdot\sigma)) = \frac{1}{2}\sqrt{\frac{2}{\pi\sigma^2}}\int_{\bar{\xi}}^{\infty}\exp\left\{-\tilde{\xi}^2\Big/2\sigma^2\right\}d\tilde{\xi} \approx \frac{1}{2}\left\{1-\sqrt{\frac{2}{\pi\sigma^2}}\bar{\xi}\right\},\ \text{if } \bar{\xi}\to 0. \qquad (2.50)$$

By comparing the result in eq. (2.49) with the slope of the complementary error function near $\bar{\xi}=0$, the effective value of σ can be inferred and used to estimate the shape of the wave front.

$$-\frac{1}{2}\sqrt{\frac{2}{\pi\sigma^2}} = -n_w\bar{k}_{d/r}(Da_{eff})/2 \ \Rightarrow\ \sigma = \sqrt{\frac{2}{\pi}}\cdot\frac{1}{n_w\bar{k}_{d/r}(Da_{eff})}, \qquad (2.51)$$

When $\sigma \ll 1$, the function resembles a step function and the wave front becomes ideal.

Finally, the total flux to the surface (Fig. 2.6D' and Fig. 2.7D') being the derivative of the concentration, it is thus normal to observe that the flux peaks are approximately gaussian. On a per surface basis, the flux becomes

$$\frac{1}{n_w}\sqrt{\frac{2}{\pi\sigma^2}}\exp\left\{-\bar{\xi}^2 \Big/ 2\sigma^2\right\} = \frac{\bar{k}_{d/r}(Da_{eff})}{2}\exp\left\{-\frac{\pi}{4}\left[n_w\bar{k}_{d/r}(Da_{eff})\cdot\bar{\xi}\right]^2\right\}, \tag{2.52}$$

This expression is very accurate near the inflection point $\bar{\xi} = 0$ for reaction with small $\bar{K}_D$. Thus the Gaussian peak model can be used with confidence to predict the head size of the wave front for $\bar{K}_D << 1$ and Da<<1, while it only becomes an approximation at larger $\bar{K}_D$'s and Da~1 since eq. (2.49) cannot take dissociation rates into account. For Da>>1, eq. (2.31) (and it's derivative for the flux) must be used.

Chapter 3. Experimental Visualization of Convection-Limited Transport in Microchannels[1]

Chapter Abstract

In this chapter, we describe the conditions under which transport and surface binding of analytes in microfluidic devices become convection-limited, i.e. limited by the influx of analyte to the detection zone. Convection-limitations appear in channels typically of less than 10 microns thick caused by a high relative number of binding sites at the surface compared to the number of analytes in the bulk. The effect is experimentally observed in suspended microresonator sensors and varies in intensity depending on the analyte concentration used.

3.1. Introduction

The study of mass transfer and binding to microchannel surfaces is a crucial part of the development of sensitive on-chip protein sensors such as protein arrays, surface plasmon resonance (SPR) or evanescent wave sensors. In the previous chapters, we provided the theoretical framework which showed that, as channel thicknesses decrease to the micron-size or less, surface transport of biomolecules becomes limited by the influx of analytes in the device instead of either by diffusion or reaction rates (Fig. 3.1). Thus, the commonly used mass transfer

---

[1] We gratefully acknowledge the experimental contribution of Dr. Christine Tsau to setup the experiments, obtain and the video streams and analyze the intensity data.

model developed for SPR[*72*], which assumes transport from the bulk through a mass transfer boundary layer at the surface, breaks down. New models must be developed to account for the chromatography-like transport behavior that appears.

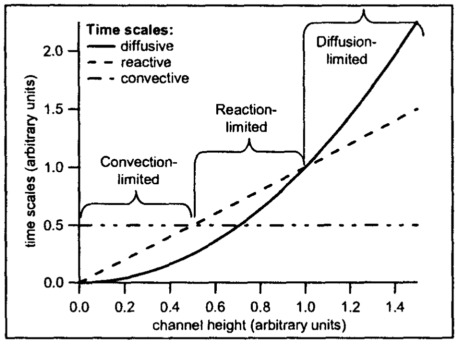

Figure 3.1: Transport time scales for diffusion ($h^2 \cdot D^{-1}$), surface reaction ($h/k_{on}/C_{s0}$) and convection (length/U_{fluid}). When channel height h is too high, reaction kinetics is obscured by diffusion-limitations, when h is too small, kinetics can be obscured by convection-limitations.

In this short chapter, which is meant as an experimental complement to chapter 2, we present the work that provided experimental evidence of the convection-limited transport regime in microfluidic sensors[*107*]. To observe the effect, we use the fluidic network of a suspended microresonator sensor (SMS), a one micron-thick channel buried inside a vibrating cantilever, as developed by Burg et al. [*108*] to measure biomolecular association kinetics. In a first part, the experimental methodology is introduced. Then, the results are exposed and interpreted. Finally, a discussion is provided on the implications of convection-limitations on sensor experimental design.

3.2. Theory

In thinner channels, the amount of available surface receptors (binding sites) per analyte molecule in the bulk becomes larger and incoming sample will be depleted by surface binding. As more sample flows over the surface, binding sites will saturate, thus allowing the free analytes to propagate further down the channel. Convection-diffusion-reaction models have been used to characterize this behavior and show that the front of analyte advances into the channel with an effective velocity U_{eff}, lower than the velocity of the carrying fluid U (Fig. 2.5-2.7). The physical conditions under which this type of transport occurs can be described using Damköhler's first number (see section 2.4.1), the ratio of convective transport to surface reaction rates as

$$Da_I = Da \cdot \zeta = \frac{k_{on} C_{s0}}{h} \cdot \frac{L}{U} >> 1, \tag{3. 1}$$

The velocity and shape of this propagating front has been characterized and shown to depend directly on the channel thickness and the relative amount of available receptors per analyte in the bulk[*109*].

3.2.1. Retardation Factor

In a channel with parallel plate geometry, the amount of time required for an analyte front to move across a surface, taking into account the delay introduced by adsorption is described by

$$\bar{t}_s = \frac{L}{U_{eff}} = \frac{L}{U}\left[1 + \frac{n_w C_{s0}}{h} \cdot \frac{1}{C_0 + K_d}\right], \tag{3. 2}$$

a variant of eq. 2.30, where C_0 [M] and C_{s0} [M·mm] are the concentration of bulk analytes and surface binding sites respectively, n_w is the number of walls where the reaction occurs (0, 1 or 2), h is the channel height (mm), and K_D is the first order equilibrium dissociation constant (mol·mm^{-3}). In the absence of surface interactions (i.e. C_{s0}=0 or n_w=0), the above time scales simplifies to yield the simple convective time scale $\bar{t}_c = L/U$. However, when the channel is sufficiently shallow and the analyte concentration in the bulk is low enough compared to the number of surface receptors available, the analyte front can move orders of magnitude slower than the carrier fluid. The ratio of the bulk velocity to that of the moving analyte front (U_{eff}) is given by

$$n \equiv \frac{U}{U_{eff}} = \left[1 + \frac{n_w C_{s0}}{h} \cdot \frac{1}{C_0 + K_d} \right]. \tag{3. 3}$$

3.2.2. Size of Propagating Wave Front

Beyond the effective propagation velocity of the analytes in the bulk, another parameter is required to fully characterize convection limitations: the length of the propagating wave front (Fig. 3.2). As seen in chapter 2, this dimension can be characterized as a standard deviation in an error function or a characteristic length in an exponential decay, depending on whether the system has a low or high Damköhler number (Fig. 2.5, section 2.4.3). Because of the small dimensions in the devices we use, *Da* tends to be low (~0.1) and the shape of the front can be described with a complementary error function[*99*] of the form:

$$\Theta_b = \left(1 + \frac{K_D}{C_0} \right) \Theta_s \approx \frac{1}{2} erfc\left(\frac{z - U_{eff} t}{\sqrt{2}\sigma_z} \right), \tag{3.4}$$

where σ_z is given in length units as

$$\sigma_z \approx \sqrt{\frac{2}{\pi}} \frac{Uh}{\left[n_w k_{on} (C_{s0} - C_{s-eq}/2) \right]}, \tag{3.5}$$

and $C_{s\text{-}eq}=C_{s0} \cdot C_0/(C_0+K_D)$. Within a proportionality factor, this profile describes both bulk and surface analyte concentration profiles (see Fig. 2.6-2.7)

When the length of the device is on the order of the length of the propagating wave front or larger (L>σ), the wave becomes blurred and tends towards a conventional reaction-limited transport. Alternatively, when the device length is much larger than the front length (L>>σ), the front can be approximated by a unit step.

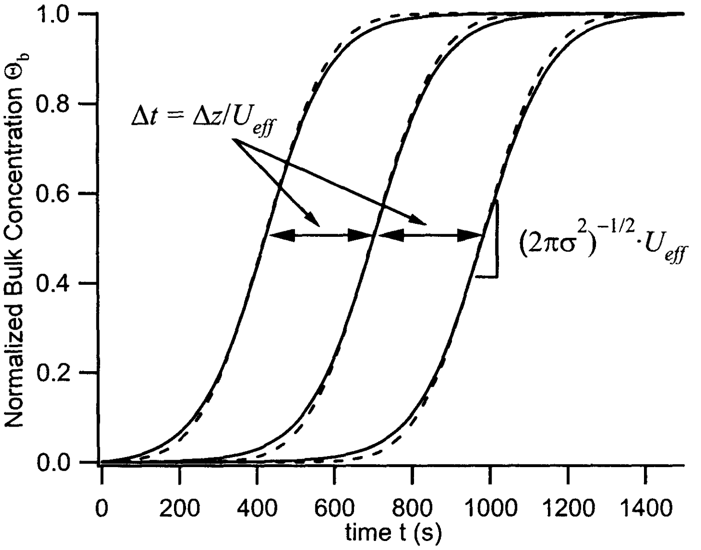

Figure 3.2: Normalized concentration as a function of time at various fixed positions inside a channel. Solid lines: Simulation of the wave front shape using FEMLAB for z=0.6mm, 1mm and 1.4mm, where the experimental conditions are the ones described for the microresonator in Table 2.2, entry 2. Using these values, the standard deviation on the concentration at the front is calculated to be σ_z/U_{eff}= 180s. Dashed lines: Error function predictions using eqs. 3.3 and 3.4.. The very accurate approximation by the error function confirms the accuracy of the front length scale σ_z at low Damköhler numbers (here Da=0.14).

3.3. Experimental Method

Convection-limited transport visualization has been performed in 1μm-thick and 2 mm-long silicon nitride channels used in suspended microresonator sensors (Fig. 3.3). The description of the fabrication protocol to create these microsensors has been described elsewhere[*108*]. The experimental procedure for the visualization consists of first patterning the receptors at the sensors surface, followed by fluorescence intensity image acquired in the form of video streams which were later analyzed.

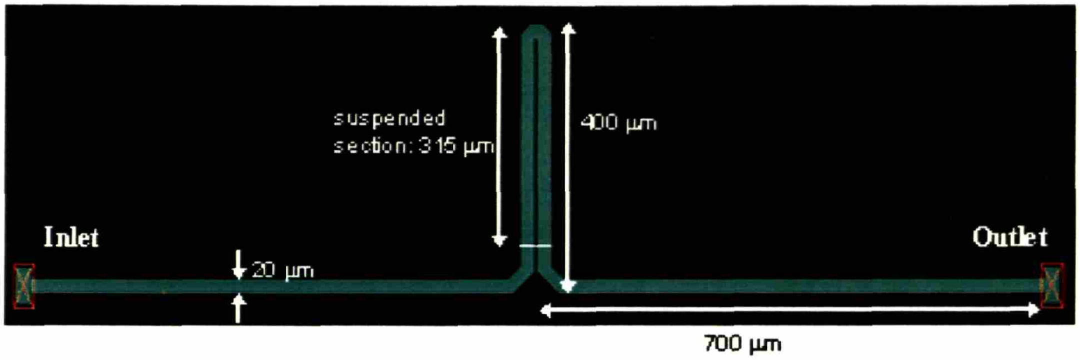

Figure 3.3: Full drawing of cantilever fluidic channel. The whole channel is 2mm long, but the suspended region is only of ~600 µm. The inlet and outlet are linked to larger fludic channels acting at flow control bypasses.

3.3.1. Surface Receptor Patterning

Biotinylated bovine serum albumin (bBSA) was Purchased from Sigma-Aldrich, USA. A saturated solution (1mg/ml of 1x Phosphate Buffer Saline, or PBS) of bBSA was flowed in and allowed to physisorb onto the silicon nitride channel walls for 30 min. The device is rinsed with PBS and 1mg/ml of BSA is then flowed in to block off any unoccupied sites. After 30 min, the device is again rinsed with PBS solution before fluorescent assay is introduced. A close packed monolayer of bBSA (M_w=66 kDa) is reported to have a maximum surface concentration of 7 ng/mm^2[*110*], translating into a surface concentration of C_{s0}=100 fmol/mm^2. Each bBSA contains on average from 7 to 10 biotin molecules (c.f. Sigma-Aldrich).

3.3.2. Fluorescence Binding Assay

Fluorescently-labeled (Rhodamine-stained) streptavidin (SA, Jackson Immunoresearch Labs, PA) in various concentrations was subsequently flowed over the surface for detection using a pressurized vial (Δp= 0.14 atm) as the flow driving force. bBSA-SA kinetics is a well characterized fast (k_{on}=1.2×10^5) and irreversible (k_{off}~0) binding process[*95*] often used as a model reaction for sensor testing due to its robustness. SA molecules display 4 biotin docking sites creating an avidity effect on rate constants (hence the name). In free solutions, the stoichiometry of biotin-SA binding is 4:1. However, when biotin is conjugated to BSA which is later confined to a surface, steric hindrances reduce this stoichiometry to approximately 1:1. The reference experiment in which surface binding does not occur was performed using rhodamine-stained dextran at high concentrations (100 µM). Dextran molecules, which are electrostatically neutral and hydrophilic, are known for their weak interactions with surfaces[*111*]. Images were acquired using an inverted microscope (Nikon Eclipse TE200, Melville, NY) and CCD camera (Roper Scientific Inc., Tucson, AZ) and processed using the MATLAB image processing toolbox (Mathworks Inc., Natick, MA).

3.4. Experimental Results

In the presence of bBSA adsorbed on the walls, the propagation velocity of SA was decreased by a factor of 10-200. As predicted in eq. (3. 3), this retardation effect has been observed to increase with a decrease in the analyte concentration in the range where C_{s0}/C_0h>>1. In a first set of experiments, the concentration of fluorescently-labeled SA was set at C_0=3.6 µM and the time required for the analyte front to cross the device was monitored (Fig. 3.4B). To obtain the retardation factor, it was then compared with the time required for the dextran probes to cross the channel (Fig. 3.4A). For the fluid velocities used (U=0.12 mm/s), the normalized Taylor dispersion coefficient in between parallel plates, ($1+Pe^2/210$) [*83*], is of about 1.03 and therefore negligible, and the effective analyte velocity can be assumed to be that of the fluid (U).

In a second set of experiments, a fresh device was used and the propagating velocity of a front of bulk concentration C_0=0.4 μM was monitored (Fig. 3.4C). Results are summarized in Table 3.1.

Table 3.1: Experimental results summary, calculated retardation factor and resulting estimated surface concentrations of binding sites.

Conditions	Channel fill time (s)	Measured Velocity (μm/s)	Retardation Factor (s.u)	Calculated C_{s0} (fmol/mm^2)
Dextran, C_0=100 μM	6 ± 1	120 ± 20	N.A.	N.A.
Streptavidin, C_0=3.6 μM	100 ± 10	7 ± 1	17 ± 5	29 ± 9
Streptavidin, C_0=0.4 μM	1300 ± 300	0.5 ± 0.1	220 ± 80	44 ± 16

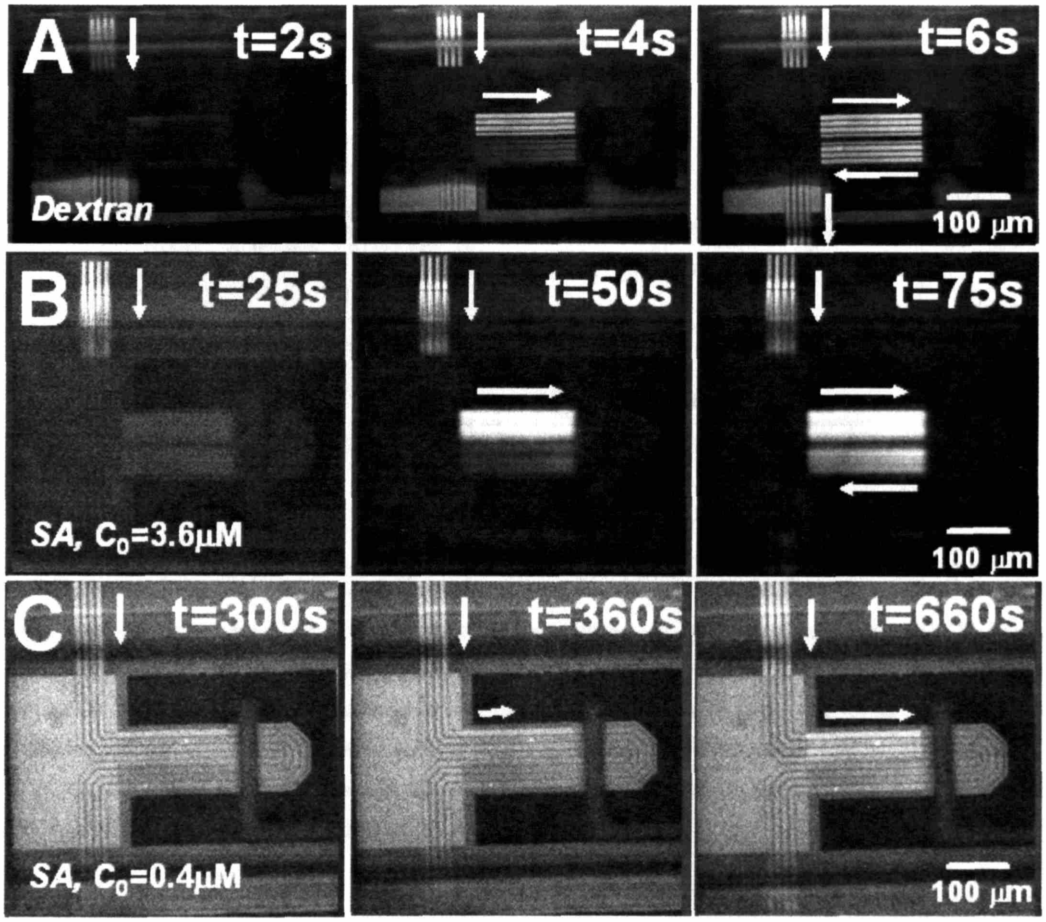

Figure 3.4: Image samples from the microscope video streams used to study the retardation effect. Due to the presence of a chrome layer at the base and tip of the cantilever, fluorescence can only be observed at the inlet, inside the cantilever's central part and at the outlet (see Fig. 3.5A). A) Rhodamine-labeled Dextran flow images for t= 2s, 4s and 6s before fluorescence enters the viewing area (t=0, reference time). Diving the full fluidic path observed (700 μm) by the flow time yields a flow velocity of U= 120 μm/s. B) Rhodamine-labeled SA flow images (C_0=3.6 μM) for t= 25s, 50s, and 75s. The device reached full saturation after 100s, yield an effective analyte velocity U_{eff}= 7 μm/s. C) Rhodamine-labeled SA flow images (C_0=0.4 μM) for t= 300s, 360s, and 660s.

Using the video streams produced to determine the analytes' effective velocity, each frame was analyzed to extract fluorescence intensity data. A rectangle across the width of channel and a 6 pixel-long (corresponding to a length of approximately 4 μm) in the stream-wise direction was averaged at every position of interest inside the channel. Curves displaying the same sigmoidal behavior as in the simulations performed in Fig. 3.2 were obtained.

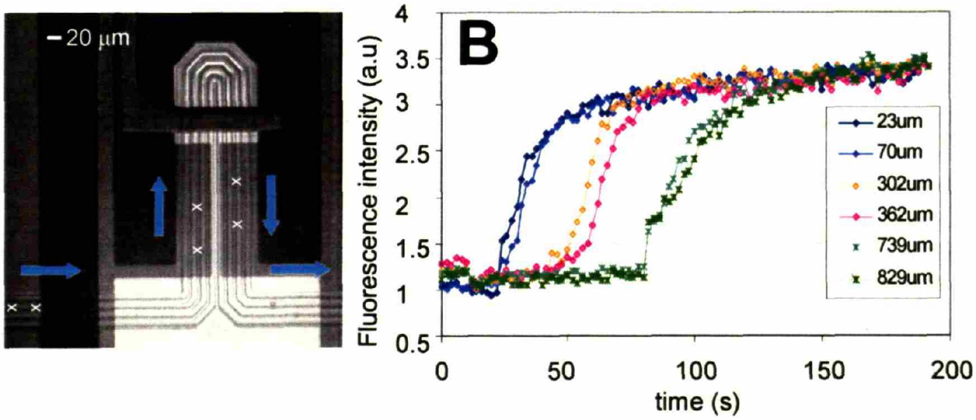

Figure 3.5: Results from the intensity analysis performed on the video stream for the streptavidin flow described in Fig. 3.4B. A) Bright field image of the suspended resonator microchannel used for the measurements. The "X's" represent the fixed points where the intensity data was collected over time (Courtesy of C. Tsau and T.P. Burg). B) Fluorescence intensity data (a.u.) vs time (at fixed point) The effective retardation is calculated by determining the time taken for the front to move from one of the detection points to another and comparing with the measured fluid velocity. Retardation factor in this set of curves is found to be of 20 (C_{b0}=3.6 μM, h=1 μm). The intensity values, as time increases, do not seem to plateau but rather to increase slightly but steadily, indicating some sort of secondary binding activity.

3.5. Discussion

3.5.1. Data Interpretation

In surface-based binding assays in shallow microfluidics devices, the amount of delay in the filling of the channel due to the binding of the analytes at the channel walls is very large and therefore very easy to observe qualitatively. The results from Table 3.1 indicate also that the amount of delay is proportional to the initial concentration of analytes C_0 flowing into the device. However, given the few concentration data points and the large error on computing the filling time, the data can only provide trends and roughly quantify the model's prediction that the relationship between the concentration and the effective velocity is linear. Furthermore, the analysis is incomplete in that the size of the analyte wave front σ_z cannot be reliably characterized using the existing data. The main impediment to that task was the low signal to noise ratio in the binding experiments. The intensity of the recorded signal is highly sensitive to focus. Since the device is not perfectly flat due to built-in lamination stresses, the signal across the device is also likely to vary. Furthermore, residual binding after the wave front has passed (Fig. 3.5B) made the data harder to normalize (see section 3.5.2).

In our experimental manipulations, we were limited by the small number of devices available (less than 10). Once a binding assay is performed in one, it has to be disposed since the cleaning procedures tested unavoidably clogged the micron-size channels.

3.5.2. Measuring Surface Receptor Concentration

In theoretically predicting the extent of convection-limitations in sensors, only one parameter cannot be estimated accurately beforehand: the effective surface concentration of binding sites. Researchers have characterized the number of active binding sites per unit area for various surface chemistries, such as bBSA adsorbed on hydrophobic silanes[*95*], and various IgG adsorbed at hydrophobic surfaces[*112*], alkanethiols[*113*] or crosslinked to a surface via reactive amine chemistry[*82*]. However, knowledge of surface coverage by a protein receptor is not sufficient to calculate the amount of binding sites. A receptor can be bound to the surface, but in such a way that its active sites are inaccessible from the solution. Many molecules used as surface receptors in sensors, such as bBSA, also possess up to 10 biotin molecule per BSA protein, thus creating an avidity effect[*114*] at the surface. This effect implies that the intrinsic associacion rate constant for SA-bBSA complex formation –observable if there is only 1 biotin molecule per BSA- could be much lower than the reported 1.2×10^{5} $M^{-1}s^{-1}$. Since the SA molecule is slightly smaller in size than its bBSA counterpart (53 kDa and 66 kDa respectively) and posses 4 docking sites, it is realistic to expect a binding stoichiometry higher than 1 SA per bBSA molecule. Due to steric effects, the effective association rate constant for secondary binding is usually slower than the first binding event on the bBSA molecule[*114*]. This type of secondary interactions may explain why, in Fig. 3.5B, the intensity measured at any given point still increases linearly by approximately 25% after the passage of the wave front.

3.5.3. Using or Avoiding Convection-Limited Transport in Sensors

As observed experimentally, convection-limited transport has the advantage that 100% of the analyte molecules passing over the sensor's surface are captured. When dealing with low-abundance or highly diluted protein samples, operating in this retention mode may be of benefit to increase the equilibrium signal to noise ratio. The kinetics parameters of a reaction, however, will be masked by the larger convection-limitations and it will consequently be harder to use the sensor to determine kinetics rate constants in that mode. Nevertheless, it is theoretically possible to extract the kinetics with a precise measurement of the moving front size σ_z. As seen in eq.

(3.5), a high k_{on} would translate into a sharp interface at the front (low σ_z) and vice versa. The shape of the front becomes, however, significantly distorted when significant dissociation (k_{off}) is present and the characterization of the rate constants is then no longer straight forward.

Alternatively, if we possess an endless supply of analytes, it is always theoretically possible to increase the flow velocity in a sensor such that convection is no longer a limiting process and kinetics can be elicited. Nevertheless, practical problem are encountered due to the pressure tolerance of these devices to leakage or rupture. Using the analysis performed in this chapter and the previous one, a pressure threshold at which flow will be fast enough to overcome convection-limitations can be calculated. By coupling the condition on Damköhler's first number described in eq. (3. 1) with the Pressure-velocity relationship provided by Hagen-Poiseuille law

$$U = \frac{h^2}{12\mu L}\Delta p\,, \tag{3. 6}$$

we derive the pressure criterion on convection-limitation to be

$$\Delta p >> \frac{12\mu k_{on} C_{s0} L^2}{h^3}\,, \tag{3. 7}$$

where μ is the dynamic viscosity of the carrying fluid (water). Using the experimentally measured values for the above parameters, it can be calculated that, in a 1 micron thick sensor, the condition on the pressure becomes $\Delta p >> 8$ atm. To completely avoid convection-limited analyte transport, pressure on the order of 100 atm would have to be used. This severe limitation on device operation could be eased by increasing the device's height ($\Delta p \sim h^{-3}$) or reducing the overall channel length ($\Delta p \sim L^2$). In any case, device operation could be tested experimentally using a fluorescent assay, as described in this chapter, to verify the nature of analyte transport inside the sensors.

3.6. Conclusion

In the field of integrated on-chip sensor technology, there is a clear trend toward building smaller and smaller devices. Reducing the sensing region's length scale often allows greater sensitivity, a reduction in sample consumption, and a higher sensor density on chip. However, shrinking a device down to the single micron size or smaller changes its fundamental operating modes and, in order to be able to take advantage of such differences, it is necessary to characterize both theoretically and experimentally the new transport behaviors that arise.

In this chapter, through simple experiments, the extent of convection-limited transport was observed experimentally in micron-thick fluidic channels with bimolecular binding reactions at the walls. The effect was directly observed under a microscope through a delay in the channel filling time introduced by the large amount of binding at the surface walls. The effect observed retarded transport by several orders of magnitude and was confirmed to increase with decreasing concentration of analytes in the bulk.

Finally, under the experimental conditions suggested in this study, a pressure greater than 8 atm would be necessary to avoid convection-limitations. If the channel were 10 times thicker ($h=10\mu m$), this critical pressure would drop to 0.008 atm and the effect would completely disappear. Convection-limitations in surface transport are therefore a typical characteristic of sensors with characteristic heights in the single micron range and smaller.

Chapter 4. Dynamic Response of a Resonating Hollow Cantilever

Chapter Abstract

In this chapter, we analyze the dynamic behavior of a resonating hollow cantilever to relate the frequency response to the mass change inside the device. Two main cases are considered: uniform loading of the cantilever surface, and non uniform, or concentration-dependent loading of the surface. While the theory for the former is common place – and thus summarized briefly, the latter needs some further development. Developing a model for frequency response for non-uniform loads is essential to correlate the signal to the predictions made earlier by the transport models. The output signal is modeled and expressed as a surface concentration so that it can be linked directly to the results derived in chapter 2. Finally, experimental design and material conditions are used to calculate the cantilever's response as precisely as possible. The model takes into account the "hollowness" of the resonator (non uniform material properties) and its specific geometry.

4.1. Introduction

Among the techniques available to detect minute mass adsorbing to a surface, resonating cantilevers possess several operating qualities which distinguish them from other existing technologies such as surface plasmon resonance sensors (SPR) or quartz crystal microbalances (QCM). Their conventional microfabrication and small sizes enables them to be integrated as a component in more complex lab-on-a-chip applications. Cantilever sensors can also be built in parallel to allow multiple simultaneous sensing experiments with either independent or differential readout[*115*]. While some systems rely on a laser beam to monitor cantilever deflection, they can also be build optics-free[*65*] for easier integration on chip than surface plasmon resonance (SPR) sensors, for example. Most importantly, mass detection in a resonating device is performed in a label-free fashion, which is often a more practical alternative to the fluorescence sandwich immunoassays[*48*].

Resonating cantilever sensors also face challenges to overcome. The main one has to do with the decrease of the resonance quality factor Q by viscous damping of the cantilever movement when immersed in a liquid. Consequently, cantilever sensors have typically been used under atmospheric pressure or less to detect airborne contaminants such as mercury[*116*] or volatile organic compounds[*117*]. Similarly to QCMs, these sensors are extremely sensitive to small hydrostatic pressure changes in the measuring environment due to the dependence of the resonance frequency on the effective load at the surface of the resonating device[*118*]. The response of resonating cantilevers are also sensitive to small temperature changes and thus susceptible to drift[*119*].

4.1.1. Resonating Hollow Cantilevers

In an attempt to palliate to the common problems of cantilever sensing, Burg et al. [*108*] have recently worked to the development of a suspended microresonator sensor (SMS) composed of a thin resonating cantilever with a micron-thick fluidic channel running inside it such that the mass adsorption occurs within the device and not at its surface (Fig. 4.1). This innovation removes the need to operate in an aqueous buffer where pressure, temperature and viscous forces decrease the signal quality of the cantilever. The device can now be operated in vacuum, the optimal medium to provide the highest signal to noise ratio (highest quality factor Q), while still performing the same fluidic assays within the device. An additional feature of such detectors is that they become sensitive to the density of solutions flowing through them since the output signal is proportional to the total mass of the cantilver (composed of both device structure and fluidic channel solution). This characteristic enables the sensor to detect, for example, protein concentration in a given solution without them interacting with the sensor surface. However, when interactions occur at the cantilever wall, the very large surface to volume ratio of hollow cantilevers imply that most of the analyte mass present in the cantilever at equilibrium will be bound at the surface. This behavior can be explained by the high relative number of binding sites at the surface compared to the total number of analytes present in the channel at any time. The surface capacity parameter $\varepsilon=C_0h/C_{s0}$, characterizing the adsorption process as described in section 2.2.2 and Table 2.2, is then much smaller than unity.

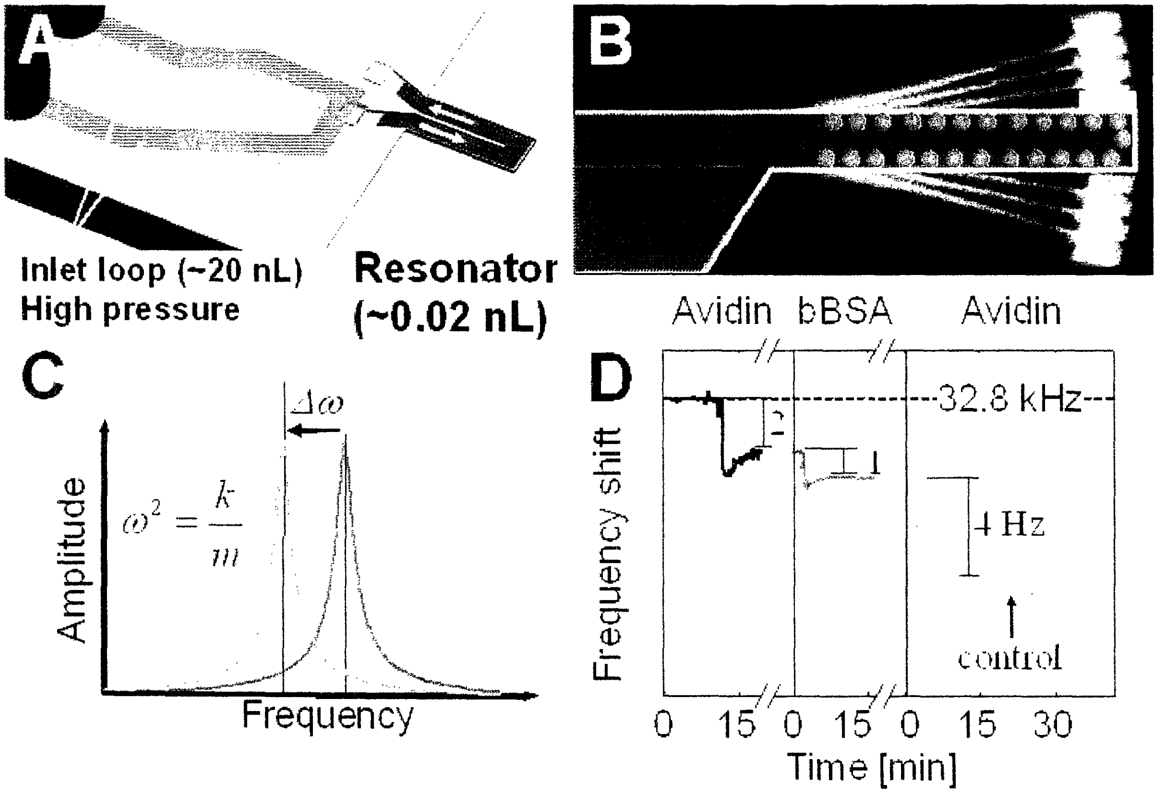

Figure 4.1: Schematics of the functioning of a suspended microresonator sensor. A) Schematics of the U-shaped fluidic channel running through the cantilever from a larger inlet bypass loop to the outlet. The flow is pressure driven. B) Illustration of the devices resonance. The displacement amplitude (~1 μm) is kept much smaller than the overall cantilever length (315μm). Biomolecular adsorption (illustrated in red), occurs at the device's interior fluidic walls. C) The added mass from the adsorbed molecules lowers the resonance frequency of the device by a few Hertz, which can be detected due to the narrow resonance peak of the device operated under vacuum. D) Sample experiment performed by successively adsorbing streptavidin (SA) and biotinylated bovine serum albumin (bBSA)

and measuring the frequency shift at equilibrium. The initial resonance frequency of the device was measured to be ~33 kHz and the shift up to 4 Hz (0.01% mass change). (This figure is a courtesy of T.P. Burg).

The resonating hollow cantilever (or SMS) solves many of the problems of current resonators using the outside surface for sensing. However, the use of micron-size fluidic channels will make the device susceptible to convective mass transfer limitations (section 2.4.1). Practically, these transport limits imply that the mass distribution inside the device may not be uniform at all times and that transport occurs from the "inlet to the outlet" as well as from the "bulk to the surface". Understanding how these transport limitations affect the resonator's output signal requires analysis.

In this chapter, we develop the mathematical model necessary to couple mass transfer analysis in microfluidic channels with the structural analysis of the SMS in order to predict the device's output frequency signal in transient binding assays. The models allow us to predict which operating conditions will be favorable to kinetics rate constants measurements. The results are then used to predict the shape of the output signal of common surface immunoassays. The analytic model provided is general and can be used to interpret signals in any form of resonating devices, including surface-based cantilever sensors and QCMs, operating in a regime with spatially and temporally varying mass deposition on the sensor.

4.2. Cantilever Bending Under Static Load

Prior to tackling the dynamic problem, defining and solving the equations for the static bending of a beam (Fig. 4.2) provides useful information on the system, such as the bending amplitude and the lever's spring constant, as well as laying the groundwork for the more complex analysis to follow. Reference for this section can be found in the classic book by Timoshenko[*120*] and the concise treatment by Sarid[*121*].

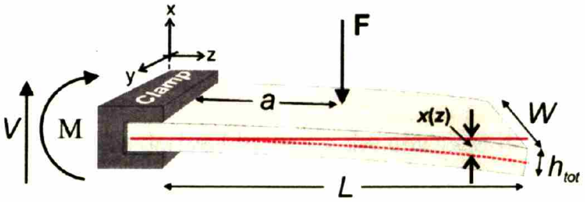

Figure 4.2: Force diagram and beam bending schematic under point load F applied at a distance a from the cantilever base. The clamping boundary condition imposes a zero shear force V and moment M at the tip of the cantilever and a zero velocity and displacement at the base.

The classical expression for the static bending of a beam is found by equating the beam's elastic resistance with the applied moment at any point along the beam axis.

$$\frac{\partial^2 x}{\partial z^2} = \frac{\mathrm{M}(z)}{EI}, \tag{4. 1}$$

$\mathrm{M}(z)$ is the moment distribution along the axis. E is the young's modulus and I the area moment of inertia. For a beam of rectangular cross section of area A its value is

$$I = \int_A x^2 dA = \frac{wh_{tot}^3}{12}. \tag{4.2}$$

Thus, the area moment of inertia, and therefore the beam bending stiffness, varies linearly with the cantilever width w and cubically with the beam's total thickness h_{tot}.

Under the influence of a concentrated load F, the moment function becomes $\mathrm{M}(z) = F \cdot (z - a)$. The way the beam is supported is also important in the definition of the boundary conditions. A rigid support at the origin of the beam yields the boundary conditions

$$x(z=0) = 0, \tag{4.3}$$

$$\left.\frac{\partial x(z)}{\partial z}\right|_{z=0} = 0. \tag{4.4}$$

This information is sufficient to solve for the bending of a beam under static load. Integrating eq. (4. 1) twice under the current boundary conditions gives

$$x(z) = \frac{Fz^2}{6EI}(z - 3a). \tag{4.5}$$

A cantilever spring constant can be derived by using the classical definition

$$k = \left|\frac{F}{x}\right|_{z=a}, \tag{4.6}$$

such that

$$k = \frac{3EI}{a^3}, \tag{4.7}$$

valid for small deflections of the cantilever. We note that the effective spring constant of the cantilever will vary strongly with the position at which the force is applied, and is minimal at *a=L*, the total length of the cantilever.

4.3. Dynamic Response of a Cantilever Beam

This section provides a summary of the steps required to achieve understanding of the results required to interpret the resonator signal. For a more thorough discussion, the reader is referred to the original development made in Sarid[*121*]. To derive results for the vibrating lever, the static solution needs to be extended using Newton's second law to account for the time varying term and balance the shear force along the lever axis. The shear force (*V*) balance over an infinitesimal axial unit length is

$$dV(z,t) = \frac{\partial^2 \mathrm{M}(z,t)}{\partial z^2} dz = -\underbrace{\rho A dz}_{mass} \frac{\partial x(z,t)}{\partial t^2}, \tag{4.8}$$

Substituting the moment's second derivative in the static load differential equation, eq. (4. **1**), yields

$$EI\frac{\partial^4 x(z,t)}{\partial z^4}+\rho A\frac{\partial^2 x(z,t)}{\partial t^2}=0. \tag{4.9}$$

By Laplace transform, the frequency response of the cantilever can be studied properly. The corresponding frequency domain equation becomes

$$EI\frac{\partial^4 x(z,j\omega)}{\partial z^4}+\rho A\omega^2 x(z,j\omega)=0. \tag{4.10}$$

Rewriting the equation in terms of spatial frequency gives

$$\frac{\partial^4 x(z,j\omega)}{\partial z^4}+\kappa^4 x(z)=0, \tag{4.11}$$

where the spatial frequency is found to be

$$\kappa=\left(\frac{\rho A}{EI}\omega^2\right)^{1/4}. \tag{4.12}$$

For convenience, the solution to the frequency response equation, eq. (4.11), can be expressed by the following set of basis functions

$$\begin{aligned} x(z) &= c_1\{\cos(\kappa z)+\cosh(\kappa z)\}+c_2\{\cos(\kappa z)-\cosh(\kappa z)\} \\ &\quad + c_3\{\sin(\kappa z)+\sinh(\kappa z)\}+c_4\{\sin(\kappa z)-\sinh(\kappa z)\}. \end{aligned} \tag{4.13}$$

From the static bending boundary conditions, eqs. (4.3) and (4.4), yields $c_1=c_3=0$. The boundary conditions on the moment and shear force at the edge of the cantilever are provided by another pair of boundary conditions necessary to solve the 4th order differential equation.

$$\mathrm{M}(z=L)=EI\left.\frac{\partial^2 x(z)}{\partial z^2}\right|_{z=L}, \tag{4.14}$$

$$V(z=L)=\left.\frac{\partial \mathrm{M}(z)}{\partial z}\right|_{z=L}=EI\left.\frac{\partial^3 x(z)}{\partial z^3}\right|_{z=L}=0. \tag{4.15}$$

They provide the remaining constant ratio

$$\frac{c_4}{c_2} = -\frac{\cos(\kappa L)+\cosh(\kappa L)}{\sin(\kappa L)+\sinh(\kappa L)} = \frac{\sin(\kappa L)-\sinh(\kappa L)}{\cos(\kappa L)+\cosh(\kappa L)}, \tag{4.16}$$

and, by reducing the equation above, the eigenvalue equation

$$\cos\kappa L \cosh\kappa L + 1 = 0\,. \tag{4.17}$$

The first two eigenvalues are found to be $\kappa_1 L$ =1.875 and $\kappa_2 L$ =4.694. The first two values of the constant ratio gives $(c_4/c_2)_1$=-0.7341, $(c_4/c_2)_2$= -1.0185. Higher modes are not necessary here but can be found, along with more details in the development in the book by Sarid[*121*]. Finally, the normal eigenmodes for the vibration of the lever can be obtained using the values of κ_n and $(c_4/c_2)_n$:

$$x_n(z) = \frac{x_0}{2}\left[\left\{\cosh(\kappa_n \frac{z}{L}) - \cos(\kappa_n \frac{z}{L})\right\} + \left.\frac{c_2}{c_4}\right|_n \left\{\sinh(\kappa z) - \sin(\kappa z)\right\}\right]\cos(\omega_n t)\,. \tag{4.18}$$

The first resonance frequency can therefore be computed from the spatial frequency expression in eq. (4.12)

$$\omega_1^2 = \frac{EI}{\rho A}\kappa^4 = \frac{(1.875)^4 EI}{\rho A L^4}\,. \tag{4.19}$$

Using the expression of the spring constant provided in (4.12) and the cantilever mass $M_c = \rho AL$, the first resonance frequency can alternatively be expressed as

$$\omega_1 = \sqrt{\frac{(1.875)^4}{3\rho AL}\cdot\frac{3EI}{L^3}} = \sqrt{\frac{k}{0.24 M_c}}\,. \tag{4.20}$$

The same approach is adapted here to obtain the value of the resonance frequency under the influence of a dynamic load concentrated at a point a on the lever. In this situation, the equations of motion are exactly the ones of the harmonic oscillator and the known resonance frequency is given by

$$\omega = \sqrt{\frac{k}{m_p}}, \tag{4.21}$$

where m_p is the point mass added at the tip of the cantilever and k is the spring constant. As a result, we can infer the natural resonance frequency of a cantilever of mass M_c is the same as the one of a massless cantilever with a point load at the tip 0.24 times smaller.

Furthermore, by using the principle of superposition, stipulating that the shear force at the tip of the device will be the sum of the contribution of both uniformly distributed and point masses at the tip, the final resonance frequency can be expressed as a function of an effective mass M_{eff}:

$$\omega = \sqrt{\frac{k}{M_{eff}}} = \sqrt{\frac{k}{m_p + 0.24(M_c + m_d)}}. \tag{4.22}$$

The capital letter M represents the largest part of the mass (the cantilever mass), while the lower case represents the tiny increment arising from mass deposited either at the tip (m_p) or uniformly distributed at the surface (m_d). Thus, for a small mass change around the cantilever mass M_c the relative frequency change can be expressed using a Taylor series truncated to the first order

$$\omega \approx \sqrt{\frac{k}{0.24M_c}}\left[1 - \frac{1}{2M_c}\left(\frac{m_p}{0.24} + m_d\right)\right]. \tag{4.23}$$

The change in resonance frequency peak caused by a small addition of mass is given by the second term of the expansion. Rearranged, it is expressed under the form

$$\frac{\Delta f}{f_0} \approx -\frac{1}{2M_c}\left(\frac{m_p}{0.24} + m_d\right), \tag{4.24}$$

where the natural resonance frequency is

$$f_0 = \frac{1}{2\pi}\sqrt{\frac{k}{0.24M_c}}. \tag{4.25}$$

The previous results are the ones usually used to characterize the resonance frequency of a microcantilever[*68*, *122*]. In the following section, we will expand them and generalized them for the case of neither uniform nor point mass loads.

4.4. Vibrating Cantilever Response Under Arbitrary Load

4.4.1. Non-Uniform Loads Occurrence in Resonators

In an ideal reaction inside a cantilever, where the transport to the surface is either purely diffusion-limited or purely reaction-limited, one should expect a uniform analyte deposition all over the cantilever surface. However, in many instances, the operation regime falls in neither categories and the concentration profile inside the device is not flat, yielding, before equilibrium is reached, to a non uniform analyte deposition at the surface. We are thus in the presence of a non uniform mass distribution at the surface and the models presented earlier (uniform and point loads) fail to express the signal as a function of mass for these more complex cases. A new model must therefore be developed to interpret the resonator's data and express the arbitrary mass distribution in the form of an effective uniform mass to link it to the existing models (Fig. 4.3). In earlier theoretical work on resonating cantilevers, the devices were usually exposed to a reagent in gaseous form or in a liquid volume much greater than the cantilever size. Thus, no convection limitations existed and deposition occurred uniformly. As a result, there was no need to explore frequency output for non uniform mass deposition up to now.

Physical insights can be gained by making an analogy between a vibrating cantilever and a swinging door held by its hinges. If one is to swing the door from its handle back and forth, the amount of energy required to do so will vary not only with the door mass, but also with the mass distribution with respect to the distance from the hinges. Any mass added close to the hinges would be expected to have little effect on the amount of energy required to swing the door open while mass added right above the handle would have a much greater effect due to the increased force moment resulting. The greater the system's moment of inertia, the lower the natural resonance frequency will be.

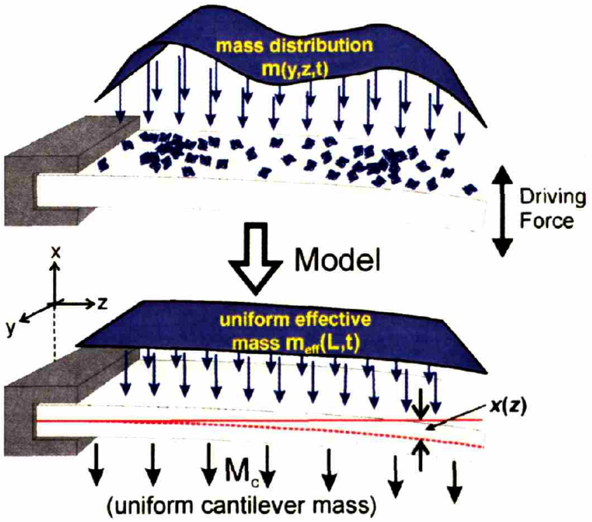

Figure 4.3: Schematics of the approach to modeling dynamic properties of resonant cantilevers under non-uniform loads. Through the balance between potential and kinetic energy at every point of the device (Rayleigh method), we convert the non-uniform mass distribution in a uniform effective mass compatible with the existing theory.

4.4.2. The Rayleigh Approach to Eigenfrequency Analysis

Finding the perturbation solution to eq. (4.9) to include the effect of a small mass, which is neither punctual nor uniform, deposited on the cantilever surface is hard to perform. To obtain this result, we proceed instead using an approach analogous to the Rayleigh solution to a vibrating beam. The method consists in balancing the stored strain energy and the kinetic energy of the moving lever. It is known to yield an expression for the resonance frequency within 1% of the frequency found by solving the full biharmonic differential equation described in eq. (4.9). Furthermore, when the deposited mass is much smaller than the overall mass of the cantilever, the energy method can be used as a perturbation of the full solution described earlier, thus making it even more accurate overall.

The potential energy stored in a cantilever is elastically stored in the form of deformation or strain energy. To compute the strain energy term, we first need to map the deflection of a beam actuated by a periodic driving force. It is well known that whether the force acts at the tip of the cantilever (point load) or uniformly on its surface (distributed load), the resulting static deflection will be different. However, when operated at its resonance frequency, all contribution to the bending from the unexcited modes vanishes in comparison to the excitation mode. This assertion is true provided that we have a high resonance quality factor *Q*. For SMS devices, *Q* factors are approximately of 700[*123*], and the non resonant modes can be ignored. Consequently, the resonance profile of the oscillating cantilever becomes independent of the actuation point of the driving force, be it concentrated at the tip, uniformly distributed or anywhere in between.

Strain-Kinetic Energy Balance Method

The stored elastic energy in a bent lever is defined by

$$\Omega_s \equiv \frac{EI}{2}\int_0^L \left[\frac{\partial^2 x(z,t)}{\partial z^2}\right]^2 dz\,. \tag{4.26}$$

In a first approximation, the addition of a small amount of mass inside the cantilever does not increase the strain energy contained in the cantilever since Ω_s does not depend on mass but only on geometry. Substituting *x*(*z*) by its value from eq. (4.18) yields after performing the integration:

$$\Omega_{s,\max} = 1.545\frac{EI}{L^3}x_0^2\,. \tag{4.27}$$

The maximum strain occurs when the cosine term in eq. (4.18) becomes equal to 1.

As for the kinetic energy, it can be expressed in the frequency domain using Rayleigh's theorem as

$$\Omega_k \equiv \int_0^L \frac{dm}{dz}\left[\frac{\partial x(z,t)}{dt}\right]^2 dz . \tag{4.28}$$

The maximum kinetic energy for a given mode is thus

$$\Omega_{k,\max} = \frac{\omega^2}{2}\int_0^L \frac{dm}{dz} x(z,0)^2 dz . \tag{4.29}$$

The amount of cantilever mass per unit length does depend both on the cantilever mass and on the amount and location of deposited mass inside the cantilever, such that

$$\frac{dm}{dz} = \rho A + \beta(z) . \tag{4.30}$$

The function $\beta(z)$, in mass per unit length, represents the linear mass distribution along the cantilever's bending axis. Using the expression of $x(z)$ found in eq.(4.18), the lever's maximum kinetic energy can be obtained for a general mass distribution $\beta(z)$

$$\Omega_k = \left(\frac{M_c}{8} + \frac{1}{2x_0^2}\int_0^L \beta(z)x(z)^2 dz\right)\cdot x_0^2\omega^2 , \tag{4.31}$$

where $M_c = \rho AL$ is the lever's total mass.

Assuming conservation of energy and mass in the system, the resonance frequency of the system is found by equating the maximum strain energy with the maximum kinetic energy stored in the lever.

$$\omega = \sqrt{\frac{k}{0.24M_c + \frac{0.97}{x_0^2}\int_0^L \beta(z)x(z)^2 dz}} . \tag{4.32}$$

The validity of this generalized expression for arbitrary small load on a cantilever can be verified by computing two limiting cases:

i) Uniform cantilever loading

The mass distribution can be expressed as , $\beta(z)=m_d$. Using eq. (4.32), the integration yields

$$\omega=\sqrt{\frac{k}{0.24(M_c+m_d)}}, \tag{4.33}$$

a result analogous to the one found in eq. (3. 2). The distributed mass m_d simply adds up to the mass of the cantilever and decreases the resonance frequency accordingly.

ii) Point mass loading at $z = a$

Using the general expression for loading, a point mass can be modeled using a Dirac delta function, $\beta(z)=m_p\delta(z-a)$. Using the sifting property of the delta function eq. (4.34) reduces to

$$\omega=\sqrt{\frac{k}{0.24M_c+0.97\dfrac{m_p\cdot x(a)^2}{x_0^2}}}. \tag{4.34}$$

Physically, this dependence on $x(a)^2$ implies a non-linear relationship between the frequency change and the position of the added mass along the cantilever (roughly $d\omega \sim z^2$). When the mass is added at the tip, then expression (4.34) reduces to the one deduced using classical mechanics principles, eq. (4.22), with an error of 3%. Therefore, the energy method, while most accurate in computing the frequency change in uniform loads, introduces an error of approximately 3% for point loads. Since no load can be further away from uniformity than a point load (we remember that the Fourier transform of a Dirac delta function is a constant function), this error constitutes an upper bound on the model's error. In most physically meaningful adsorption experiments, deposition does not occur punctually and the measurement error remains below the 3% maximum.

4.5. Coupling Mass Adsorption and Surface Transport

Assessing surface adsorption using frequency signal can be difficult in non-ideal cases. A frequency shift output signal lumps together important information about the spatial distribution of analytes adsorbed at the device's surfaces. One can easily imagine many different mass distributions on the cantilever that would lead to the same output frequency signal. Therefore, a loss of information occurs in this lumping process. While it is not possible to retrieve this lost information, a thorough understanding of the transport regimes will give us clues on the shape of the distribution inside the cantilever and allow us to study binding kinetics and transport behaviors.

Chapters 2 and 3 have been dedicated to study the nature of protein transport in micron-scale channels. One key result is to obtain a monolayer surface concentration of adsorbed species, $C_s(y,z,t)/C_{s0}$ or $\Theta_s(y,z,t)$ in dimensionless form, as a function of the device operation parameters, such as the flow velocity U, the analyte distribution in the fluid $\Theta_b(y,z,t)$, and the reaction kinetics. Once this surface concentration is calculated, it can be converted it to a linear mass distribution $\beta(z,t)$ in a resonant cantilever sensor using the relative density change $\Delta\rho=\rho_a-\rho_{water}$ between the bound analyte and the displaced water molecules:

$$\beta(z,t) = \int_0^W \frac{n_w M_a \Delta\rho C_{s0}}{\rho_a} \left[\Theta_s(y,z,t) + \varepsilon \cdot \Theta_b(y,z,t)\right] dy. \tag{4.35}$$

The channel width W is part of the equation to reduce the surface concentration to a linear function, and the molecular weight M_a of the analyte is introduced to convert the molar units to mass. The number of walls reacting n_w indicates that twice the mass can be stored inside the cantilever is both walls can adsorb analytes. In shallow microfluidic channels, the relative surface capacity $\varepsilon = C_0 h / C_{s0}$ is often much smaller than one, which implies that the bulk concentration term in eq. (4.35) can often be neglected.

A taylor expansion of eq. (4.32) introducing the new time dependent mass distribution $\beta(z,t)$ yields the generalized expression for the sensor frequency shift under arbitrary time-dependent loads:

$$\frac{\Delta f}{f_0} = -\frac{1}{2}\gamma \cdot \left[\frac{4}{x_0^2 S} \iint_S \left[\Theta_s(y,z,t) + \varepsilon \cdot \Theta_b(y,z,t) \right] x(z)^2 dS \right]. \tag{4.36}$$

The dimensionless sensitivity parameter γ reads

$$\gamma = \frac{n_w M_a \Delta\rho C_{s0} S}{\rho_a M_c}, \tag{4.37}$$

where S is the surface area of the channel inside the cantilever.

4.6. Predicted Experimental Results

The frequency signal in the microresonator will depend mainly on three factors: the density of binding sites, the mass distribution at the surface, and the shape of the resonator itself. The density of sites, if uniform, will only affect the amplitude of the signal, whereas the latter two factors will also affect the shape of the frequency curves, thus convoluting the actual association and dissociation kinetics at the surface. Since in SMS devices the relative surface capacity for adsorption in on the order of $\varepsilon \sim 0.001$, we neglect the contribution of the unbound analytes in the following analysis.

In this section, we consider various special mass distribution cases for which a simple solution exists. The cantilever geometry is always assumed to be the same (see Fig. 4.5): a channel taking a round trip from the cantilever base to the tip and back, where the turning section is short enough that the transversal flow can be neglected. The natural frequency of the suspended microresonator sensor, using the geometry described in Fig. 4.4 and the relevant material properties, is found to be 34 kHz. Details of the calculation and material properties are provided in appendix A4. Experimental measurements of the resonance frequency were consistently in the range of 32-35 kHz depending on where on the original wafer the device comes from[*123*]. The discrepancy between the predicted and measured resonance frequency is likely to come from fluctuations in the material properties. The Young's modulus of silicon nitride used fluctuates depending on the deposition method[*124*] and the actual value for this application has not been directly measured. Not taking into account the "hollowness of the cantilever" would underestimate the resonance frequency by 10%.

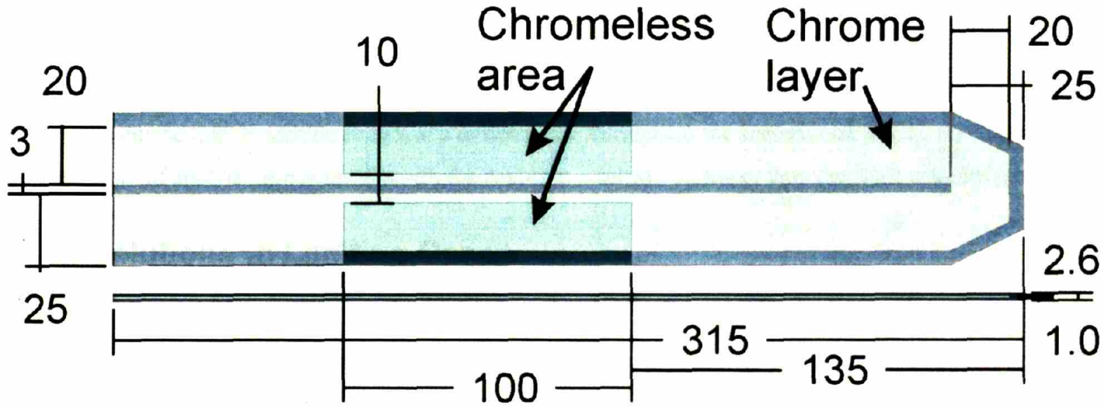

Figure 4.4: Scaled drawing of the resonant microcantilever studied. The device consists of a U-shaped fluidic channel going through a silicon nitride structure. A 40 nm-thick chrome layer was deposited onto the cantilever to allow position measurement using laser reflection. Dimensions are in microns.

In a first approximation, the fluid is assumed to always be moving along the cantilever axis. In a U-shaped fluidic channel, the displacement-averaged surface integral then becomes

$$\frac{4}{S}\iint_S \Theta_s(y,z,t)x(z)^2\,dS = \frac{2}{L}\left[\int_0^L \Theta_s(z,t)x(z)^2\,dz + \int_L^{2L} \Theta_s(z,t)x(2L-z)^2\,dz\right]. \tag{4.38}$$

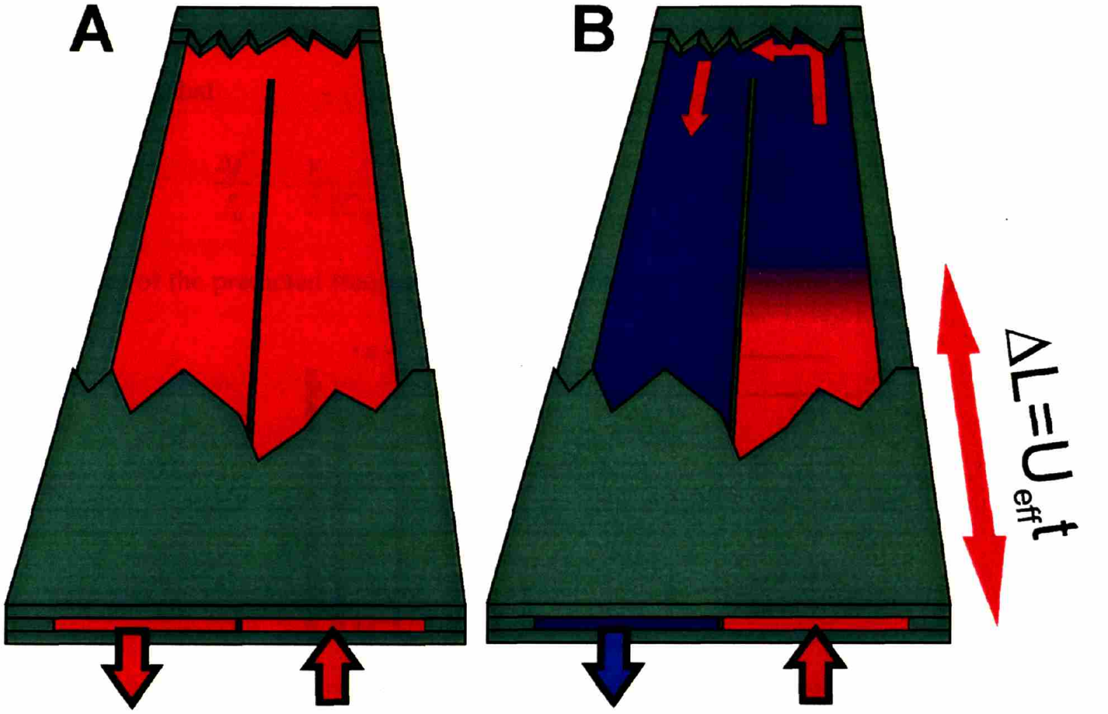

Figure 4.5: Illustration of the two limiting cases studied. A) Reaction-limited case. The transport is fast enough through the device that deposition occurs at a uniform rate throughout the surface (see 4.6.1). B) Convection-limited case: the front of analyte propagates through the device at a speed U_{eff}, lower than the fluid velocity (see 4.6.2).

4.6.1. Solutions to Limiting Cases

4.6.2.1. Limiting case 1: Uniform deposition

The mass distribution can be uniform because of deposition conditions (e.g. fully reaction-limited regime) or because the system has reached equilibrium. The concentration becomes independent of space and $C_s(x,y,t) \to C_s(t)$ (Fig. 4.5A). The frequency response curve simplifies to

$$\frac{\Delta f}{f_0} = -\frac{1}{2}\gamma \cdot \Theta_s(t). \tag{4.39}$$

The case of uniformly deposited mass leads to the result quoted in various experimental papers[*68, 116, 117*] is recovered. Assuming that the reaction kinetics is slow enough that there is no significant depletion anywhere in the bulk, mass deposition will follow a pseudo first order kinetics such that

$$\frac{\Delta f}{f_0} = -\frac{\gamma}{2}\frac{C_0}{(C_0+K_D)}\cdot\left(1-\exp\left\{-(k_{on}C_0+k_{off})t\right\}\right). \tag{4.40}$$

The shape of the predicted frequency curve under these conditions is provided in Fig. 4.6.

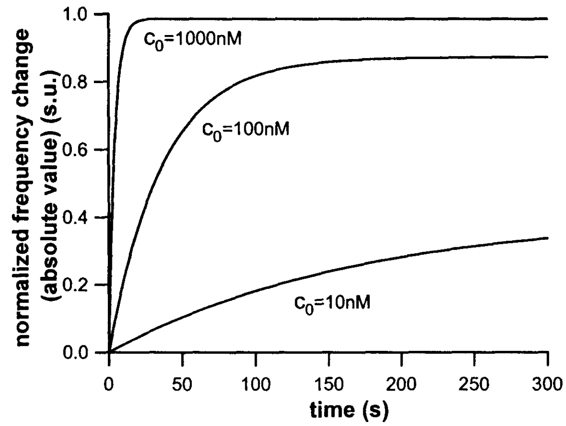

Figure 4.6: Analytic Solution providing the normalized output signal ($-2/\gamma\cdot\Delta f/f_0$) under fully reaction-limited conditions for various initial concentrations of analytes. The normalized signal gives directly the bimolecular kinetic association curve. The same is true for dissociation curves. This situation is ideal for measuring kinetics in sensors.

4.6.2.2 Limiting Case 2: Wave-like propagation

The surface saturates with a wave front of equilibrium concentration C_{s-eq} propagating at velocity U_{eff} (see section 2.4.2 and Fig. 4.5B). Assuming that the part of the front in transition to reach equilibrium is small compared to the size of the channel ($\sigma \ll L_{channel}=2L_{cantilever}$, section 2.4.3), the surface concentration as a function of time can be expressed as

$$C_s(z,t) = C_{s-eq}\cdot\left(1-H\left(z-U_{eff}t\right)\right),\quad 0<t<2L/U_{eff}, \tag{4.41}$$

where H is the Heaviside unit step function and the equilibrium concentration is $C_{s\text{-}eq}=C_0/(C_0+K_D)$ for bimolecular reactions.

When $t < L/U_{eff}$, the first side half of the device is filled while the other side remains clear. At higher times, the second half of the channel is filled from the tip to the base. Since the device length L is much larger than the device width W ($L > 5 \cdot W$), the transversal modes are assumed to be too far away from the normal resonance frequency of the cantilever and dampened away.

Using the expression for the displacement-averaged surface integral found in eq. (4.38), the full frequency signal becomes, in integral form

$$\frac{\Delta f}{f_0} = \begin{matrix} -\dfrac{\Delta f_{\max}}{f_0} \times \dfrac{2}{x_0^2 L} \displaystyle\int_0^{U_{eff}t} x(z)^2 \, dz, & 0 < z < L \\ -\dfrac{\Delta f_{\max}}{f_0} \times \left(\dfrac{1}{2} + \dfrac{2}{x_0^2 L} \displaystyle\int_L^{U_{eff}t} x(2L - z)^2 \, dz \right), & L < z < 2L \end{matrix} \tag{4.42}$$

At any time for a given reaction, the maximum frequency change is expressed through the sensitivity parameter γ as

$$\frac{\Delta f_{\max}}{f_0} = \frac{1}{2} \gamma \left(\frac{C_0}{C_0 + K_D} \right) \tag{4.43}$$

The integral of $x(z)^2$ required in eq.(4.42) is easily computed using a mathematical software such as Maple$^{\text{TM}}$. However, the many terms involved make it too large for convenient display and we choose not to include it.

Intuitively, the signal from such a contribution would have its maximum rate of change at the tip of the device since this is where the signal is maximum per mass increment. This behavior is readily noticed in Fig. 4.7. Taking the derivative of the normalized frequency signal when the wave front reaches the tip ($t = L/U_{eff}$) gives an expected slope of

$$\left. \frac{\partial}{\partial t} \left(\frac{\Delta f}{f_0} \right) \right|_{t = L/U_{eff}} = -\gamma \cdot \frac{C_0}{C_0 + K_d} \cdot \frac{U_{eff}}{L} = -2 \frac{\Delta f_{\max}}{f_0} \frac{U_{eff}}{L}. \tag{4.44}$$

The maximum slope at the inflection point in the curve is thus linearly proportional to the wave front's effective velocity. Since $U_{eff}(C_{s0},C_0,K_d)$ is a function of the surface and bulk concentration and of the equilibrium dissociation constant (eq. (2.30)), any of these values can be extracted from the slope if the two others are known. Experimentally, C_{s0} is easy to measure as it corresponds to the frequency change as the binding of the probe layer occurs. C_0 can also be controlled experimentally in a way that K_D remains the only unknown to be calculated from the slope.

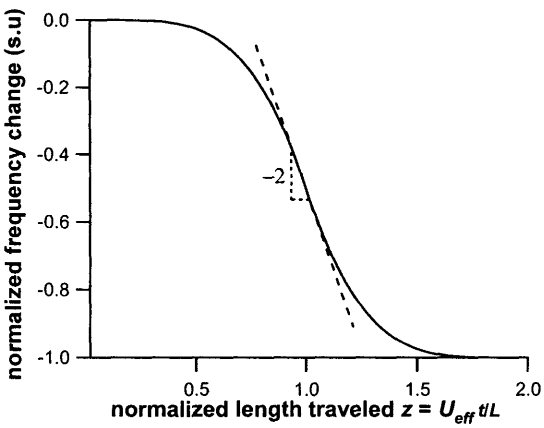

Figure 4.7: Analytic solution providing the normalized frequency change ($\Delta f/\Delta f_{max}$) as a function of the normalized distance traveled by the wave front . When $U_{eff}t/L=1$, the wave front reaches the tip of the cantilever and the sensitivity is maximal. The general slope at $U_{eff}t/L=1$ is -2 .

4.6.3. Kinetics Measurement in Partially Convection-Limited Conditions

4.6.3.1. Identifying the Correct Regime With Dimensionless Numbers

Since the frequency output signal lumps together the mass distribution, the shape of the concentration distribution inside the device must be established by other means. To extract kinetics from the data, it is imperative that we operate in reaction-limited regime. In transport terms, the reaction time scale $\bar{t}_r$ inside the device has to be much slower than either convection

$\bar{t}_c$ or diffusion $\bar{t}_d$ time scales. The conditions on transport limitations can thus be summarized using dimensionless numbers in the following way:

$$Da_{\mathrm{I}} \equiv \frac{\bar{t}_c}{\bar{t}_r} << 1, \quad Da_{\mathrm{II}} \equiv \frac{\bar{t}_d}{\bar{t}_r} << 1. \quad . \tag{4.45}$$

As we have seen from earlier analysis, for a sensor with channel thicknesses in the single micron range, diffusion is always much faster and the delivery of analytes (convection) more frequently limits the response. The dominant condition is thus imposed by the first Damköhler number Da_{I} and reads, in terms of the device specifications:

$$L << \frac{h}{k_{on} C_{s0}} U. \quad . \tag{4.46}$$

To access kinetics, the length of the sensing region (i.e. the channel path inside the cantilever) must therefore be much smaller than the reaction time scale multiplied by the carrying fluid velocity *U*.

4.6.3.2. Numerical Simulations for Arbitrary Operating Conditions

When the condition given in eq. (4.44) is not met, i.e. $L \sim hU/k_{on}C_{s0}$, then none of the above limiting solutions can be applied. Instead, one must solve the full transport model as described in chapter 2, compute the value of the surface concentration $C_s(z,t)$ at all times and integrate it numerically over the channel path (using eq. (4.38)) to obtain the time-varying frequency output signal. These simulations have been performed in FEMLAB$^{\mathrm{TM}}$ according to a model described in appendix A3. The results obtained for typical antibody-antigen bimolecular kinetics under realistic operating conditions are displayed in Fig. 4.8-4.10.

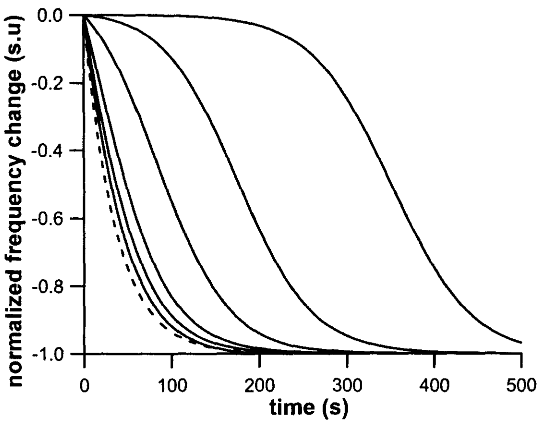

Figure 4.8: Simulated normalized output signal ($\Delta f/\Delta f_{max}$) for a typical immunoassay for various analyte flow velocities. The experimental parameters used are the following: k_{on}=2.4x10^5 M^{-1}s^{-1}, k_{off}=3.5x10^{-3}s^{-1} (Anti-Protein A33 immunoassay as reported by Catimel et al., 1998), $L_{cantilever}$=0.315mm, h=1μm, C_{s0}=10 fmol/mm^2, C_0=10^{-7}M and D=5.5e-5mm^2/s. Solid lines: Output signal for velocities U= 0.5, 1, 2, 5, 10, 20 mm/s (from left to right). Dashed line: Fully reaction-limited model. As the velocity increases, the signal loses its sigmoidal shape and tends asymptotically to the fully reaction-limited solution.

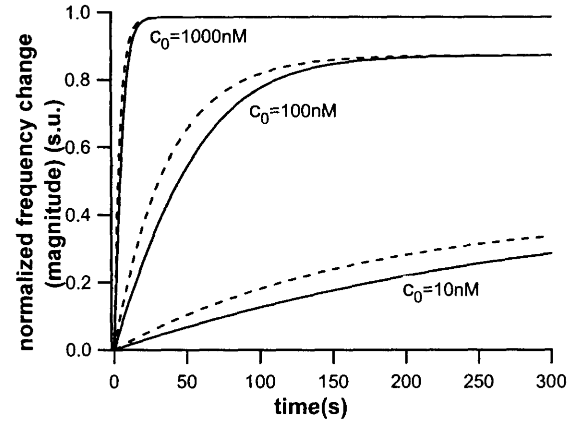

Figure 4.9: Simulated output signal ($-2/\gamma \cdot \Delta f/f_0$) for partially convection-limited transport situations. The experimental parameters used are the same as in Fig. 4.8 with the velocity fixed at U=10 mm/s and varying analyte concentrations in the bulk. Solid lines: FEMLAB simulations. Dahsed lines: Value predicted by a simple analytic model involving bimolecular kinetics (Fig. 4.6).

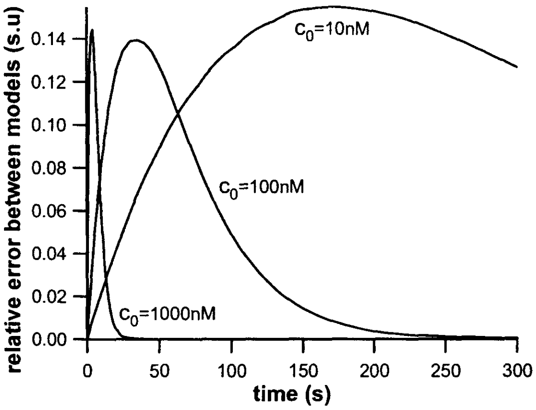

Figure 4.10: Relative error introduced by convection limitations ($\Delta f_{bimolecular}(t)$- $\Delta f_{FEMLAB}(t))/\Delta f(t \rightarrow \infty)$. The error on C_0=10nM is slightly higher due to the small relative increase in kinetics rate when $C_0 < K_D$ (here K_D=14nM) due to the contribution of k_{off} in the rate (for C_0=10nM, $k_{off} > k_{on}C_0$).

In these non-ideal cases, it is observed that the output signal behavior possesses both the characteristics of the uniform deposition and wave-like propagation limiting cases. In Fig. 4.8, when the flow velocity is maintained low (U>5 mm/s) under the proposed experimental conditions, the signal displays the sigmoid signature of convection-limitations. As the velocity is increased, and thus the convective transport limitations reduced, the signal loses its sigmoid tail and asymptotically approaches the shape of typical bimolecular kinetics association curves, such as the curves presented in Fig. 4.6 and 4.9. Fig. 4.10 displays the error introduced on the ideal kinetics data by convection-limitations. The magnitude of the error becomes constant when the bulk concentration $C_0 >> K_D$.

4.6.5. Model Approximation

Performing the surface integral with the full bending lever solution may not always be most useful to quickly predict a signal due to its algebraic complexity. A useful approximation is to assume that the lever only pivots at its hinges while its body remains rigid. For that case,

$$x(z) = x_0 \frac{z}{L}, \tag{4.47}$$

and the lever integral, eq. (4.38), simplifies to

$$\iint_S \Theta_s(y,z,t)x(z)^2 dS = \frac{Wx_0^2}{2L^2}\left[\int_0^L \Theta_s(z,t)z^2 dz + \int_L^{2L} \Theta_s(z,t)\cdot(2L-z)^2 dz\right]. \tag{4.48}$$

To approximate the effect of the mass deposited on the cantilever, it is therefore only required to know the distribution up to its second moment, where

$$\mathrm{M}_2 = \int_0^L \Theta_s(z,t)z^2 dz\,. \tag{4.49}$$

The second moment of a distribution is proportional to its variance, the first moment to its center of mass, and the zeroth moment to the total mass. Results are compared in Fig. 4.11.

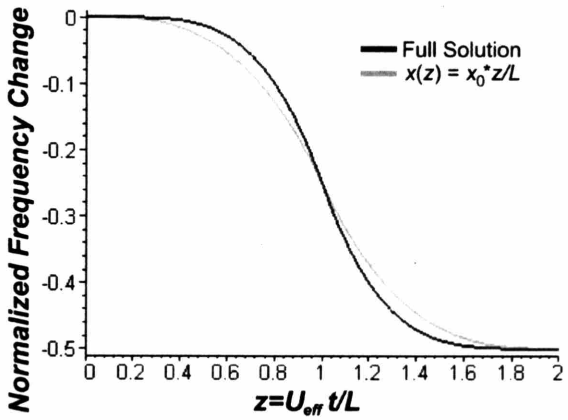

Figure 4.11: Expected frequency signal for a wave front traveling at a velocity U_{eff} across the sensor's length. In some cases, linearizing the cantilever displacement provides a sufficient approximation to interpret experimental results. In the linearized model, however, the maximum slope of the signal at mid height is somewhat milder than for the full solution, and represents ¾ of the maximum frequency shift instead of 1.

4.7. Conclusion

When studying binding assays with mass sensors, it is critical to measure the true reaction kinetics profile and not a combination of both mass transfer and reaction effects. In practice, however, it is extremely difficult to eliminate all mass transfer limitations since it would often require operating in conditions that the device cannot tolerate such as too high pressure, or too thin channels (thus risking clogging). To circumvent this problem, models accounting for the exact contribution of mass transfer limitations exist and can be used to subtract its effect on the kinetics output signal. To apply these models, such as the ones summarized in Chapter 2, to the output signal analysis in a resonating hollow cantilever, we generalized the existing method in several ways. First, we developed a model based on Rayleigh's energy balance to include the effects of mass transfer limitations on the mass distribution inside the device. Since, from an energy point of view, mass deposition has the same effect whether it occurs at the surface of the lever or inside it, the model provides a general tool to study any form of resonating cantilever under arbitrary load. Secondly, we used the aforementioned model to predict the output signal shape. We conclude that, even though it is often impossible to directly measure the mass distribution inside a cantilever, a sigmoidal output signal directly corresponds to convection-limited transport situation. By increasing the analyte flow velocity, it is possible to reduce these transport limitations and achieve reaction-limited regimes, where kinetics measurements are possible. Finally, we used experimental data to predict the output signal under various operating conditions and discussed their interpretation.

Chapter 5. Flow-Induced Deformation of Shallow Microfluidic Channels

Chapter abstract

In this chapter, we study the elastic deformation of polymer microchannels under imposed flow rates and its effect on the laminar flow profile and pressure distribution inside them. Deformation is observed to be important in low aspect ratio channels and to increase when the channel is made shallower. Imaging of the bulging channels under various flow conditions is performed by confocal microscopy. Results show that deformation is not uniform throughout the channel and that tapering occurs along the stream-wise axis. Finally, the measured pressure drop is monitored as a function of the imposed flow rate. For any given pressure drop, the corresponding flow rate in a deforming channel is found to be several times higher than expected in a non deforming channel. The experimental results are supported by scaling analysis and computational fluid-structure interaction models.

5.1. Introduction

Over the last 10 years, it has become clear in the microfluidics community that soft lithography techniques offer a valuable alternative to conventional lithography for a wide range of applications[*30*]. Poly(dimethylsiloxane) (PDMS) is often the material of choice as it is quick and simple to use, cheap, transparent, and biocompatible[*31*]. PDMS can be molded to yield features down to the nanometer scale, allowing the creation of nanochannels and structures[*65*], microcontact printing stamps[*42*], and other devices requiring fine geometric control.

Another property of soft lithography, which sets it apart from classical silicon or glass-based micromachining processes, is the high compliance of its materials. The bulk properties of PDMS are characterized by a low Young Modulus *E* (in the range of 0.5 to 4 MPa) and a high Poisson ratio (ν=0.5, incompressible), making it a typical rubber elastic material[*125*]. One-dimensional stress-strain analysis thus implies a structural deformation (strain) on the order of 10% under a pressure of 1 atm. By contrast, monocrystalline silicon Young's modulus, E=170 GPa, is several orders of magnitude above that of PDMS, and the material can withhold extremely high pressures without deforming[*124*].

The high deformability of soft lithographic materials has provided new venues to develop MEMS devices. Quake and others have demonstrated how PDMS can be used to design pressure-actuated valves and create a versatile fluidic control platform[*34, 35*]. Similarly, deformable "soft" MEMS have been used in micro flow cytometry[*126*], on-chip pumping and mixing[*36*] and pressure sensors[*127*].

On the other hand, the deformability of rubber elastic materials also limits the range of applications of soft lithography. The sagging and sticking of structures with very low aspect ratios (height/width) will impose constraints on how wide channels can be made[*128*] and structural analysis has been performed to further understand this phenomenon in the specific case of microcontact printing[*129*].

Similarly, for pressure-driven flows, low aspect ratio channels will have a tendency to bulge under the imposed pressure. The deformation of a microfluidic channel drastically affects the effective pressure drop inside it and the resulting flow profile due to the fourth power dependence on the cross section length scale of the hydraulic resistance[*90*]. Therefore, any microfluidics applications for which a precise knowledge of the flow profile, pressure, and channel geometry is necessary will be compromised if the actual channel deformation cannot be quantified and taken into account.

The effect of channel deformation becomes important in a number of common microfluidic applications for which flow conditions are not unusual. Shear-flow assays – e.g. shear-based cellular[*76, 130*] or protein[*131*] assays, where linear velocities are required to be on the order of 1 m/s- are an example of such a system where the actual flow profile needs to be accurately determined in order to compute the effective shear rate. Diffusion-limited mass transfer also depends on flow profile and channel thickness. For a pressure-driven flow with specified pressure drop, the Péclet number $Pe=Uh/D$ (ratio of convective to diffusive time scales) varies as h^3 in a Poiseuille flow profile (see Table 1). The increase in the channel's effective thickness thus increases Taylor dispersion and alters the ability of a system to resolve intrinsic surface kinetics such as in surface plasmon resonance (SPR) sensing technology[*71*]. In nanoliter-size SPR sensors[*73*], the increase in the hydraulic resistance of the device yields higher pressures for the same flow rate and induces potential channel deformation. Multiphase microfluidic systems for the study of fast chemical reaction kinetics or crystallization often rely on droplet-based flows through microchannels at high velocities (>0.1 m/s) [*132*]. Deformation can also affect fluorescence intensity signals, which depend on the absorption path length across the channel, and can bias measurements if not taken into account. To conclude, any effect in microfluidics sensitive to channel dimensions[*20*] will be affected by channel deformation when it occurs. Table 1 summarizes the scaling of the various effects mentioned above with respect to the channel cross sections.

Table 5.1: Cross section dependence of key quantities susceptible to channel deformation in low aspect ratio

microfluidic devices ($W >> h$) for both fixed pressure drop and fixed flow rate conditions.

Effect	**Variable**	**Fixed Δp**	**Fixed Q**
Fluid Velocity	U	$\sim h^{2}$	$\sim h^{-1}W^{-1}$
Shear Stress	τ	$\sim h$	$\sim h^{-2}W^{-1}$
Residence Time	t	$\sim h^{-2}$	$\sim hW$
Mass transfer entrance length	L_E	$\sim h^{4}$	$\sim hW^{-1}$
Taylor Dispersion	K	$\sim h^{6}$	$\sim W^{-2}$

Few papers have discussed the importance of bulk channel deformation in microfluidics. Holden et al. used the aforementioned fluorescence intensity change effect to experimentally quantify bulk PDMS deformation under high pressure drop (~1 atm) [*133*]. Hosokawa et al. have monitored pressure changes in microchannels using deformable PDMS gratings[*127*]. However, neither of these analyses provides a structural model to describe the magnitude of the channel bulging with respect to the imposed flow rate (or pressure) and channel geometry.

In this communication, we provide theoretical and experimental verification of the extent of PDMS deformation inside rectangular microchannels. Finite element analysis is used to model the expected deformation and to extract scaling arguments relating the expected deformation and the operating conditions. These scaling laws can later be used by experimentalists as design criteria to either avoid deformation or use it to one's advantage in future devices.

5.2. Fluid-Structure Coupling Theory

The key aspect of the model described in this section is the coupling of the Navier-Stokes flow solution to the structural deformation through the hydrodynamic pressure exerted at the liquid-solid interface (Fig. 1). The problem is first presented here in decoupled form and description of the coupling is provided afterwards.

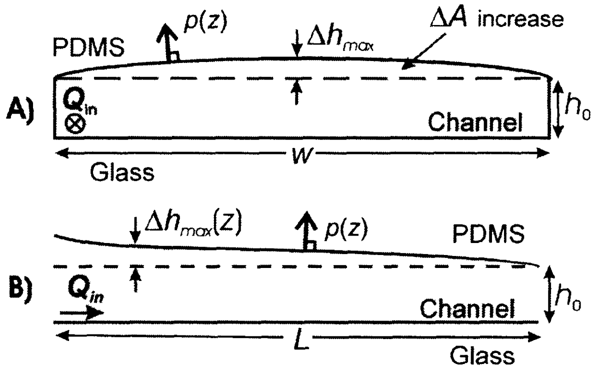

Figure 5.1: Schematic representation of polymer channel deformation under an imposed flow rate. A) Channel cross section normal to flow: Imposed pressure makes the cross-sectional area increase, thus deforming the flow profile inside the device and lowering the channel's hydraulic resistance. B) Channel cross section parallel to flow. The bulging of the channel becomes attenuated as the outlet is approached since the pressure decreases to ambient value. For a fixed flow rate, an acceleration of the fluid is expected along the length as a result of the decreasing cross-section area.

5.2.1. Hydrodynamics

Flow in most microfluidic devices is properly described by the Navier-Stokes equation:

$$\rho \bar{v}\bar{\nabla} \cdot \bar{v} + \mu \bar{\nabla}^2 \bar{v} = \bar{\nabla} p, \tag{5.1}$$

where v is the fluid velocity, p is the applied pressure and μ is the fluid viscosity (assumed to be that of water in this study: $\mu = 10^{-8}$ atm·s). In low aspect ratio rectangular channels with an imposed volumetric flow rate Q, eq. **(5.1)** can be solved and averaged over the cross section to yield a relationship between the flow rate and the pressure of the form[*90*]:

$$-\frac{\partial p(z)}{\partial z}=\frac{r_h}{A}\cdot Q, \tag{5.2}$$

where $p(z)$ is the pressure at stream-wise position z and A is the cross sectional area. The hydraulic resistivity r_h and the channel cross section will vary with the channel thickness h as

$$\frac{r_h}{A}=\frac{12\mu}{h^3W}. \tag{5.3}$$

The pressure drop in a channel under an imposed flow rate is thus dependent on the third power of the channel thickness indicating a strong sensitivity to channel deformation.

5.2.2. Structural Mechanics

At any cross section along the channel (z-direction), the pressure $p(z)$ will cause the channel to expand if we assume the surface to elastically deform according to its Young's modulus E. In this particular case, the glass slide is assumed rigid (E_{SiO2} = 62 GPa) and the channel perfectly sealed, thereby imposing a zero-displacement boundary condition along the rubber/glass interface. Inside the channel, the boundary condition is replaced by a fixed pressure on the deformable channel walls. In most applications, the thickness of the PDMS slab (several millimeters) is much higher than the extent of the channel deformation. Since beam bending theory only applies to slender beams (or membranes), it cannot be used here. The structural displacement of the PDMS is instead assumed to take place in a semi-infinite medium. The problem can be modeled using the constitutive stress-strain and strain-displacement coupled equations with proper boundary conditions accounting for fixed displacement at the edges and fixed pressure at the flow interface. Stress-strain analysis in semi-infinite media is common place in soil mechanics, where the pressure imposed by a large structure causes soil deformation around it (see for example Poulos[*134*]).

The mathematical formulation of this classical structural mechanics problem involves 15 coupled differential equations (6 stresses, 6 strains, 3 displacements) for which analytic solutions exist only in the cases of highest symmetry. For example, analytic solutions would exist if the displacement conditions were relaxed, i.e. the PDMS is not bound to the glass. This situation would lead to a variant of the Boussinesq contact problem: a semi-infinite elastic medium moving under a point force[*120*]. However, the presence of hybrid boundary condition (pressure and displacement) in the present case is an indicator that analytic methods will be difficult to apply. We therefore use numerical simulations to obtain a useful solution to these equations[*135*](see section 5.6 for the vectorial form of the stress-displacement equations and their boundary conditions).

5.2.3. Fluid-Structure Coupled Interaction

The strong coupling between the flow solution and the structural deformation is due to the third power dependence of the channel height on the pressure drop in an approximately rectangular channel with $W>>h$. Under an imposed flow rate, the pressure distribution inside the channel will cause the structure to deform. The deformation induced in the channel cross section will, in its turn, modify the fluid velocity and the pressure distribution, and so on. Since the hydrostatic pressure is higher near the inlet than at the outlet, the channel deformation is expected to vary along the channel's main axis.

5.2.4. Scaling Analysis

Since the system of equations is complex, a scaling approximation based on physical reasoning is needed to estimate the amount of deformation sustained in the channels. To obtain such a solution, we start by assuming that the maximum strain in the system will be on the order of the one provided by Hooke's law: $e=\sigma/E$. In an infinite medium, all strains are expected to vanish very far from the deforming region. In this particular problem, the characteristic length scale of strain decay is proportional to the width W of the channel, and not to the height (fig. 2). Since the maximum stress observed in the system is proportional to the pressure, the stress-strain scale in the problem becomes

$$e_{vertical} \sim \frac{\Delta h}{W} \sim \frac{p}{E}. \tag{5.4}$$

The same argument can be used on the sides of the channels, where the lateral strain decay length is now proportional to the channel height h. The scale for the lateral deformation ΔW yields, by analogy,

$$e_{lateral} \sim \frac{\Delta W}{h} \sim \frac{p}{E}. \tag{5.5}$$

Comparing eqs. (5.4) and (5.5) reveals that the lateral deformation ΔW can be neglected in the case where $W >> h$, and only the top wall will exhibit significant displacement. The relative maximum thickness variation inside the channel at any position z can therefore be inferred to be

$$\frac{\Delta h_{\max}}{h_0} = c_1 \frac{p(z)W}{Eh_0}, \tag{5.6}$$

where Δh_{max} is the height increase at mid width of the channel under deformation and c_1 is a proportionality constant of magnitude $O(1)$. The linearity of this scale was verified numerically using the coupled model described below. Eq. (5.6) thus provides a natural dimensionless number to characterize the extent of channel deformation. In a channel, when $\Delta pW/Eh_0 << 1$, deformation can be neglected. It must, however, be taken into account in all other cases.

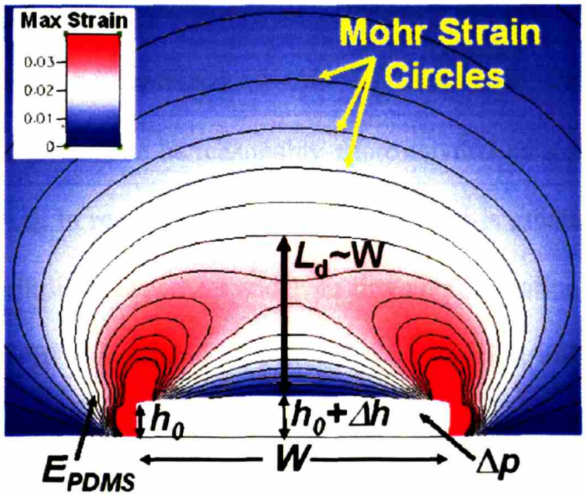

Figure 5.2: Distribution of the principal strain component in a channel cross section far from the inlets. The perturbation of the strain profile near the channel is observed to get as deep in the material as about one width scale. For any point deeper in this infinite medium, we recover the Mohr strain circles, indicating that the solutions asymptotically tends to the one described by a point force acting on a surface (Saint-Venant's principle –Sadd, 2005). The strain decay length scale imposed by the channel can thus be deduced to be $L_{decay} \sim W$.

Assuming that the channel deflects by a distance Δh_{max} and yet remains rectangular would be constantly overestimating the area change and, therefore, underestimating the true channel resistance. A more accurate scale of the effective channel deflection Δh is thus the width-averaged displacement $\langle\Delta h\rangle$ such that the cross section area change remains constant while the channel is still assumed rectangular:

$$\frac{\Delta A}{A_0} = \frac{W\langle\Delta h\rangle}{Wh_0} = \frac{\langle\Delta h\rangle}{h_0}, \tag{5.7}$$

Consequently, at any distance z down the channel, the effective channel height is described by

$$h(z) = h_0\left(1 + \frac{\langle \Delta h \rangle (z)}{h_0}\right). \tag{5.8}$$

For any given channel profile, the relationship between the maximum and the average displacement can always be expressed as $<\Delta h> = c_2 \cdot \Delta h_{max}$. If the deflection is small, the shape of the deforming wall can be reasonably approximated by a parabola, and one can show easily that $c_2=2/3$. In reality, the channel deformation is greater than parabolic, and the true value of c_2 will lie between 2/3 and 1. In first approximation, using eqs. (5.1) and (5.8), the total height of the channel as a function of position will vary with the local pressure as

$$h(z) = h_0\left(1 + \alpha\frac{p(z)W}{E}\right), \tag{5.9}$$

where $\alpha=c_1 \cdot c_2$. From then on, the problem becomes analogous to a flow between tapering plates[*83*], where the tapering is a function of the local pressure *p*(*z*). To couple the structural deformation to the flow profile, eq. (5.9) is introduced in Stokes equation (with r_h/A defined as in eq. (3)) to compute the flow

$$-\frac{\partial p(z)}{\partial z} = \frac{12\mu}{h_0^3 W}\left(1 + \alpha\frac{p(z)W}{Eh_0}\right)^{-3} \cdot Q. \tag{5.10}$$

Even though the true value of α can only be obtained from the fluid-structure interaction simulations, it will be verified through a direct fit to the data that the value of α remains approximately constant for a given channel geometry and is on the order of 1. The solution to eq. (5.10) is equivalent to computing the first order perturbation of the coupled system, assuming the perturbation factor $\varepsilon=\alpha p(z)W/Eh_0$ sufficiently small. It is valid provided that the channel remains roughly rectangular in shape, which is not the case at larger deformations. Integrating eq. (5.10) over axial position with the outlet condition $p(z=L)\equiv 0$ gives

$$Q=\frac{h_0^4E}{48\alpha\mu(L-z)}\left[\left(1+\alpha\frac{p(z)W}{Eh_0}\right)^4-1\right]. \tag{5.11}$$

The total pressure drop is given by eq. (5.11) when $z=0$ and $p(0)=p_0$. When the channel is allowed to deform, eq. (5.11) predicts that the flow rate will vary non-linearly with the applied pressure. The physical significance of this observation resides in the combined effect of the third power dependence of the flow rate on the channel height and the linear dependence of the channel vertical displacement on the width. When the perturbation is small ($\varepsilon\sim 0$), we recover the linear relationship between $p(z)$ and Q of eq. (5.3). However, when the perturbation becomes large ($\varepsilon \gg 1$) the flow rates scales as the fourth power of the pressure.

When using this result, one must be careful not to overlook the existing pressure drops up and downstream of the channel studied. A non-negligible pressure drop in the outlet tubing, for example, would mean that the effective length L to be used is in fact larger than the channel length. The condition on the pressure at the end of the channel will also become $p(z=z_{out})=p_{out}$, altering the result above.

Equation 10 can be used in practice in multiple ways: to compute the effective flow rate coming out of a deforming channel, to determine the non-linear pressure distribution in the channel as a function of position z, or to calculate the pressure drop of a channel deforming under an imposed flow rate Q. The main error in this approximation resides in the channel being considered rectangular at all times. Nevertheless, when the parameter α is fitted, the perturbation approach yielding eq. (5.11) is robust enough that the trend holds for deformations of more than 100% of the channel height (see Fig. 8).

Finally, it is also possible to extract the average cross sectional velocity distribution $U(z)$ along the channel axis. The conservation of mass inside the channel states that at any axial position z,

$$Q = W \cdot h(z) \cdot U(z). \qquad (5.12)$$

Combining eqs. (5.9), (5.11), and (5.12) yields

$$U(z) = \frac{Q}{Wh_0}\left(\frac{48\alpha\mu(L-z)Q}{h_0^4 E}+1\right)^{-1/4}. \qquad (5.13)$$

The average velocity is no longer a linear function of the flow rate. As a consequence, an acceleration of the fluid is expected down the channel length which, scales as

$$\frac{\partial U}{\partial z} \sim \left[1+\frac{(L-z)}{L_a}\right]^{-5/4}, \qquad (5.14)$$

where $L_a = h_0^4 E/48\alpha\mu Q$ is the characteristic acceleration length scale, found from inspection of eq. (5.13).

5.2.5. Numerical Modeling

Simulations of the fluid-structure interaction in PDMS channels were performed using the volume of flow (VOF) and finite element method (FEM) software CFDACE™ (CFDRC Inc.). The solution strategy was based on reducing the steady state coupled flow-deformation problem into a series of uncoupled problems solved by iterations using a deformable grid. The initial pressure in the channel is used to calculate a displacement solution in the solid. The meshing grid is subsequently modified using the displacement output. The flow solution is then recalculated with its updated cross section, yielding a new pressure distribution and velocity field. The new pressure is used to update the grid, and so on, until convergence is achieved. Solutions would typically converge in hours on a regular PC after approximately ten grid update iterations, performed automatically in CFDACE™. Mesh refinement analysis assured that the model error was within 1% of the asymptotic value achievable with a perfectly dense mesh. To model a semi-infinite medium, a thickness of 2 mm of PDMS was used on top of the channels. This thickness ensured that, for the maximal deflections studied (~50 μm or 1/40th of the PDMS thickness), the sum of the residual strains at the top of the PDMS were under 3% of the maximum strain observed in the system. In absolute values, the maximum local strains recorded in the PDMS for a 50 μm displacement were of 8% while the top strain was under 0.25%. In theory, the strains should vanish far from the pressure source in an infinitely thick medium. In practice, there is a large computational cost associated with modeling thick channel walls. Approximating infinity with a 2 mm thick PDMS block was, in our case, sufficient for an accurate analysis of the problem.

5.3. Experimental Section

5.3.1. Microfluidic Setup

Simple linear microfluidic channels were fabricated in Poly(dimethylsiloxane) (Sylgard184™, Corning) using standard soft lithographic procedures. The process yielded channel dimensions of 28 ± 2 μm thick by 1 cm long. Two different widths were studied, namely 250 μm and 500 μm. Inlets were made wider to ensure a minimal pressure drop in that area (calculated to be around 7% of the pressure drop in the channel). PDMS channels were sealed on a glass cover slip (VWR Inc., 170 μm-thick). Leakage at the inlets was prevented using silicone sealant (Loctite corp.) and epoxy (Devcon Inc.). Devices were tested to hold pressures higher than 2 bars before leaking. Special care was taken in preparing the PDMS to use as the bulk of the channel. Temperature, mixing ratios and curing times were carefully controlled to yield PDMS of various elasticity. Their thicknesses were control to be larger than 6 mm to ensure that the semi-infinite medium approximation was valid at all observed deformations. PDMS samples from the same batch were tested in compression using a 50N load cell (Instron corp.) to determine their Young's Moduli. Values between 1 MPa and 3MPa (±10%) were obtained depending on the mixing ratios and curing conditions used.

Flow through the deforming devices was driven using a conventional syringe pump (Harvard Apparatus). A piezoresistive pressure sensor (Honeywell Inc.) was used directly upstream of the microchannel to relate the input flow rate to the pressure drop in the device (Fig. 3).

5.3.2. Confocal Microscopy

A confocal microscope (Zeiss LSM 510) was used to provide 3D imaging of the deforming channels for various input flow rates. Fluorescein-conjugated Bovine Serum Albumin (FITC-BSA, 0.5 mg/ml) was used to provide contrast. Confocal images were acquired, filtered and rendered using Imaris 4.2 image analysis software (Bitplane Inc.). Cross section contours were obtained using built in algorithms from the Matlab image processing toolbox (Mathworks Inc.).

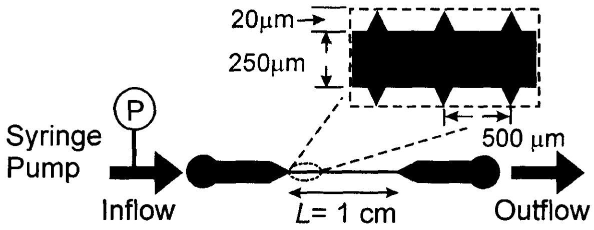

Figure 5.3: Schematics of the microfluidic channel used (channel to scale). Deflection is measured in the channel's narrower region (250 μm or 500 μm). A series of triangular ticks (20 μm side) are patterned at the channel wall every 500 μm for accurate positioning of confocal images. A pressure gauge is set at the entrance of the channel to measure the true pressure drop inside it.

5.4. Results and Discussion

To understand the nature of coupled fluid-structure interactions, a numerical model was used to predict the extent of the channel deformation as well as the resulting pressure distribution inside the device. Simulations also reveal the extent of the flow perturbation due to the channel deformation (Fig. 4). From these results and eq. (5.13) describing the average fluid velocity $U(z)$ at a position z down the channel, we show that the average velocity will increase as we get nearer to the channel outlet since the channel cross section becomes narrower (and the flow rate is constant). This acceleration of the flow in a deforming channel is a potential source of error in predicting quantities such as the wall shear stress in a polymer device.

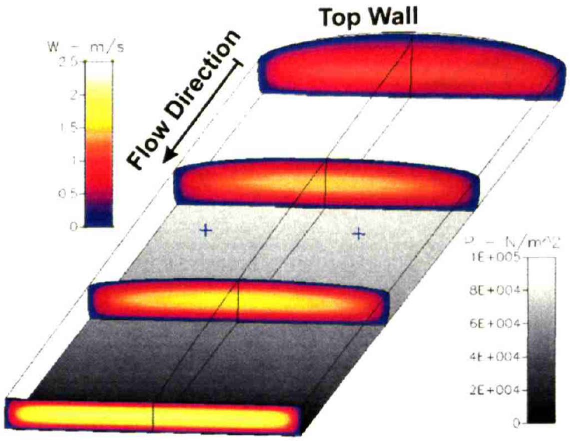

Figure 5.4: 3D simulation of the velocity and pressure profiles under an imposed pressure drop of 1 bar. The channel geometry represented is 25μm x500μm x1cm. Young's modulus is assumed to be of E=1 MPa. The decreasing cross section area along the channel axis is responsible for the change in the fully developed flow profile and for the acceleration of the flow.

5.4.1. Displacement Measurements

Channel deformation was verified directly using confocal microscopy. 3D rendered images of the channels captures in a clear fashion the shape of the channels under various flow conditions (Fig. 5). The experimental data also capture the much higher deformation predicted by the geometry change at the inlets of the device (Figs. 6 and 7, first 3 data points). The rapid tapering of the channel (Fig. 4) translates into an unconstrained displacement (stress-free) boundary condition at the edges. It is also observed both in the model and the entrance data that this effect becomes negligible when we move inside the channel by a distance of a few widths. This entrance effect is not taken into account in the simplified model provided in eq. (5.11) but, as in most applications channels are much longer than wide, neglecting its overall effect is usually a reasonable approximation.

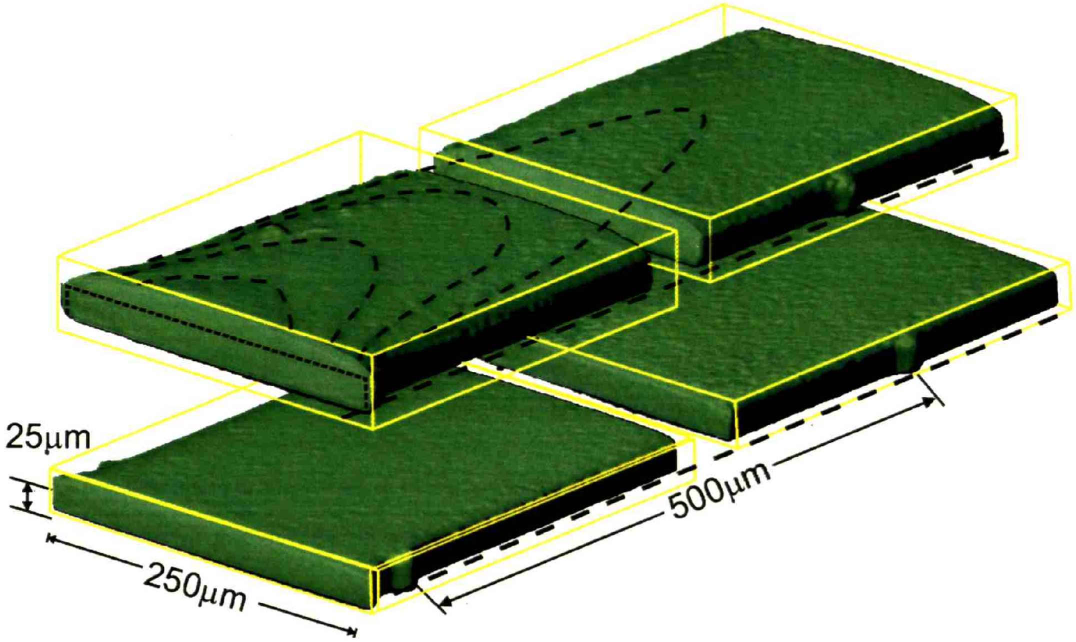

Figure 5.5: 3D rendering of the entrance of two microfluidic channels of the same material and geometry (250 μm wide, 26 μm thick, 1cm long, E=2.2 MPa). Top channel: 300uL/min imposed flow rate. The tapering of the channel can be observed by comparing the cross sections in the first and second segments. Long dash lines: topographic displacement curves. Short dash lines: original channel cross section in the absence of deformation. Bottom channel: 1 uL/min imposed flow rate (reference measurement).

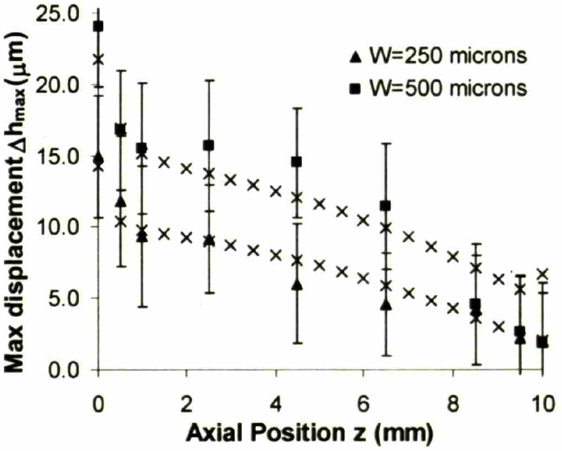

Figure 5.6: Maximum displacement vs axial position (E=2.2MPa). ▲: 26μm x 250μm channel at a flow rate of 300μL/min. ■: 30μm x 500μm channel at a flow rate of 800μL/min. ×: Numerical simulation under the same material and flowconditions.

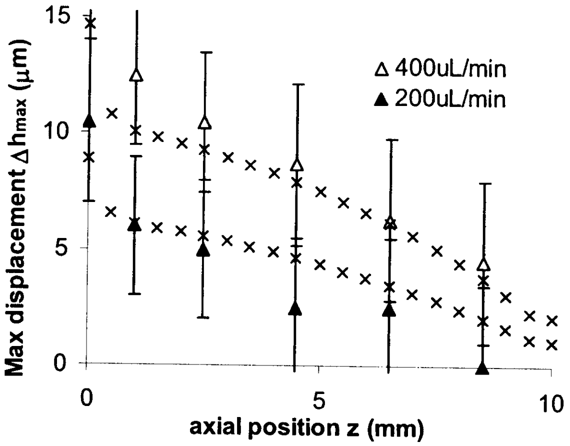

Figure 5.7: Maximum displacement as a function of position (26μm x 250μm channel, E=2.8MPa) for Q = 200 μL/min and 400 μL/min. ×: Numerical simulation under the same material and flow conditions.

Using the same confocal data that was used to produce Fig. 8, the shape of the deforming channel cross-sections was outlined using boundary detection algorithms (Mathworks Inc., Natick, MA). The shape of the cross sections clearly indicates that the side wall deformation, though present, is negligible when compared to the extent of the top wall deformation (Fig. 9).

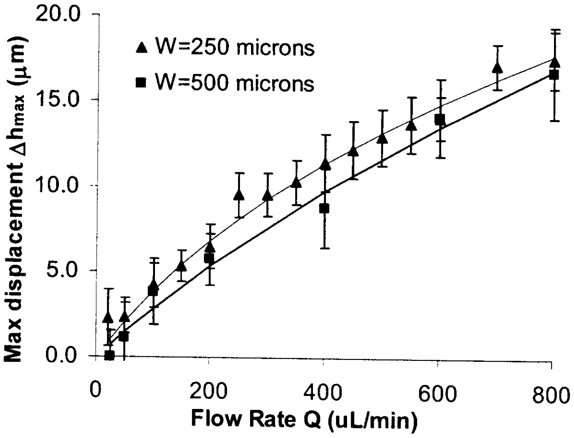

Figure 5.8: Maximum deformation vs flow rate (E=2.2MPa). —: fit from eq. (5.11) using the displacement expression $h=h_0+c_1pW/E$. The fit parameter yields c_1=0.73 (250μm channel) and c_1=0.42 (500μm channel).

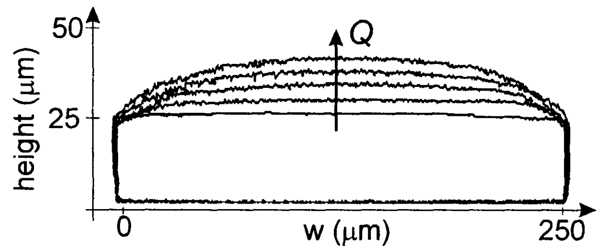

Figure 5.9: Measured Cross section profile at axial position *z*= 1mm for imposed flow rates *Q* = 1, 100, 300, 500, 700 μL/min. 26 x 250 μm^2 initial cross section, E= 2.2 MPa.

5.4.2. Pressure Drop Under Forced Convection

The simplest way to demonstrate the severe effects of channel deformation in conventional microfluidic assays is to monitor the relationship between the total pressure drop over a channel section and the flow rate it induces (and vice versa). In a perfectly rigid channel, it is well established that the pressure drop will vary linearly with the imposed flow rate, as described in eq. (5.2). In Fig. 10, the flow rate imposed in the device is plotted as a function of the measured pressure for two channel geometries and two different elasticity moduli *E*. Results show that the flow rates are much higher than the ones predicted in non deforming channels. For example, in a 30μm x 500μm cross section channel (E=2.2 MPa), the expected flow rate in a rigid channel under a pressure of 1 bar is 270 μL/min while it is measured to be 1600 μL/min in the deforming one (~500% increase). A ratio of the flow rates predicted in eqs. (5.2) and (5.11) yields the following scaling for the amount of increased flow rate at small deformations ($\Delta h/h_0 \ll 1$):

$$\frac{\Delta Q}{Q} = \frac{Q_{\text{deform}} - Q_{\text{rigid}}}{Q_{\text{rigid}}} \sim \frac{3\alpha}{2}\frac{\Delta p W}{E h_0}. \tag{5.15}$$

Thus, if the channel were 100 μm-thick, ceteris paribus, the relative variation in the flow rate would now be only ~25%. However, following a similar reasoning, a 5 μm-thick channel would now suffer from a 25 fold deviation in the expected flow rate. The height dependence is expected to be even more important at larger deformations ($\Delta Q/Q \sim (\Delta h/h_0)^4$). The consequence of this observation is to impose a severe constraint on the design and operation of PDMS channel networks at the scale of a few microns.

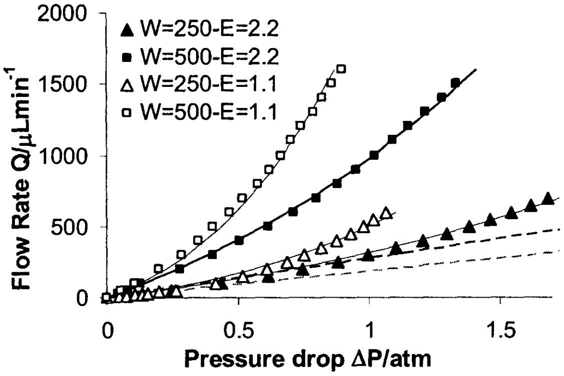

Figure 5.10: Channel flow rate as a function of channel pressure drop. – –: expected flow rate in the absence of channel deformation for W=250 μm (▲,Δ) and W=500μm (■,□).—: fit of eq. (5.11) to the data. The fit parameter α was found to be α= 0.33 (30μm x 500μm -2.2MPa), α=0.55 (26μm x250μm -2.2MPa), α=0.67 (26μm x 250μm -1.1MPa), and α=0.56 (26μm x 500μm -1.1MPa).

5.5. Conclusion

Rapid prototyping in PDMS possesses many well known advantages over silicon micromachining, such as its low cost and quick turnaround time. However, at the micron scale, these advantages may not counterbalance the losses in control of device operation due to channel deformation. In this paper, we have reported the effect of flow on polymer channel deformation in microdevices (and vice versa). From scaling analysis, we have provided a dimensionless number ($\Delta p W/E h_0$) to quickly assess whether the application used will incur deformation or not. Based on the experimental results and the numerical analysis provided, 3 main consequences of channel deformation can be elicited.

1) Cross section effects: For channel with low aspect ratio, the amount of deflection under pressure is proportional to the channel width and neither to the channel height h nor the PDMS wall thickness H provided that ($\Delta h_{max} << H$). It ensues from this observation that thinner channels will suffer higher relative changes in their cross section areas and will therefore be more sensitive to deformation. In this study, we used ~25 µm-thick channels for the sake of getting a better resolution in the confocal imaging. The effect would have nonetheless been markedly larger in, say, 5 µm-thick channels. For the same reason, channel deformation will, in general, disappear when the channels are thick enough.

2) Stream-wise effects: Channel deformation is not even along the channel's stream-wise axis but rather decreases non-linearly along the length of the channel to reach zero at the outlet. This steady decrease in cross section area causes a steady acceleration of the fluid velocity along the axis. This change in velocity will make diffusion/convection time scales and shear stresses uneven throughout the channel, thus introducing new difficulties to control these experiments in narrow channels.

3) Flow rates and pressure effects: For a given flow rate, the pressure drop in an elastomeric channel is observed to be much less than that of a rigid channel. This result will affect the prediction of the maximum tolerated flow in a device. Indeed, the deformable devices will be able to handle much higher flow rates than expected without leaking due to the channel compliance.

In all these cases, increasing the rigidity of polymer channels will decrease the amount of deformation and thus all of the aforementioned effects. Possible ways to achieve higher effective bulk moduli vary. Curing PDMS for longer times (>24h) at higher temperatures

(120°C) with more curing agent have been reported to increase the elasticity modulus of PDMS to E=4 MPa[26]. Enchasing glass microslides close to the channel surface in the unbaked polymer is another example of a simple way to avoid large deformations and its effect in polymer-based microfluidic systems.

5.6. Analytic Supplement

Appendix- Elasticity Problem Formulation

We refer the reader to the book by Sadd[*135*] for a more complete development of the elasticity equations. In absence of body forces, the internal displacement equations governing elastic deformation are described by Lamé's equation:

$$\bar{\nabla}^2 \bar{u} + \left(\frac{2\nu}{(1-2\nu)} \right) \bar{\nabla}(\bar{\nabla} \cdot \bar{u}) = \bar{0} . \tag{5.16}$$

where the displacement vector is given by

$$\bar{u} = u_1(x,y,z)\hat{x}_1 + u_2(x,y,z)\hat{x}_2 + u_3(x,y,z)\hat{x}_3 . \tag{5.17}$$

The unit vectors $\hat{x}_i$ point in the direction of x, y and z. At the interface of the PDMS block, the boundary conditions are of a third kind (mixed traction and displacement) and read:

$$\begin{gathered} \bar{u} = \bar{0} \text{, for glass-PDMS interface.} \\ \underline{\underline{\sigma}} \cdot \bar{n} = p(z)\bar{n} \text{, for fluid-PDMS interface,} \end{gathered} \tag{5.18}$$

where $\bar{n}$ is the unit vector normal to the interface. Using the displacement formulation and Hooke's generalized law, the stress value can be converted to strain values and thus to displacement. Lumping theses steps together provide the stress-displacement relationships in the PDMS.

$$\sigma_{ij} = \frac{E\nu}{(1-2\nu)(1+\nu)} \bar{\nabla} \cdot \bar{u} \delta_{ij} + \frac{E}{(1+\nu)} \left(\frac{\partial u_i}{\partial x_j} + \frac{\partial u_j}{\partial x_i} \right). \tag{5.19}$$

The elasticity equations are coupled to Navier-Stokes flow by the pressure *p*(*z*) in eq. (5.1). When dealing with numerical simulations in incompressible media, a poisson ratio of ν=0.499 is used in CFDACE instead of ν=0.5 to prevent the numerical divergence of the problem.

Chapter 6. General Conclusion

6.1. Thesis Contributions

The main aim of this thesis was to develop the theoretical foundations required to control and improve on-chip biological sensing, from characteristic length scales of tens of microns to the single micron scale. In the μTAS community, the reduction in size of on-chip sensors has been a long standing goal as it is a promise of faster analysis times, lower sample consumption and greater integration. This thesis shows that these principles do not always hold true when sensors reach characteristic lengths in the single micron range (1-10 μm). At this scale, many of the physical behaviors expected from larger microsystems disappear, and a new approach must be taken to predict their performances. This thesis contributes to the understanding of single micron scale sensors under three different topics.

6.1.1. Mass Transport and Surface Reaction

In Chapter 2, it is demonstrated through a detailed analysis of convection-diffusion-reaction transport equations that the theory commonly used to describe transport to surfaces in microsensors breaks down in channels of a few microns thick or smaller. Transport no longer occurs from the bulk to the surface through a diffusive mass transfer boundary layer. Instead, surface binding is limited by the influx of analytes inside the channel, a behavior that we named "convection-limited transport". This form of transport, not previously described in the microfluidics community, has been characterized through analysis and numerical simulations[*136*]. In addition to the new model proposed, the complete set of analytic solutions used to characterize chemical transport and surface reactions in microchannels was compiled.

Two key experimental parameters were quantified in each of these transport regimes: the analyte capture fraction and the surface saturation time scale. The results provide useful device design criteria for the experimentalist to predict and control a device behavior given its geometry and operation conditions.

As a complement to the theoretical analysis, Chapter 3 provides experimental observation of convection-limited transport in shallow microfluidic sensors. The results confirm the theoretical prediction that surface binding induces a delay in analyte flow of several orders of magnitude[*137*]. This retardation effect is shown to decrease with increasing bulk analyte concentration.

6.1.2. Application to Biological Sensors

One of the most important applications of on-chip sensors is to measure surface binding in a real time fashion to extract kinetics rate constants. In chapter 4, we determined whether protein interaction kinetics can be measured in the presence of convection-limitations. As a case study, we chose a novel sensing method based on the resonance of a microcantilever traversed by a 1 um-thick fluidic channel in which binding occurs. In a first step, we described how the frequency output signal of the device can be correlated directly and in real time to the adsorbed mass inside the fluidic channel. To proceed, we expanded the current theory on dynamic response of resonating cantilevers to include the effect of non-uniform mass distributions. Based on this model, we showed the impact of convection-limited transport in sensor signals and discuss ways of measuring kinetics despite these limitations. We concluded by providing guidelines on sensor design and optimization through theoretical modeling.

6.1.3. General Microfluidics

The reduction of sensor sizes also imposes structural constraints on it. As the channel cross section decreases, the hydraulic resistance augments drastically, thus requiring much higher pressures to achieve the same fluid velocities. This pressure imposes mechanical stresses in the device's structure and can cause them to deform. This is particularly true in polymer devices such as the ones created by soft lithography. In chapter 5, we concluded our work by a study of flow-induced deformation in microfluidic channels[*138*]. Through scaling analysis and numerical simulations based on coupled fluid-structure interaction models, we characterized the extent of deformation and provided design criteria to either avoid or maximize deformation. We also demonstrated how the high non-linearity of pressure-flow rate curves becomes a source of error in many microfluidic applications. The predictions based on the modeling were confirmed by experimental observations in conventional microchannels fabricated with soft-lithography techniques.

6.2. Outlook and Research Perspective

Research progress in microfluidic technology is often compared to the development of microelectronics. Both share the quest for miniaturization, faster analysis and the highest possible degree of integration. In microelectronics research, progress has led to the advent of portable computers and, more globally, to a revolution in information processing and storage. Microfluidics seeks essentially the same: a revolution in biochemical information processing and storage fueled by the development of highly integrated sensors capable of measuring protein abundance and activity in real time.

In order to slowly march towards that goal, several challenges must be met by the community; the main ones are summarized in the following discussion.

Integration and Packaging

As mentioned earlier in this work, the approach to engineering research in the microfluidics community has been a modular one. Multiple research groups have been developing efficient devices of their own with little potential for integration with devices created by other groups. These incompatibilities often arise from different flow rate requirements, incompatible solvents and chemistries, or the need for bulky and complex macrosystems to operate the micro ones. Developing a general microfluidic platform as a standard way to deliver fluid samples, gases and external stimuli (light, heat) is one necessary step to achieve the level of integration required to perform useful biological tasks.

Surface Engineering

While producing the experimental results necessary to observe surface saturation under convection-limited transport (chapter 3), an important practical limitation arose. Once the binding of an antigen occurred to its surface-bound antibody and the detection has been performed, it becomes extremely difficult to regenerate the sensor's surface so that another measurement can be performed in the same device.

The same type of difficulties appears in almost every microfluidic application in the form of non-specific adsorption at the wall, depleting samples and introducing noise in protein-specific signals. A possible way to avoid these difficulties is to create an entirely disposable sensing unit connected to a permanent operating system but there remains the problem of delivering the fluid to the unit, introducing yet another packaging challenge.

Sensitivity and Signal Selectivity

Signal transduction proteins account for only approximately 12% of the variety of proteins in found in the human genome[*139*]. In number of copies, however, they account for a much smaller fraction of all proteins found in a given cell. In order to detect them, very sensitive and selective sensors will be required. Immunoassays are a very specific kind of assays with the disadvantage that antibodies need to be engineered to target every kind of protein to be detected.

As argued throughout this thesis, the general trend in biological sensing technology is to move toward the nanoscale. The control of material properties is currently giving rise to novel detection schemes which could potentially be integrated in microfluidic devices. Carbon nanotubes[*140, 141*] are a promising way to build electrodes for label-free single-molecule sensing. Along with nanocantilever arrays[*67, 142*]and multiple other devices in the realm of nanobiotechnology[*143*], they constitute the future of label-free detection. No matter how small these sensor elements are, they will have to be integrated in lab-on-a-chip devices just as their larger counterparts. Mass transfer design considerations will remain essentially the same. Consequently, the usefulness of the models developed in this thesis to understand the fundamental limits of on-chip biosensors will remain unaltered.

The Role of the Modeler

In the search for the optimal on-chip sensor, engineers and scientist are only limited by their own creativity. Important investments of time and capital are made in the design and characterization of every device prototype in often long series of iterations based on trial and error. Through this iterative process, an invaluable amount of time can be saved by making the correct assumptions on the underlying physics. Is the flow distribution adequate in the fluidic network? Is the reaction mass transfer-limited? Can I really measure kinetics with such a detection scheme? Is the device susceptible to deform? In this thesis, we provided answer to many of these questions in a systematic way.

Dimensionless numbers obtained through were invaluable criteria to achieve this task. They provided a quick route for the experimentalist to estimate the importance of competing processes in a device and thus convenient criteria to be used in the design process. The role of the modeler is however not limited to the development of such theories, but also to point out to the scientific community the most relevant theories that apply to a particular experimental problem.

Finally, the greatest advantage of analysis is that results are easily generalized and transferable. Once a theory is developed to explain the functioning of a particular sensor, it can often be generalized to other problems, many of which not anticipated in the original analysis. After all, could Leo Graetz (1856-1941) have suspected that his seminal work on heat transfer in tubes[*144*] would be used to develop micron-size mass sensors to advance our knowledge of biology and medicine?

Appendices – Analytic and Modeling Supplement

A1. Analytic Solution to the Graetz Problem in Parallel Plate Geometry with Arbitrary Damköhler numbers

This appendix displays the MAPLE^{TM} code used to solve the full Graetz Problem (Table 2.3) analytically using first order reactions. The two algorithms presented differ only in that they assume either reaction at both walls (case A) or reaction at the bottom wall only (case B). For references on the method used (Sturm-Liouville theory and eigenfunction expansions) see Varma A. & Morbidelli M., "Mathematical Methods in Chemical Engineering" [*145*], and Deen WM, "Analysis of Transport Phenomena" [*83*]. Figures are not numbered but are described in the comments.

A1.1 Solution to Graetz Problem in Parrallel Plate Geometry With Equal First Order Reaction at Both Walls

Work performed by Thomas Gervais, MIT, using Maple version 8 - March 2004

Initializes the Work sheet. Assigns the domain of validity of the main variables.

```
> restart; unassign('eta','GP(eta)'): assume(eta>=0): assume(lambda>=0): Digits:=15:
alias('M'=KummerM):
```

General Solution for Planar Geometries

Full PDE expression:

```
> Graetz:= diff(C(x,z,t),t)= D*diff(C(x,z,t),x$2)-6*U*(1/4-(x/h)^2)*diff(C(x,z,t),z);
```

Using dimensionless notation: eta=x/h, zeta=z/Pe/h, tau= Dt/h^2, Theta= C/C[0]

```
> Graetz_adim:= diff(Theta(eta,zeta,tau),tau)= diff(Theta(eta,zeta,tau),eta$2)-6*(1/4-
eta^2)*diff(Theta(eta,zeta,tau),zeta);
```

$$Graetz := \frac{\partial}{\partial t} \mathrm{C}(x, z, t) = \mathrm{D}\left(\frac{\partial^2}{\partial x^2} \mathrm{C}(x, z, t)\right) - 6\, U\left(\frac{1}{4} - \frac{x^2}{h^2}\right)\left(\frac{\partial}{\partial z} \mathrm{C}(x, z, t)\right)$$

$$Graetz\_adim := \frac{\partial}{\partial \tau} \Theta(\eta\sim, \zeta, \tau) = \left(\frac{\partial^2}{\partial \eta\sim^2} \Theta(\eta\sim, \zeta, \tau)\right) - 6\left(\frac{1}{4} - \eta\sim^2\right)\left(\frac{\partial}{\partial \zeta} \Theta(\eta\sim, \zeta, \tau)\right)$$

Using separation of Variables, the problem can be divided in three ordinary differential equations of the form:

```
> pdsolve(Graetz_adim, Theta(eta,zeta,tau));
```

Which we rewrite, using the separation variables -lambda^2 and -kappa^2

```
> eq_tau:= diff(T(tau),tau)+kappa^2*T(tau);
```

```
> eq_zeta:= diff(Z(zeta),zeta)+lambda^2/6*Z(zeta);
> eq_eta:= diff(H(eta),eta$2)+lambda^2*(1/4-eta^2)*H(eta);
```

$$(\Theta(\eta\sim,\zeta,\tau)=\_F1(\eta\sim)\,\_F2(\zeta)\,\_F3(\tau))\ \&\text{where}\left[\{\frac{d}{d\zeta}\_F2(\zeta)=\_c_2\,\_F2(\zeta),\frac{d}{d\tau}\_F3(\tau)=\_c_3\,\_F3(\tau),\frac{d^2}{d\eta\sim^2}\_F1(\eta\sim)=\left(\frac{3}{2}\_F1(\eta\sim)-6\,\_F1(\eta\sim)\,\eta\sim^2\right)\_c_2+\_F1(\eta\sim)\,\_c_3\}\right]$$

$$eq\_tau:=\left(\frac{d}{d\tau}\mathrm{T}(\tau)\right)+\kappa^2\,\mathrm{T}(\tau)$$

$$eq\_zeta:=\left(\frac{d}{d\zeta}\mathrm{Z}(\zeta)\right)+\frac{1}{6}\lambda\sim^2\,\mathrm{Z}(\zeta)$$

$$eq\_eta:=\left(\frac{d^2}{d\eta\sim^2}\mathrm{H}(\eta\sim)\right)+\lambda\sim^2\left(\frac{1}{4}-\eta\sim^2\right)\mathrm{H}(\eta\sim)$$

The first two ODEs possess simple solutions:

```
> dsolve(eq_tau,T(tau)); dsolve(eq_zeta,Z(zeta));
```

$$\mathrm{T}(\tau)=\_C1\,\mathrm{e}^{(-\kappa^2\,\tau)}$$

$$\mathrm{Z}(\zeta)=\_C1\,\mathrm{e}^{\left(-\frac{\lambda\sim^2\,\zeta}{6}\right)}$$

The ode expressing the vertical concentration profile H(eta) is more complex:

```
> G_plan_diff:=diff(diff(GPl(eta),eta),eta)+(1/4-eta^2)*lambda^2*GPl(eta);
```

The solution to G_plan_diff provides the problem's eigenfunctions

```
> G_plan:= dsolve(G_plan_diff): G_plan_Kum:= simplify(convert(G_plan,hypergeom));
>
>
```

$$G\_plan\_diff:=\left(\frac{d^2}{d\eta\sim^2}\mathrm{GPl}(\eta\sim)\right)+\left(\frac{1}{4}-\eta\sim^2\right)\lambda\sim^2\,\mathrm{GPl}(\eta\sim)$$

$$\begin{aligned}G\_plan\_Kum:=\mathrm{GPl}(\eta\sim)=\lambda\sim^{(1/4)}\Big(&\_C1\ \mathrm{hypergeom}\left(\left[\frac{3}{4}-\frac{\lambda\sim}{16}\right],\left[\frac{3}{2}\right],\lambda\sim\eta\sim^2\right)\eta\sim\,\Gamma\left(\frac{3}{4}-\frac{\lambda\sim}{16}\right)\Gamma\left(\frac{1}{4}-\frac{\lambda\sim}{16}\right)\sqrt{\lambda\sim}\\&+\_C2\sqrt{\pi}\ \mathrm{hypergeom}\left(\left[\frac{1}{4}-\frac{\lambda\sim}{16}\right],\left[\frac{1}{2}\right],\lambda\sim\eta\sim^2\right)\Gamma\left(\frac{1}{4}-\frac{\lambda\sim}{16}\right)\\&-2\,\_C2\sqrt{\pi}\ \mathrm{hypergeom}\left(\left[\frac{3}{4}-\frac{\lambda\sim}{16}\right],\left[\frac{3}{2}\right],\lambda\sim\eta\sim^2\right)\sqrt{\lambda\sim}\,\eta\sim\,\Gamma\left(\frac{3}{4}-\frac{\lambda\sim}{16}\right)\Big)\mathrm{e}^{\left(-\frac{\lambda\sim\eta\sim^2}{2}\right)}\Big/\left(\Gamma\left(\frac{3}{4}-\frac{\lambda\sim}{16}\right)\Gamma\left(\frac{1}{4}-\frac{\lambda\sim}{16}\right)\right)\end{aligned}$$

```
>
```

Boundary Conditions for fully diffusion-limited problem

The general boundary conditions are:

1- No flux at the symmetry line

```
> diff(H(eta),eta)[eta=0]=0;
```

2- Instantaneous consumption reaction at the wall

```
> H(eta=1/2)=0;
```

$$\left(\frac{d}{d\eta\sim}\mathrm{H}(\eta\sim)\right)_{\eta\sim=0}=0$$

$$\mathrm{H}\left(\eta\sim=\frac{1}{2}\right)=0$$

This procedure applies the first boundary condition to find the form of the eigenfunctions

```
> eigenfunction:= proc(eta_,lambda_) local C1,C2,sol;  diff(op(2,G_plan_Kum),eta);
simplify(subs(eta=0,%)); C2:=solve(%,_C2); sol:=subs(_C2=C2,op(2,G_plan_Kum)); C1:=
subs(eta=0,%);  subs(lambda=lambda_,eta=eta_,simplify(sol/C1)); convert(%,M) end proc;
```

```
>
eigenfunction := proc (eta_, lambda_)
local C1, C2, sol;
    diff( op( 2, G_plan_Kum ), η );
    simplify( subs( η = 0, % ));
    C2 := solve( %, _C2 );
    sol := subs( _C2 = C2, op( 2, G_plan_Kum ));
    C1 := subs( η = 0, % );
    subs( λ = lambda_, η = eta_, simplify( sol/C1 ));
    convert( %, M)
end proc
```

The eigenfunction can be expressed using confluent hypergeometric functions or Kummer M functions as:

```
> eigenfunction(eta,lambda);
```

$$\mathrm{M}\left(\frac{1}{4}-\frac{\lambda\sim}{16},\frac{1}{2},\lambda\sim\eta\sim^2\right)\mathrm{e}^{\left(-\frac{\lambda\sim\eta\sim^2}{2}\right)}$$

Applying the second boundary condition to the eigenfunction provides the eigenvalue equation:

```
> dirichlet_1_C1:= subs(eta=1/2, eigenfunction(eta,lambda));
```

$$dirichlet\_1\_C1 := \mathrm{M}\left(\frac{1}{4}-\frac{\lambda\sim}{16},\frac{1}{2},\frac{\lambda\sim}{4}\right)\mathrm{e}^{\left(-\frac{\lambda\sim}{8}\right)}$$

Solving For Eigenvalues

This section finds the first n eigenvalues of the expansion

```
> eigen_f:= lambda_-> simplify(subs(lambda=lambda_,dirichlet_1_C1));
```

$$eigen\_f := lambda\_ \rightarrow \mathrm{simplify}(\mathrm{subs}(\lambda = lambda\_, dirichlet\_1\_C1))$$

The zeros of this plot correspond to the eigenvalues of the problem. They can be roughly located and then precisely calculated using built-in Maple function solver "fsolve"

```
> plot(eigen_f(lambda),lambda=0..100);
```

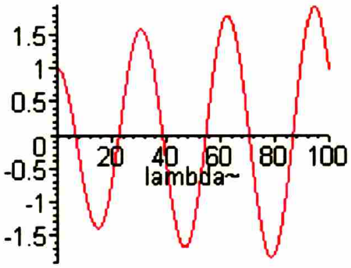

first eigenvalues:

```
> eig_1:= fsolve(eigen_f(lambda),lambda=3.5);
evalf([seq(fsolve(eigen_f(lambda),lambda=6.6+16*k),k=0..4)]);
```

$$eig\_1 := 6.72638128895594$$

$$[6.72638128895594, 22.6794293835803, 38.6729698500416, 54.6706457704302, 70.6694942613971]$$

Sherwood number

This Sh is normalized on a per surface basis and compared with the value found in Shah and London.

```
> 'Sh[infinity]=1/12*lambda[1]^2'= 1/12*eig_1^2; Shah:= 7.54070087/2;
```

$$\left(Sh_{\infty}=\frac{1}{12}\lambda_1^2\right)=3.77035043703472$$

$$Shah := 3.77035043500000$$

Partially Diffusion-Limited Surface Reactions

To include the effect of partial reaction limitations at the surface due to finite Damkohlers, we use the same reasoning. The eigenfunctions remain identical, but we modify the boundary condition that yields the eigenvalue equations.
THIS IS THE MASTER DAMKOHLER NUMBER FOR WHICH THE SOLUTION IS COMPUTED BELOW. Changing the value of this Global Variable will modify the calculations for the entire page.

```
> Da_M:=1;
```

THIS IS THE NUMBER OF TERMS TAKEN INTO ACCOUNT

```
> nb_max:=8;
```

As above, the eigenfunctions read:

```
> eigenfunction(eta,lambda);
```

$$Da\_M := 1$$

$$nb\_max := 8$$

$$\mathrm{M}\left(\frac{1}{4}-\frac{\lambda\sim}{16}, \frac{1}{2}, \lambda\sim\,\eta\sim^2\right) \mathrm{e}^{\left(-\frac{\lambda\sim\,\eta\sim^2}{2}\right)}$$

The second boundary condition now becomes a boundary condition of the third kind (Robin Boundary Condition)

```
> Robin_BC:= diff(H(eta),eta)+Da*H(eta)=0;
```

Computes the new eigenvalue equation, now dependent on two variables: lambda and Da

```
> eigen_robin:= proc(lambda,Da) local dif; diff(eigenfunction(eta,lambda),eta); dif:=
subs(eta=1/2,%); dif+Da*eigenfunction(1/2,lambda); simplify(%); end proc;
```

$$Robin\_BC := \left(\frac{d}{d\eta\sim}\mathrm{H}(\eta\sim)\right) + Da\,\mathrm{H}(\eta\sim) = 0$$

eigen_robin := **proc** (λ, *Da*)
local *dif*;
diff(eigenfunction(η, λ), η); *dif* := subs(η = 1/2, %); *dif* + *Da*×eigenfunction(1/2, λ); simplify(%)
end proc

From the second boundary condition involving Da, we extract the Eigenvalue equation: Eigen_robin(lambda,Da)

```
> eigen_robin(lambda,Da);
plot(eigen_robin(lambda,Da_M),lambda=0..100,title='zeros_of_the_eigenvalue_function');
```

$$\frac{1}{4}\mathrm{e}^{\left(-\frac{\lambda\sim}{8}\right)}\left(\mathrm{M}\left(\frac{1}{4}-\frac{\lambda\sim}{16}, \frac{1}{2}, \frac{\lambda\sim}{4}\right)\lambda\sim - 4\,\mathrm{M}\left(\frac{1}{4}-\frac{\lambda\sim}{16}, \frac{1}{2}, \frac{\lambda\sim}{4}\right) + 4\,\mathrm{M}\left(-\frac{3}{4}-\frac{\lambda\sim}{16}, \frac{1}{2}, \frac{\lambda\sim}{4}\right) + \mathrm{M}\left(-\frac{3}{4}-\frac{\lambda\sim}{16}, \frac{1}{2}, \frac{\lambda\sim}{4}\right)\lambda\sim \right.$$
$$\left. + 4\,Da\,\mathrm{M}\left(\frac{1}{4}-\frac{\lambda\sim}{16}, \frac{1}{2}, \frac{\lambda\sim}{4}\right)\right)$$

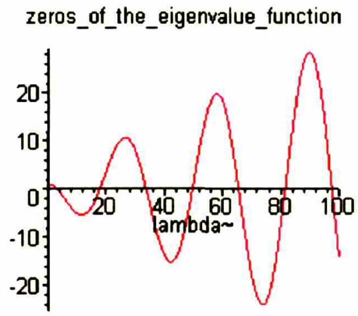

This section determines the first nb_max eigenvalues. NOTE: The algorithm to extract the roots does not always work, so verify that all eigenvalues returned are different and ordered. Consult the plot above to be more sure.

```
> lambda_set:=evalf([seq(fsolve(eigen_robin(lambda,Da_M),lambda= 5+16*(k-
1)),k=1..nb_max)]);
>
```

lambda_set := [3.10203107606564 , 17.9834445985570 , 33.7725218722339 , 49.6770562288525 , 65.6208527732453 ,
81.5831642921751 , 97.5558321622730 , 113.534942614764]

We define here an inner product used to compute the coefficients of the eigenfunction expansion

```
> inner_prod:= proc(f,lambda,Da) int(2*(1/4-
```

```
eta^2)*eigenfunction(eta,lambda)*f,eta=0..1/2); evalf(%); end proc;
inner_prod := proc (f, λ, Da) int(2×(1/4 – η^2)×eigenfunction(η, λ)×f, η = 0 .. 1/2); evalf(%) end proc
```

This is an example of the use of the inner product to calculate the value of the first eigenfunction against itself

```
> inner_prod(eigenfunction(eta,lambda_set[1]),lambda_set[1],Da_M);
                                0.149393019151426
```

This computes the norm of the first nb_max eigenfunctions. <Gk|Gk>=normk. NOTE: 1/sqrt(norm)= normalization coefficient of the eigenfunctions such that <Gknorm|Gknorm>=1
Computationnally intensive (~15 s per term)

```
>
norm_set:=[seq(inner_prod(subs(lambda=lambda_set[k],eigenfunction(eta,lambda)),lambda_
set[k],Da_M),k=1..5)];
norm_set :=
    [0.149393019151426 ,0.101480463966268 ,0.0993169102141278 ,0.0987663349991022 ,0.0985423412600415 ]
```

This procedure computes the first coefficients of the eigenfunction such that F(eta, zeta=0)= sum(ai*Gi(eta)). It is done for the initial condition f(eta,zeta=0)=1.
This step is computationnally intensive (~15 seconds per term)

```
> a_coeff_set:=
[seq(inner_prod(1,lambda_set[k],Da_M)/inner_prod(eigenfunction(eta,lambda_set[k]),lamb
da_set[k],Da_M),k=1..5)];
a_coeff_set := [1.05439953081752 ,-0.0702247611159831 ,0.0231974022075540 ,-0.0116350579600006 ,
    0.00704945979000803 ]
```

The full solution thus writes:

```
> Theta(eta,zeta,tau)= Sum(a[n]*eigenfunction(eta,lambda[n])*exp(-
lambda[n]^2/6*zeta)*(1-exp(-kappa^2*tau)),n=1..infinity);
>
```

$$\Theta(\eta\sim,\zeta,\tau)=\sum_{n=1}^{\infty} a_n\,\mathrm{M}\left(\frac{1}{4}-\frac{1}{16}\lambda\sim_n,\frac{1}{2},\lambda\sim_n\,\eta\sim^2\right)\mathbf{e}^{\left(-1/2\,\lambda\sim_n\,\eta\sim^2\right)}\,\mathbf{e}^{\left(-1/6\,\lambda\sim_n^{\,2}\,\zeta\right)}\left(1-\mathbf{e}^{\left(-\kappa^2\,\tau\right)}\right)$$

The value of kappa is not calculated here because the Graetz problem assumes time steady state. We put it for completion, but the steady state assumption proved to be satisfied (pseudo-steady state) for our particular problem.
Also, from an engineering point of view, it is not important to know the concentration distribution in the eta direction. A more compact solution to be used is found using velocity-averaged coefficients:

```
> Theta[b](zeta)= Sum(A[n]*exp(-1/6*lambda[n]^2),n=1..infinity);
```

with coefficients A:

```
A_coeff_set:=
[seq(6*inner_prod(1,lambda_set[k],Da_M)^2/inner_prod(subs(lambda=lambda_set[k],eigenfu
nction(eta,lambda)),lambda_set[k],1e12),k=1..5)];
```

$$\Theta_b(\zeta)=\sum_{n=1}^{\infty} A_n\,\mathbf{e}^{\left(-1/6\,\lambda\sim_n^{\,2}\right)}$$

```
A_coeff_set := [0.996533637294252 ,0.00300271584423889 ,0.000320666178029567 ,0.0000802227029977920 ,
    0.0000293823009124527 ]
```

The sum of the coefficients at the origin (zeta=0) should give 1:

```
> test_sum:=sum(A_coeff_set[k],k=1..5);
                                test_sum := 0.999966624320431
```

Sherwood number

This section computes the Sherwood number for the fully developed region including the effect of reaction limit at the wall. It also computes the diffusion/reaction mass transfer coefficient kd/r found in the Chem. Eng. Sci. Paper (Gervais et. al, 2005).

```
> eig_Da_1:= proc(Da) fsolve(eigen_robin(lambda,Da),lambda= 6.6*(Da+0.01)/(1+Da)); end
proc;
> eig_Da_1(Da_M);
>  'D/h*(1/k[m]+1/k[r])=(1/(3/(lambda[1](Da))^2+1/Da))'=
(1/(12/eig_Da_1(Da_M)^2+1/Da_M));
> k[dr]:= 'lambda^2/6'=eig_Da_1(Da_M)^2/6;
```

```
>
eig_Da_1 := proc (Da) fsolve( eigen_robin( λ, Da ), λ = 6.6×( Da + 0.01 )/( Da + 1 ) ) end proc
```

$$3.10203107606564$$

$$\left(\frac{D\left(\frac{1}{k_m}+\frac{1}{k_r}\right)}{h} = \frac{1}{\frac{3}{\lambda_1(Da)^2}+\frac{1}{Da}} \right) = 0.445025030400917$$

$$k_{dr} := \frac{\lambda^2}{6} = 1.60376613281283$$

This section computes the diffusion reaction mass transfer coefficient kdr for various Damkohler numbers.

```
> kdr:= Da-> eig_Da_1(Da)^2/6;
> seq_Sh:=[seq([m/10,kdr(m/10)],m=0..20)]:
```

With the upper limit being:

```
> kdr(1e20);
>
```

$$kdr := Da \rightarrow \frac{1}{6}\,\mathrm{eig\_Da\_1}(Da)^2$$

$$7.54070087406943$$

A vector is built containing the value of kdr at various Da numbers:

```
> mmax:=30; seq_m:=[seq(m,m=1..mmax)]: seq_lambda:=[seq(eig_Da_1(-m*4/mmax^2+m^2*2/mmax
),m=0..mmax)]: seq_plot_lambda:= [seq([-m*4/mmax^2+m^2*2/mmax,eig_Da_1(-
m*4/mmax^2+m^2*2/mmax )],m=0..mmax)]:
>
```

$$mmax := 30$$

The vector values are plotted

```
> # kdr vs Da
> plot(seq_plot_lambda);
```

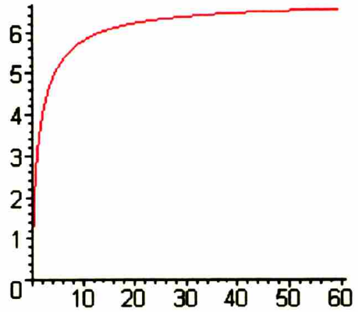

END of Code.

A1.2 Solution to Graetz Problem in Parrallel Plate Geometry With First Order Reaction at Only One Wall

Initializes the Work sheet. Assigns the domain of validity of the main variables.

```
> restart; unassign('eta','GP(eta)'): assume(eta>=0): assume(lambda>=0):
alias('M'=KummerM): Digits:=15:
```

General Solution for Planar Geometries

Full PDE expression:

```
> Graetz:= diff(C(x,z,t),t)= D*diff(C(x,z,t),x$2)-6*U*x/h*(1-x/h)*diff(C(x,z,t),z);
```

Using dimensionless notation: eta=x/h, zeta=z/Pe/h, tau= Dt/h^2, Theta= C/C[0]

```
> Graetz_adim:= diff(Theta(eta,zeta,tau),tau)= diff(Theta(eta,zeta,tau),eta$2)-
6*eta*(1-eta)*diff(Theta(eta,zeta,tau),zeta);
```

$$Graetz := \frac{\partial}{\partial t}\mathrm{C}(x,z,t) = \mathrm{D}\left(\frac{\partial^2}{\partial x^2}\mathrm{C}(x,z,t)\right) - \frac{6\,U x\left(1-\frac{x}{h}\right)\left(\frac{\partial}{\partial z}\mathrm{C}(x,z,t)\right)}{h}$$

$$Graetz\_adim := \frac{\partial}{\partial \tau}\Theta(\eta\sim,\zeta,\tau) = \left(\frac{\partial^2}{\partial \eta\sim^2}\Theta(\eta\sim,\zeta,\tau)\right) - 6\,\eta\sim(1-\eta\sim)\left(\frac{\partial}{\partial \zeta}\Theta(\eta\sim,\zeta,\tau)\right)$$

Using separation of Variables, the problem can be divided in three ordinary differential equations of the form:

```
> pdsolve(Graetz_adim, Theta(eta,zeta,tau));
```

Which we rewrite, using the separation variables -lambda^2 and -kappa^2

```
> eq_tau:= diff(T(tau),tau)+kappa^2*T(tau);
> eq_zeta:= diff(Z(zeta),zeta)+lambda^2/6*Z(zeta);
> eq_eta:= diff(H(eta),eta$2)+lambda^2*eta*(1-eta)*H(eta);
```

$$(\Theta(\eta\sim,\zeta,\tau) = \_F1(\eta\sim)\,\_F2(\zeta)\,\_F3(\tau))\ \&\mathrm{where}\left[\left\{\frac{d}{d\zeta}\_F2(\zeta) = \_c_2\,\_F2(\zeta), \frac{d}{d\tau}\_F3(\tau) = \_c_3\,\_F3(\tau),\right.\right.$$

$$\left.\left.\frac{d^2}{d\eta\sim^2}\_F1(\eta\sim) = (6\,\eta\sim\,\_F1(\eta\sim) - 6\,\eta\sim^2\,\_F1(\eta\sim))\,\_c_2 + \_F1(\eta\sim)\,\_c_3\right\}\right]$$

$$eq\_tau := \left(\frac{d}{d\tau}\mathrm{T}(\tau)\right) + \kappa^2\,\mathrm{T}(\tau)$$

$$eq\_zeta := \left(\frac{d}{d\zeta}\mathrm{Z}(\zeta)\right) + \frac{1}{6}\lambda\sim^2\,\mathrm{Z}(\zeta)$$

$$eq\_eta := \left(\frac{d^2}{d\eta\sim^2}\mathrm{H}(\eta\sim)\right) + \lambda\sim^2\,\eta\sim(1-\eta\sim)\,\mathrm{H}(\eta\sim)$$

The first two ODEs possess simple solutions:

```
> dsolve(eq_tau,T(tau)); dsolve(eq_zeta,Z(zeta));
```

$$\mathrm{T}(\tau) = \_C1\,\mathrm{e}^{(-\kappa^2\tau)}$$

$$\mathrm{Z}(\zeta) = \_C1\,\mathrm{e}^{\left(-\frac{\lambda\sim^2\zeta}{6}\right)}$$

The ode expressing the vertical concentration profile H(eta) is more complex:

```
> G_plan_diff:=diff(diff(GPl(eta),eta),eta)+eta*(1-eta)*lambda^2*GPl(eta);
```

The solution to G_plan_diff provides the problem's eigenfunctions

```
> G_plan:= dsolve(G_plan_diff): G_plan_Kum:= simplify(convert(G_plan,hypergeom));
>
>
```

$$G\_plan\_diff := \left(\frac{d^2}{d\eta\sim^2}\mathrm{GPl}(\eta\sim)\right) + \eta\sim(1-\eta\sim)\,\lambda\sim^2\,\mathrm{GPl}(\eta\sim)$$

$$G\_plan\_Kum := \mathrm{GPl}(\eta\sim) = \mathbf{e}^{\left(-\frac{\eta\sim\lambda\sim(-1+\eta\sim)}{2}\right)}\left(\_C1\ \mathrm{hypergeom}\left(\left[\frac{1}{4}-\frac{\lambda\sim}{16}\right],\left[\frac{1}{2}\right],\frac{\lambda\sim(2\,\eta\sim-1)^2}{4}\right)\right.$$
$$\left.+\,2\ \_C2\ \mathrm{hypergeom}\left(\left[\frac{3}{4}-\frac{\lambda\sim}{16}\right],\left[\frac{3}{2}\right],\frac{\lambda\sim(2\,\eta\sim-1)^2}{4}\right)\eta\sim-\_C2\ \mathrm{hypergeom}\left(\left[\frac{3}{4}-\frac{\lambda\sim}{16}\right],\left[\frac{3}{2}\right],\frac{\lambda\sim(2\,\eta\sim-1)^2}{4}\right)\right)$$

Boundary Conditions on H(η) for fully diffusion-limited problem

The general boundary conditions are:
1- No flux at the top wall

```
> diff(H(eta),eta)[eta=1]=0;
```

2- Instantaneous consumption reaction at the lower wall

```
> H(eta=0)=0;
```

$$\left(\frac{d}{d\eta\sim}\mathrm{H}(\eta\sim)\right)_{\eta\sim=1}=0$$

$$\mathrm{H}(\eta\sim=0)=0$$

This procedure applies the first boundary condition to find the form of the eigenfunctions

```
> Gp_bc1:= proc(eta_,lambda_) local C1,C2,sol; diff(op(2,G_plan_Kum),eta);
simplify(subs(eta=1,%)); C2:=solve(%,_C2); sol:=subs(_C2=C2,op(2,G_plan_Kum)); C1:=
subs(eta=0,%);  subs(lambda=lambda_,eta=eta_,simplify(sol/C1)); end proc;
```

```
Gp_bc1 := proc (eta_, lambda_)
local C1, C2, sol;
    diff(op(2, G_plan_Kum), η);
    simplify(subs(η = 1, %));
    C2 := solve(%, _C2);
    sol := subs(_C2 = C2, op(2, G_plan_Kum));
    C1 := subs(η = 0, %);
    subs(λ = lambda_, η = eta_, simplify(sol/C1))
end proc
```

The eigenfunction can be expressed using confluent hypergeometric functions or Kummer functions as:

```
> Gp_bc1(eta,lambda):
```

Maple does a poor job at simplifying the equation, so we rewrite, using M as the Kummer Function Symbol:

```
> eigenfunction:= (eta,lambda)-> exp(lambda*eta*(1-eta)/2)/2*(M(1/4-
lambda/16,1/2,lambda*(1/2-eta)^2)/M(1/4-lambda/16,1/2,lambda*(1/2)^2)-Cst(lambda)*(1-
2*eta)*M(3/4-lambda/16,3/2,lambda*(1/2-eta)^2)/M(3/4-lambda/16,3/2,lambda*(1/2)^2));
> Cst:= lambda-> ((lambda-4)*M(1/4-lambda/16,1/2,lambda*(1/2)^2)+(lambda+4)*M(-3/4-
lambda/16,1/2,lambda*(1/2)^2))/((lambda-12)*M(7/4-
lambda/16,3/2,lambda*(1/2)^2)+(lambda+4)*M(3/4-lambda/16,3/2,lambda*(1/2)^2))*(M(3/4-
lambda/16,3/2,lambda*(1/2)^2)/M(1/4-lambda/16,1/2,lambda*(1/2)^2));
```

$$eigenfunction := (\eta,\lambda)\rightarrow\frac{1}{2}\mathbf{e}^{(1/2\,\lambda\,\eta\,(1-\eta))}\left(\frac{\mathrm{M}\left(\frac{1}{4}-\frac{1}{16}\lambda,\frac{1}{2},\lambda\left(\frac{1}{2}-\eta\right)^2\right)}{\mathrm{M}\left(\frac{1}{4}-\frac{1}{16}\lambda,\frac{1}{2},\frac{1}{4}\lambda\right)}-\frac{\mathrm{Cst}(\lambda)\,(1-2\,\eta)\,\mathrm{M}\left(\frac{3}{4}-\frac{1}{16}\lambda,\frac{3}{2},\lambda\left(\frac{1}{2}-\eta\right)^2\right)}{\mathrm{M}\left(\frac{3}{4}-\frac{1}{16}\lambda,\frac{3}{2},\frac{1}{4}\lambda\right)}\right)$$

$$Cst := \lambda\rightarrow\frac{\left((\lambda-4)\,\mathrm{M}\left(\frac{1}{4}-\frac{1}{16}\lambda,\frac{1}{2},\frac{1}{4}\lambda\right)+(\lambda+4)\,\mathrm{M}\left(-\frac{3}{4}-\frac{1}{16}\lambda,\frac{1}{2},\frac{1}{4}\lambda\right)\right)\mathrm{M}\left(\frac{3}{4}-\frac{1}{16}\lambda,\frac{3}{2},\frac{1}{4}\lambda\right)}{\left((\lambda-12)\,\mathrm{M}\left(\frac{7}{4}-\frac{1}{16}\lambda,\frac{3}{2},\frac{1}{4}\lambda\right)+(\lambda+4)\,\mathrm{M}\left(\frac{3}{4}-\frac{1}{16}\lambda,\frac{3}{2},\frac{1}{4}\lambda\right)\right)\mathrm{M}\left(\frac{1}{4}-\frac{1}{16}\lambda,\frac{1}{2},\frac{1}{4}\lambda\right)}$$

Applying the second boundary condition to the eigenfunction provides the eigenvalue equation:

```
> dirichlet_1_C1:= subs(eta=0, eigenfunction(eta,lambda));
```

$$dirichlet\_1\_C1 := \frac{1}{2}\mathbf{e}^0\left(1-\frac{\left((\lambda\sim-4)\,\mathrm{M}\left(\frac{1}{4}-\frac{\lambda\sim}{16},\frac{1}{2},\frac{\lambda\sim}{4}\right)+(\lambda\sim+4)\,\mathrm{M}\left(-\frac{3}{4}-\frac{\lambda\sim}{16},\frac{1}{2},\frac{\lambda\sim}{4}\right)\right)\mathrm{M}\left(\frac{3}{4}-\frac{\lambda\sim}{16},\frac{3}{2},\frac{\lambda\sim}{4}\right)}{\left((\lambda\sim-12)\,\mathrm{M}\left(\frac{7}{4}-\frac{\lambda\sim}{16},\frac{3}{2},\frac{\lambda\sim}{4}\right)+(\lambda\sim+4)\,\mathrm{M}\left(\frac{3}{4}-\frac{\lambda\sim}{16},\frac{3}{2},\frac{\lambda\sim}{4}\right)\right)\mathrm{M}\left(\frac{1}{4}-\frac{\lambda\sim}{16},\frac{1}{2},\frac{\lambda\sim}{4}\right)}\right)$$

Solving For Eigenvalues

This section finds the first n eigenvalues of the expansion

```
> eigen_f:= lambda_-> exp(-
lambda/4)*numer(simplify(subs(lambda=lambda_,dirichlet_1_C1)));
```

$$eigen\_f := lambda\_ \rightarrow e^{\left(-\frac{\lambda}{4}\right)} \mathrm{numer}(\mathrm{simplify}(\mathrm{subs}(\lambda = lambda\_, dirichlet\_1\_C1)))$$

The zeros of this plot correspond to the eigenvalues of the problem. They can be roughly located and then precisely calculated using built-in Maple function solver "fsolve"

```
> plot(eigen_f(lambda),lambda=0..100);
```

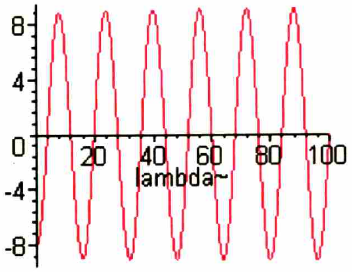

first eigenvalues:

```
> eig_1:= fsolve(eigen_f(lambda),lambda=3.5);
evalf([seq(fsolve(eigen_f(lambda),lambda=6.6+16*k),k=0..4)]);
```

$$eig\_1 := 3.81866604154175$$

$$[3.81866604154175 , 19.9241377002544 , 35.9473172831151 , 51.9582841340956 , 67.9648784118355]$$

Sherwood number

This Sh is normalized on a per surface basis and compared with the value found in Shah and London.

```
> 'Sh[infinity]=1/6*lambda[1]^2'= 1/6*eig_1^2; Shah:= 2.43037;
```

$$\left(Sh_{\infty} = \frac{1}{6}\lambda_1^{\,2}\right) = 2.43036838947068$$

$$Shah := 2.43037$$

Partially Diffusion-Limited Surface reaction

To include the effect of partial reaction limitations at the surface due to finite Damkohlers, we use the same reasoning. The eigenfunctions remain identical, but we modify the boundary condition that yields the eigenvalue equations.

THIS IS THE MASTER DAMKOHLER NUMBER FOR WHICH THE SOLUTION IS COMPUTED BELOW. Changing the value of this Global Variable will modify the calculations for the entire page.

```
> Da_M:=1;
```

THIS IS THE NUMBER OF TERMS TAKEN INTO ACCOUNT

```
> nb_max:=8;
```

As above, the eigenfunctions read:

```
> eigenfunction(eta,lambda);
```

$$Da\_M := 1$$

$$nb\_max := 8$$

$$\frac{1}{2} e^{\left(\frac{\lambda\sim\eta\sim(1-\eta\sim)}{2}\right)} \left(\frac{\mathrm{M}\left(\frac{1}{4}-\frac{\lambda\sim}{16}, \frac{1}{2}, \lambda\sim\left(\frac{1}{2}-\eta\sim\right)^2\right)}{\mathrm{M}\left(\frac{1}{4}-\frac{\lambda\sim}{16}, \frac{1}{2}, \frac{\lambda\sim}{4}\right)} - \frac{\left((\lambda\sim-4)\,\mathrm{M}\left(\frac{1}{4}-\frac{\lambda\sim}{16}, \frac{1}{2}, \frac{\lambda\sim}{4}\right) + (\lambda\sim+4)\,\mathrm{M}\left(-\frac{3}{4}-\frac{\lambda\sim}{16}, \frac{1}{2}, \frac{\lambda\sim}{4}\right)\right)(1-2\,\eta\sim)\,\mathrm{M}\left(\frac{3}{4}-\frac{\lambda\sim}{16}, \frac{3}{2}, \lambda\sim\left(\frac{1}{2}-\eta\sim\right)^2\right)}{\left((\lambda\sim-12)\,\mathrm{M}\left(\frac{7}{4}-\frac{\lambda\sim}{16}, \frac{3}{2}, \frac{\lambda\sim}{4}\right) + (\lambda\sim+4)\,\mathrm{M}\left(\frac{3}{4}-\frac{\lambda\sim}{16}, \frac{3}{2}, \frac{\lambda\sim}{4}\right)\right)\mathrm{M}\left(\frac{1}{4}-\frac{\lambda\sim}{16}, \frac{1}{2}, \frac{\lambda\sim}{4}\right)} \right)$$

The second boundary condition now becomes a boundary condition of the third kind (Robin Boundary Condition)

```
> Robin_BC:= -diff(H(eta),eta)+Da*H(eta)=0;
```

Computes the new eigenvalue equation, now dependent on two variables: lambda and Da

```
> eigen_robin:= proc(lambda,Da) local dif; diff(eigenfunction(eta,lambda),eta); dif:=
subs(eta=0,%); dif-Da*eigenfunction(0,lambda); exp(-lambda/4)*numer(simplify(%)); end
proc;
```

$$Robin\_BC := -\left(\frac{d}{d\eta\sim} \mathrm{H}(\eta\sim)\right) + Da\, \mathrm{H}(\eta\sim) = 0$$

```
eigen_robin := proc (λ, Da)                end proc
local dif;
     diff( eigenfunction( η, λ ), η );
     dif := subs( η = 0, % );
     dif – Da×eigenfunction( 0, λ );
     exp( –1/4×λ )×numer( simplify( % ) )
```

From the second boundary condition involving Da, we extract the Eigenvalue equation: Eigen_robin(lambda,Da)

```
> eigen_robin(lambda,Da):
plot(eigen_robin(lambda,Da_M),lambda=0..50,title='zeros_of_the_eigenvalue_function');
```

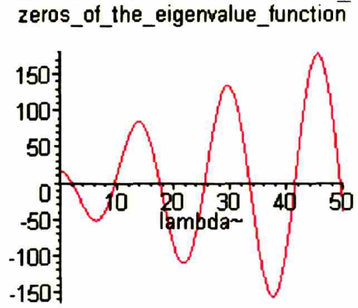

This section determines the first nb_max eigenvalues. NOTE: The algorithm to extract the roots does not always work, so verify that all eigenvalues returned are different and ordered. Consult the plot above to be more sure.

```
> lambda_set:=evalf([seq(fsolve(eigen_robin(lambda,Da_M),lambda=
3*(Da_M+0.01)/(1+Da_M)+8*(k-1)),k=1..nb_max)]);
>
lambda_set := [2.08370936349027 , 9.67057458266985 , 17.5722960288822 , 25.5244311762319 , 33.4951883718695 ,
     41.4751291717432 , 49.4603556151630 , 57.4489365660124 ]
```

We define here an inner product used to compute the coefficients of the eigenfunction expansion

```
> inner_prod:= proc(f,lambda,Da) int(eta*(1-eta)*eigenfunction(eta,lambda)*f,eta=0..1);
evalf(%); end proc;
inner_prod := proc (f, λ, Da) int( η×( 1 – η )×eigenfunction( η, λ )×f, η = 0 .. 1 ); evalf( % ) end proc
```

This is an example of the use of the inner product to calculate the value of the first eigenfunction against itself

```
> inner_prod(eigenfunction(eta,lambda_set[1]),lambda_set[1],Da_M);
                                  0.05055550675938755
```

This computes the norm of the first nb_max eigenfunctions. <Gk|Gk>=normk. NOTE: 1/sqrt(norm)= normalization coefficient of the eigenfunctions such that <Gknorm|Gknorm>=1

Computationnally intensive (~15 s per term)

```
>
norm_set:=[seq(inner_prod(subs(lambda=lambda_set[k],eigenfunction(eta,lambda)),lambda_
set[k],Da_M),k=1..5)];
norm_set :=
     [0.05055550675938755 , 3.51447474265826 , 0.0170860343982727 , 8.86169471352404 , 0.0133972245553723 ]
```

This procedure computes the first coefficients of the eigenfunction such that F(eta, zeta=0)= sum(ai*Gi(eta)). It is done for the initial condition f(eta,zeta=0)=1.

This step is computationnally intensive (~15 seconds per term)

```
> a_coeff_set:=
[seq(inner_prod(1,lambda_set[k],Da_M)/inner_prod(eigenfunction(eta,lambda_set[k]),lamb
da_set[k],Da_M),k=1..5)];
```

a_coeff_set := [1.80850349503230 , -0.0177919561047078 , 0.0897772414543372 , -0.00203146483027679 , 0.0321345285764554]

The full solution thus writes:

```
> Theta(eta,zeta,tau)= Sum(a[n]*'eigenfunction(eta,lambda[n])'*exp(-
lambda[n]^2/6*zeta)*(1-exp(-kappa^2*tau)),n=1..infinity);
```

$$\Theta(\eta\sim, \zeta, \tau) = \sum_{n=1}^{\infty} a_n \, \mathrm{eigenfunction}(\eta, \lambda_n) \, \mathrm{e}^{\left(-1/6 \, \lambda\sim_n^2 \, \zeta\right)} (1 - \mathrm{e}^{(-\kappa^2 \tau)})$$

The value of kappa is not calculated here because the Graetz problem assumes time steady state. We put it for completion, but the steady state assumption proved to be satisfied (pseudo-steady state) for our particular problem. Also, from an engineering point of view, it is not important to know the concentration distribution in the eta direction. A more compact solution to be used is found using velocity-averaged coefficients:

```
> Theta[b](zeta)= Sum(A[n]*exp(-1/6*lambda[n]^2),n=1..infinity);
```

with coefficients A:

```
> A_coeff_set:=
[seq(6*inner_prod(1,lambda_set[k],Da_M)^2/inner_prod(subs(lambda=lambda_set[k],eigenfu
nction(eta,lambda)),lambda_set[k],1e12),k=1..5)];
```

$$\Theta_b(\zeta) = \sum_{n=1}^{\infty} A_n \, \mathrm{e}^{\left(-1/6 \, \lambda\sim_n^2\right)}$$

A_coeff_set := [0.992098174621656 , 0.00667511994291540 , 0.000826275813763026 , 0.000219425274764092 , 0.0000830060893074228]

The sum of the coefficients at the origin (zeta=0) should give 1:

```
> test_sum:=sum(A_coeff_set[i],i=1..5);
```

test_sum := 0.999902001742405

Sherwood number

This section computes the Sherwood number for the fully developed region including the effect of reaction limit at the wall. It also computes the diffusion/reaction mass transfer coefficient kd/r found in the Chem. Eng. Sci. Paper (Gervais et. al, 2005).

```
> eig_Da_1:= proc(Da) fsolve(eigen_robin(lambda,Da),lambda= 6.6*(Da+0.01)/(1+Da)); end
proc;
> eig_Da_1(Da_M);
> 'D/h*(1/k[m]+1/k[r])=(1/(3/(lambda[1](Da))^2+1/Da))'=
(1/(12/eig_Da_1(Da_M)^2+1/Da_M));
> k[dr]:= 'lambda^2/6'=eig_Da_1(Da_M)^2/6;
```

eig_Da_1 := **proc** (*Da*) fsolve(eigen_robin(λ, *Da*), $\lambda = 6.6\times(Da + 0.01)/(Da + 1)$) **end proc**

2.08370936349027

$$\left(\frac{\mathrm{D}\left(\frac{1}{k_m} + \frac{1}{k_r}\right)}{h} = \frac{1}{\frac{3}{\lambda_1(Da)^2} + \frac{1}{Da}} \right) = 0.265688775542115$$

$$k_{dr} := \frac{\lambda^2}{6} = 0.723640785249505$$

This section computes the diffusion reaction mass transfer coefficient kdr for various Damkohler numbers.

```
> kdr:= Da-> eig_Da_1(Da)^2/6;
> seq_Sh:=[seq([m/10,kdr(m/10)],m=0..20)]:
```

With the upper limit being:

```
> kdr(1e20);
```

$$kdr := Da \to \frac{1}{6} \mathrm{eig\_Da\_1}(Da)^2$$

2.43036838947068

A vector is built containing the value of kdr at various Da numbers:

```
> mmax:=30; seq_m:=[seq(m,m=1..mmax)]: seq_lambda:=[seq(eig_Da_1(-m*4/mmax^2+m^2*2/mmax
),m=0..mmax)]: seq_plot_lambda:= [seq([-m*4/mmax^2+m^2*2/mmax,eig_Da_1(-
m*4/mmax^2+m^2*2/mmax )],m=0..mmax)]:
```

$$mmax := 30$$

The vector values are plotted

```
> # kdr vs Da
> plot(seq_plot_lambda);
```

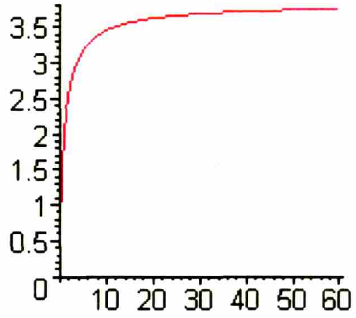

END of Code.

A2. Modeling Convection/Diffusion/Reaction transport under arbitrary conditions using FEMLAB™

In this section, we provide a step by step guide on how to simulate time-dependent concentration profile in the presence of convection, diffusion and bimolecular surface reaction under arbitrary conditions. The simulations use the multiphysics capabilities built in the FEMLAB software and uses geometry coupling to link the reaction occurring at the surface to the reaction in the bulk. The specific example used was used to generate the data used in the analysis performed in Chapter 2. In particular, refer to figure 2.6 and 2.7 for the physical understanding). This tutorial will work on FEMLAB versions 3.0 and 3.1. It will not work on earlier versions and cannot be guaranteed to work on more advanced versions of the software.

A2.1. Physics Model

The physical model solves the dimensionless equations system summarized in Table 2.1 (right column) for the case of asymmetric reactions with the data from Table 2.2 (entry 2). The convection-diffusion PDE in the bulk is couple to the bimolecular surface reaction ODE though a flux boundary condition at the reacting walls. The resulting system is nonlinear due to the multiplied surface and bulk concentration in the surface reaction equation.

A2.2. Channel geometry

To simulate transport and reaction at a channel surface one must define two different geometries in FEMLAB: a bulk geometry and a surface one. Since in most sensors studied in this work, the channel width is much larger than its height, we proceed to a simplified 2D model assuming parallel plate geometry. The resulting geometries in FEMLAB are thus very simple:

In FEMLAB 3.1, do:

1- Open "Multiphysics/Model Navigator";
2- Remove all existing geometries using the remove button;
3- Click on "Add geometry". Add a 2D geometry named "Bulk" with independent variables zeta and eta (in that order to yield a zeta normalized axial variable and eta normalized height variable);
4- Click on "Add geometry". Add a 1D geometry named "Surface" with independent variable zeta;
5- Click "OK" to close window;
6- Select the "Bulk" in the geometry tabs (Fig. A3.1);
7- Go to "Draw\Draw Objects\Rectangle-Square". Draw a rectangle whose lower left base point is located at the origin (0,0) of dimension 10x1 (Fig. A3.1). The channel we seek to model has normalized height $eta=x/h$ from 0 to 1 and length zeta= Dz/Uh^2 from 0 to 10. (x and z are the real device dimensions.) We use the scaling factor a_1 to reduce the computational cost of the simulation. In 1:1 units, modeling a 1 µm-thick and 2 mm long channel would mean a 1x2000 grid with unnecessary resolution. Thus we fix the aspect ratio of our simulations and adjust the length scale instead;
8- Similarly, select the 1D "Surface" geometry tab and draw a 10 unit-long line in 4 segments of 3.5, 3, 3, and 3.5 units respectively. The first segment split is positioned at the relative starting point of the cantilever in the channel (0.7mm/2mm =3.5/10). The second segments represents the first half of the path inside the cantilever (see Fig. 3.3). The third segments represents the second half of the channel path inside the cantilever. Finally, the last segments represents the remainder of the channel to the outlet. These segment splits will be useful when using the model to compute frequency shifts in appendix A3). This is the corresponding surface domain;

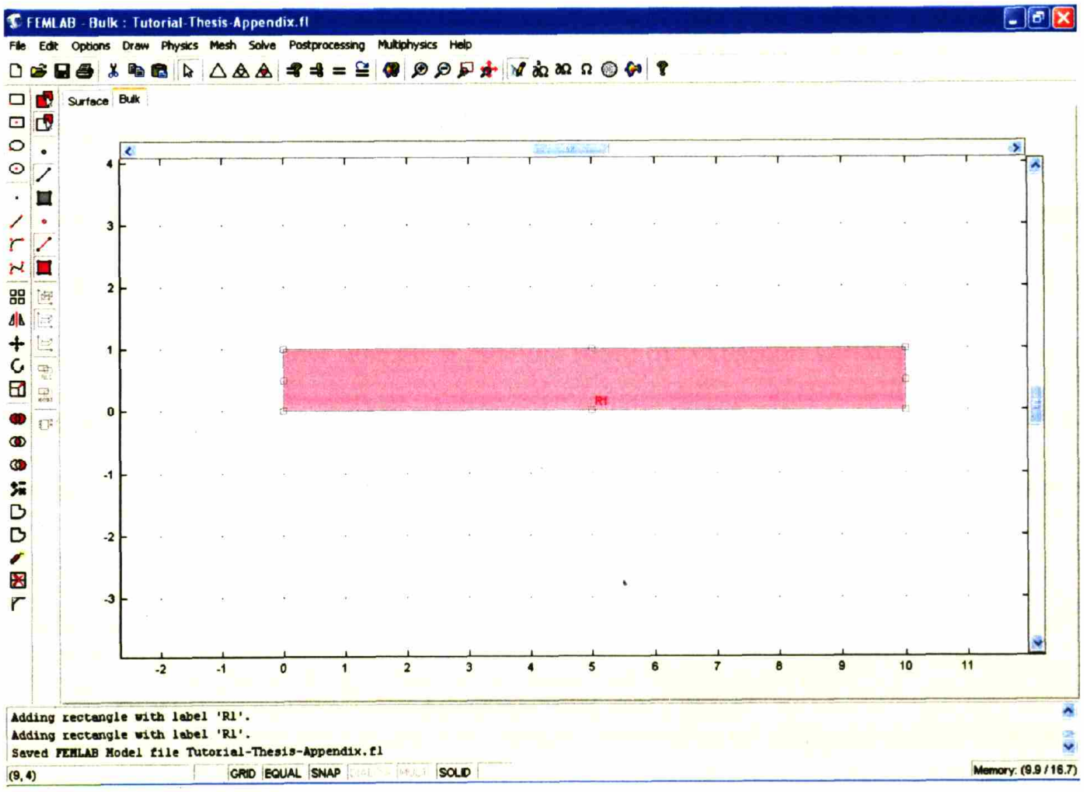

```
Adding rectangle with label 'R1'.
Adding rectangle with label 'R1'.
Saved FEMLAB Model file Tutorial-Thesis-Appendix.fl
```

Figure A2.1: FEMLAB 3.1 main interface. The Geometry tabs are right above the drawing region. The drawing tools are located on the right. The simple geometry drawn is the side view of a parallel plate channel 10 times longer than high.

A2.3. Physics Model Setting and Domain Coupling

Once the two geometries are drawn, the type of physics model must be selected from FEMLAB's Chemical Engineering Module. Then extrusion variables must be specified to link the two geometries together. Finally, the subdomain equations and boundary conditions must be specified with user-defined experimental parameters.

Choosing the physics models:

9- In "Multiphysics\Model Navigator", select for the 2D geometry "Chemical Engineering Module\ Mass Balance\ Convection and Diffusion\ Transient Analysis". Rename the dependent variable "Theta" for the normalized concentration variable and click "Add";

10- Similarly create another transient convection-diffusion module in the 2D geometry with dependent variable "Theta_b" for the velocity-averaged normalized bulk concentration (see chapter 2);

11- In the 1D geometry, create a transient diffusion module (convection is not necessary at the surface) with dependent variable "Theta_s" for the normalized surface concentration;

12- Click "OK" and return to FEMLAB's main window;

Domain Coupling:

A priori, variables are only defined with respect to the geometry in which they operate. Coupling two domains together so that the change of one dependent variable in a domain affects the change of another in another domain is possible using the extrusion variable feature. To do so, the variable "Theta_s" in the 1D geometry must be redefined in the 2D domain with a different name. Similarly the variable "Theta" must be redefined in the 1D domain to represent the concentration at the wall. The procedure is the following:

13- While in the "Bulk" Geometry, select "Options\ Extrusion Coupling Variables\ Boundary Variables" to bring up the extrusion variables window;

14- On the boundaries corresponding to the upper and lower wall enter the following:
  a. On the lower wall (#2), create the variable Theta_wall = Theta,
  b. Under the destination tab, select the "surface" geometry as the destination and the boundary #2 and #3 as the origin,
  c. Under the source vertices tab, enter the starting and ending point of the boundary to be extruded (vertices # 1 and 3),
  d. Under the destination vertices tab, enter the starting and ending point of the domain to which it corresponds in the 1D geometry (vertices # 1 and 5).

15- Repeat step 14 in the "Surface" geometry and create another extrusion variable Theta_s_up =Theta_s which links the surface concentration in all of the 1D domain to the upper boundary in the 2D domain;

16- Repeat once more to add another variable Theta_s_down =Theta_s and link it to the lower boundary in the 2D domain;

Even though "Theta_s_up" and "Theta_s_down" represent the same variable, they must be speficied individually since every extrusion variable can possess only one destination. Furthermore, should the problem be generalized to account for different reaction rates at both walls, it is more convenient to have the two walls represented with different variables.

Constant and Variable Specifications

17- In "Options\constants" enter the problems experimental parameters, one per line, within a consistent unit system. The constants entered are global:
   a. Initial bulk concentration of analyte: c0=1e-7 [M],
   b. Total number of surface receptors (bBSA binding sites): cs0=7e-8 [M·mm],
   c. Number of walls participating in the reaction: nw=2 [s.u.] (this value can be 1 or 2),
   d. Diffusivity of the analyte (Streptavidin): D=6e-5 [mm^2/s],
   e. Channel height: he=0.001 [mm],
   f. Channel length: L=2 [mm],
   g. Length of the geometry: L_geom=10 [s.u.],
   h. Association rate constant (A33 protein with anti-A33 IgG): kon=2.4e5 [$M^{-1}s^{-1}$],
   i. Dissociation rate constant (same reaction): koff=0 [s^{-1}],
   j. Average fluidic velocity: U=2 [mm/s].

Even though the dissociation constant of Biotin-Streptavidin binding is essentially 0, we define all reaction with the dissociation term so that the model can be directly used with arbitrary dissociation constants.

18- In the "Bulk" geometry tab, select "Options\Scalar Variables". Enter the variables that apply to the bulk and the surface. The variables entered are local to one particular geometry:
   a. Normalized Poiseuille velocity profile: V=6*x*(1-x),
   b. Peclet Number: Pe=U*he/D,
   c. Damköhler number: Da=kon*cs0*he/D,
   d. Diffusion time scale: td= he^2/D
   e. Normalized dissociation constant: KD= koff/kon/c0,
   f. Relative surface capacity: epsilon= c0*he/cs0,
   g. Length scaling factor: a1 = L_geom*td*U/L, this factor dilates the geometry such that the true sensor length traveled at zeta=10 is the length of the sensor L.
   h. Effective front velocity: Ueff=U*(1+nw*cs0/c0/h/(1+KD)),
   i. Normalized bimolecular reaction term at the upper wall:
      reac_wall_up=epsilon*Da*(Theta* (1-Theta_s_up)-KD*Theta_s_up),
   j. Bimolecular reaction term at the upper wall:
      reac_wall_down=epsilon*Da*(Theta* (1-Theta_s_down)-KD*Theta_s_down),

19- In the "Surface" geometry tab, select "Options\Subdomain Variables":
   a. Enter the surface reaction rate as seen from the surface:
      reac_s=epsilon*Da*(Theta_wall* (1-Theta_s)-KD*Theta_s).

Subdomain equation settings:

20- In "Multiphysics\Model Navigator", select the concentration model with variable "Theta". In "Physics\ subdomain settings" enter the following parameter (linked to the variables previously defined) in the convection-diffusion equation ("Theta" tab):
   a. Time-scaling coefficient: δts= td (since τ = t/td)
   b. Diffusion coefficient: D anisotropic = (a1/Pe)^2 0 0 1 (Since the normalization constants are different axially and vertically, the effective diffusion in the geometry becomes anisotropic),
   c. Reaction rate : R= 0 (there is no reaction in the subdomain)
   d. z-velocity: u= a1*V (accounts for the normalized length)
   e. leave the "init" and "element" tab unchanged,

21- In "Multiphysics\Model Navigator", select the concentration model with variable "Theta_b". In "Physics\ subdomain settings" enter the following:
   a. Diffusion coefficient: D isotropic = 0,
   b. Reaction rate : R= Theta*V,
   c. x-velocity: u=1,
   d. leave the other tabs unchanged.

Looking carefully at the equations, step 20 is specified such that the value of "Theta_b" becomes the integral of the concentration times the velocity profile, thus yielding the velocity-averaged concentration profile in the bulk $\Theta_b(z)$.

22- In "Multiphysics\Model Navigator", select the concentration model with variable "Theta_s". In "Physics\ subdomain settings" enter the following:
   a. Time-scaling coefficient: δts= td (since τ = t/td)
   b. Diffusion coefficient: D isotropic = 0,
   c. Reaction rate : R= reac_s,
   d. leave the other tabs unchanged.

With the diffusion coefficient at the surface set to 0, the model computes the time dependent bimolecular reaction rate at the surface. This rate will vary with z depending on the concentration Theta_wall right above it in the bulk.

Boundary conditions settings:

23- For each of the models (variables Theta, Theta_b and Theta_s) enter the boundary conditions in "Physics\boundary settings":
   a. for the "Theta" variable:
      i. boundary 1 (inlet): concentration c0= 1,
      ii. boundary 2 (lower wall): flux = -reac_wall_down/epsilon,
      iii. boundary 3 (upper wall): flux= -reac_wall_up/epsilon,
      iv. boundary 4 (outlet): convective flux.

For an asymmetric reaction, set the upper wall flux to 0 instead.

b. for the "Theta_b" variable:
  i. boundary 1 (inlet): insulation/symmetry,
  ii. boundary 2 (lower wall): concentration c0=0 (initial condition for the integral),
  iii. boundary 3 (upper wall): convective flux,
  iv. boundary 4 (outlet): insulation/symmetry,
c. for the "Theta_s" variable:
  i. boundary 1 (left vertex): flux=0,
  ii. boundary 3 (right vertex): flux=0.

A2.4. Meshing

The meshing of the geometry must be fine enough to resolve the sharp spatial distribution of analytes that may occur near the reacting walls. In the bulk, some memory can be saved by specifying a coarser mesh since the gradients present there are lower than at the surface. We therefore propose the following meshing method:

24- Select "Mesh\Mesh parameters" from the main menu to bring up the customized mesh window. For the "Bulk" geometry, enter the following:
  a. In the subdomain tab, enter a maximum element size of 0.2. This size limits ensures that, for a geometry of height 1 as in the present case, there will always be at least 5 grid points across it,
  b. In the boundary tab, enter a maximum element size of 0.05 along the reactive walls (boundaries 2 and 3) to ensure a finer characterization of these regions,
  c. Click on remesh to recreate the mesh. The default mesh growth rates are sufficient in our case.
25- Select the "Surface" geometry and select Mesh\Mesh parameters" from the main menu;
  a. In the subdomain tab, enter a maximum element size of 0.05. This number of points at the surface will be sufficient to match those specified at the boundary in the "Bulk" geometry.

A2.5. Solver Parameters and Solver Manager

The solver parameter and solver manager windows, in the "solve" menu are necessary to specify the type of solving algorithm used, the number of time points to compute and which variables to solve for. Prior to setting these parameters, a quick scaling of the problem provides the appropriate time range to be specified. The diffusion, convection and reaction time scales in this problem yield: $\bar{t}_c = L/U$=1s, $\bar{t}_d = he^2/D$=0.02s, $\bar{t}_r = he/k_{on}C_{s0}$=0.12s. The convection time scale is clearly the largest which means that transport should occur from the inlet to the outlet at effective velocity U_{eff}, and therefore the saturation of the whole channel's surface receptors should occur on a time scale of $\bar{t}_s \sim L/U_{eff} = L/U \cdot \left(1 + n_w C_{s0}/he/(C_0 + K_D)\right)$~1400s if the two surface are participating (n_w=2).

Solver Parameters:

26- In "solver\solver parameters", select the "general" tab and specify the following:
   a. Time stepping: times= 0:100:1500, a time larger than the predicted 1400 seconds to capture the full saturation time scale with time increments of 100s each (middle value),
   b. Direct Solver: UMFPACK. Given the relatively small size of the model (18000 degrees of freedom), direct solving is the most convenient numerical method,
   c. Solution form: select "General" or "Weak". "Coefficients" is too rigid for such highly coupled problem,
   d. Other tabs can be left as they are for now,
   e. Click "Ok" to return to the main window.

Solver Manager:

27- In the "solver\solver manager" window,
   a. select the "initial value" tab and specify: Initial value: "Initial value expression", the rest can be left untouched,
   b. In the "solve for" and "output" tabs, values can be left as default (i.e. solves for all variables). In some particular cases, it may save time to solve only for certain variables. However, all coupled variables must always be solved together or the solution will yield a trivial solution,
   c. Click "OK" to return to the main menu.

Solving the problem:

Solving the problem can be done by simply clicking on the "equal" in the toolbar icons. Alternatively, it can be done by going to "solver\solver manager" and clicking solve in that window. The solution here takes about 2 minutes to compute on a Pentium 4, 3GHz processor speed and 2Gb RAM (you surely have better than that at hand as you read these lines…).

A2.6. Data Postprocessing

The simulations results can be handled in many ways using FEMLABs postprocessing mode. A few of the most useful ones are succinctly described here.

Plot parameters:

Selecting from the main menu "Postprocessing\plot parameters" brings forth the postprocessing window. In the "surface" tab, all dependent variables, including their derivatives are available to display in the main window. To plot a customized formula including multiple dependent variables and constants from that geometry (e.g. c0*Theta +c0*Theta_b) enter the formula in the "expression" box. Isotherm lines can be added in the "contour" tab. The "animate" tab allows to create and to save movie files by using the multiple time data series produced.

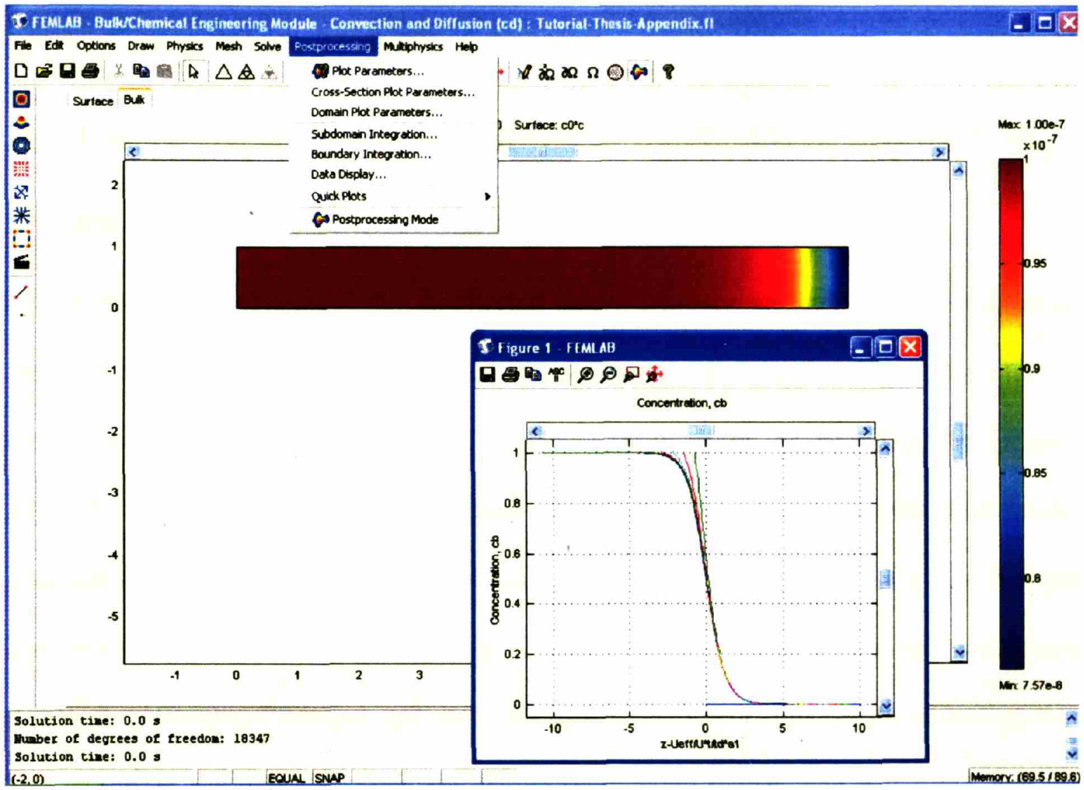

```
Solution time: 0.0 s
Number of degrees of freedom: 18347
Solution time: 0.0 s
```

Figure A2.2: Main FEMLAB window in postprocessing mode. The solution exhibited is the one calculated for t=1500s. A figure containing Cross-section plot data is exhibited.

Plotting multiple time curves simultaneously:

It may be useful to plot several times curves in the same plot window and to extract the data produced to another software to create figures such as Fig. 2.6C. The procedure is the following:

28- Select in the menu "postprocessing\cross section plot parameters";
  a. In the "line\extrusion" tab select the variable "Theta_b" to display,
  b. In the "cross section line data" box, type zeta0=0, zeta1=10, eta0=1, eta1=1,
  c. Select zeta as the x-axis data, and click apply.

To confirm that the wave propagates at constant velocity across the sensor length, it is convenient to plot all lines with a spatial shift proportional to $\Delta z = U_{eff}\Delta t$, such as in Fig. 2.6C'. This shift can be implemented using the variable transformation $\zeta' = \zeta - U_{eff}/U \cdot t/t_d$.

29- In the "x-axis data" box, activate the expression button. Enter the expression zeta-a1*Ueff/U*t/td and click "OK".

The data (Fig. A2.2) can be exported by clicking on the "ASC=" icon in the figure and later processed using Igor pro, Excel, etc.

A3. Use of Integration Variables in FEMLAB to Model Frequency Output Signals in Resonators

As derived in chapter 4 for suspended microresonator sensors, the determination of the frequency output signal submitted to non-uniform loads requires the computation of the displacement-weighed average of the surface concentration, as described in section 4.5. In appendix A2, we constructed a model in FEMLAB to calculate the bulk and surface concentrations inside a straight channel. Using FEMLAB's integration variables, it is possible to conveniently build over the previous model an extension to the model that will compute the displacement-average integral and yield the cantilever output directly. In doing so, we make a few important assumptions. First, the cantilever is much longer than it is wide, and the fluidic path inside can be approximated as a straight line with a sharp U-turn at the cantilever extremity (Fig. 4.5). Therefore, from zeta=0 to zeta=5 in appendix A2, the fluid goes from the base to the tip of the cantilever. From zeta=5 to zeta=10, the fluid returns from the tip to the outlet of the device. Secondly, the lateral position of the concentration on the cantilever (width-wise) is irrelevant to compute the signal. This assumption states that a half filled channel (from the base to the tip but not back) would yield exactly half the signal of a fully filled channel as the lateral vibration modes are do not resonate at the driving frequencies used. Finally, the fluidic channel inside the resonator is wide enough that parallel plate geometry can be assumed. For most devices, the channel's aspect ratio is 20:1, which means that the effective hydraulic resistance pf the channel differs from the parallel plate case by only 3% [90]. The change in flow profile at the tip due to the turn is also neglected in first approximation to keep the model bidimensional.

A3.1. Specifying the cantilever deflection profile

Implementing the code for measuring the output frequency in FEMLAB 3.1 is performed using the following protocol. As a prerequisite to this appendix, the model in appendix A2 must be constructed and solved.

1- In the "Surface" geometry, select "option\constants" and add the following constants to the existing ones:
   a. Cantilever length in real units: Lc = 0.3 [mm],
   b. Length of the cantilever in model units: Lc_geom = 3 [s.u],
   c. Position at the base of the cantilever: zeta_base=3.5 [s.u],
   d. Sensitivity parameter: gamma = 1 (normalized to 1 here for convenience).

2- In the "Surface" geometry, select "option\expressions\scalar expression" and add the following variables to the existing ones:
   e. Lever deflection profile from inlet to tip (eq. 4.18):
      x_zeta_in_tip = 1/2*((cosh(1.875*zeta/Lc_simul)-cos(1.875*zeta/Lc_simul))-0.7341*(sinh(1.875*zeta/Lc_simul)-sin(1.875*zeta/Lc_simul)))),
      a. Lever deflection profile from tip to outlet:
      x_zeta_tip_out = 1/2*((cosh(1.875*(2-(zeta-zeta_base)/Lc_geom))-cos(1.875*(2-(zeta-zeta_base)/Lc_geom))-0.7341*(sinh(1.875*(2-(zeta-zeta_base)/Lc_geom))-sin(1.875*(2-(zeta-zeta_base)/Lc_geom)))),
   f. Total frequency change: delta_f_tot = -gamma/2*(integral_in_tip+integral_tip_out)

A3.2. Integration Variable implementation

The variables computing the displacement-weighed average, equivalent to the total kinetic energy of the cantilever motion is conveniently defined using integration variables in FEMLAB.

3- In the "Surface geometry", select "options/ integration coupling variables/ subdomain variables".
   a. In segment 2, corresponding to the first half of the fluidic channel inside the cantilever, enter the following integration variables:
      i. First displacement-weighed integrand (eq. 4.38):
         integral_in_tip = 4*Theta_s*x_zeta_in_tip^2/2/Lc_geom,
   b. Similarly, in segment 3, enter the integration variables:
      i. Second displacement-weighed integrand (eq. 4.38):
         integral_ tip_out = 4*Theta_s*x_zeta_tip_out^2/2/Lc_geom,

A3.3. Solution and Data Visualization

When the FEMLAB solver has already provided a solution to all dependent variables specified in the integrand of the integration variables (Theta_s only in our case), then it does not need to run again to perform the integrals.

4- Using the command "solve\update model" updates all integration variable and expressions defined;

5- Once the model update is performed, select from the main menu "postprocessing/cross section plot parameters.
   a. In the "point" tab, enter the expression "delta_f_tot". Enter also any value on the domain in the coordinates box (e.g. 1). (For an integration variable, the value of the integral is independent of the surface position). Click "OK" to plot the value of the frequency output.

This type of modeling was used to produce and analyze Figs. 4.7-4.10. The results are generalizable for any kind of cantilever geometry. However, solving 3D models in FEMLAB requires special care due to the high physical memory required to run the software.

A4. Calculation of the Natural Resonance Frequency of the Suspended Microresonator Sensor

In this section, we determine the resonance frequency of the unloaded cantilever. We proceed by studying the geometry of the device (Fig. 4.3) and its material properties (see below) and by applying the theory of static bending of beams.

A4.1. Physical Assumptions

The device poses certain difficulties since the buried channels inside it yields non uniform material properties. Furthermore, the device is not entirely rectangular (Figure 4.3). However, the problem can be simplified to rectangular cantilever and yield an excellent approximation of the real device by making (and justifying) the following assumptions:

1. We assume that the fluidic channel contributes to neither the elasticity modulus nor the area moment of inertia. The shear modulus of water in an unconfined space is indeed negligible. The modulus of low stress silicon Nitride, E=180GPa, is taken from the literature[*137*].

2. The region of the cantilever which is not rectangular (the tip) is very short compared to the device's total length (25μm/315μm=8%). The region also possesses a silicon nitride volume fraction very similar to the rectangular part of the lever (75% Si_3N_4 for the trapezoidal tip and 71% for the rectangular section). For a trapezoid-shaped cantilever of tip width b and base width w, the spring constant is found by solving eq. (4.9) with a length dependent area moment of inertia

$$I(y)=\frac{wh_0^3}{12}\left(1-(1-\frac{b}{w})\frac{y}{\Delta L}\right). \tag{4.50}$$

ΔL is the length of the trapezoidal portion of the lever.

The result gives an effective spring constant of

$$k_{\text{trapezoid}}=k_{\text{rectangle}}\cdot\frac{\left(1-b/w\right)^3}{-b/w\ln\left(b/w\right)+\left(1-b/w\right)\left(\frac{3}{2}\left(1-b/w\right)-1\right)}. \tag{4.51}$$

For $b=25\mu\text{m}$ and $w=53\mu\text{m}$, we get an effective spring constant $k_{\text{trapezoid}}=0.85\cdot k_{\text{rectangle}}$. A variation of 15% on the spring constant over a region comprising 8% of the device length, even at the tip, can be neglected with no significant loss in precision.

3. A 40 nm thick chromium layer is deposited on 75% of the cantilever surface. The layer has a total mass of 4.5 ng (4% of the cantilever mass). The mass is added to the total cantilever mass as if it were uniformly distributed on the surface.

A full characterization of the device geometry is provided below. With the assumptions made above, and using eq. , we obtain a resonance frequency f_0=34 kHz. The experimentally measured range for devices, depending on where they come from on the wafer is 32-35 kHz.

A4.2. Calculations performed in MAPLE^{TM}

by Thomas Gervais, November 2004

Initialization of the worksheet:
```
> restart; Digits:=5:
```

Material properties of the hollow cantilever [Units are in g, cm, s, Hz]:

Material densities [g/cm^3]:
```
> rho[SiN]:= 3.2: rho[water]:= 1:
```
Material Young Moduli [dynes/cm^2]
```
> E[SiN]:=1.8e12: E[water]=0:
```

Cantilever Geometry:

Fluidic channel height, Top and Bottom wall thickness, Total cantilever thickness:
```
> h[channel]:= 1e-4: h[top]:=0.8e-4: h[bottom]:= 0.8e-4: h[tot]:=
h[channel]+h[top]+h[bottom]:
```
Width of the outer SiN fluidic walls, Width of the Middle SiN wall, Channel width, Total cantilever width,
```
> W[out]:=5e-4: W[mid]:=3e-4: W[channel]:=20e-4: W[tot]:= 2*W[out]+W[mid]+2*W[channel]:
```
Total cantilever length
```
> L:=315e-4:
```

Cross sectional area calculations:

Silicon Nitride Cross section area
```
> A[SiN]:=(h[top]+h[bottom])*W[tot] + h[channel]*(W[mid]+2*W[out]);
> A[channel]:=2*W[channel]*h[channel]; A[tot]:=A[SiN]+A[channel];
```

$$A_{SiN} := 0.978\ 10^{-6}$$
$$A_{channel} := 0.40\ 10^{-6}$$
$$A_{tot} := 0.1378\ 10^{-5}$$

Effective Material Properties:

The effective material properties of the cross section can, in first approximation, be assumed to be the area-weighed average of the quantities:
Average density:
```
> rho[eff]:= (rho[water]*A[channel]+rho[SiN]*A[SiN])/A[tot];
```
Area Moment of Inertia I

I for a solid cantilever (inside walls W[out] and W[mid])
```
> I_solid:= W[tot]*h[tot]^3/12;
```
I for a purely hollow cantilever (As if it were two cantilevers of thickness 0.8 um suspended 1um apart.)
```
> I_channel:= W[tot]*2*int(x^2,x=h[channel]/2..h[channel]/2+h[top]);
```
Springs added in parralel add up their spring constants (k~ I). The total width-averaged area moment of inertia becomes:

```
> I_eff:= ((2*W[out]+W[mid])*I_solid+2*W[channel]*I_channel)/W[tot];
```

$$\rho_{eff} := 2.5614$$
$$I\_solid := 0.77627\ 10^{-14}$$
$$I\_channel := 0.73212\ 10^{-14}$$
$$I\_eff := 0.74294\ 10^{-14}$$

Spring constant of the cantilever:

```
> k:= 3*E[SiN]*I_eff/L^3;
```

$$k := 1283.6$$

Total Cantilever mass:

Cantilever Mass:

```
>M[d]:= rho[eff]*A[tot]*L; #in grams
```

Mass of deposited chrome in grams (assumed uniformly distributed)

```
>m[cr]:= 4.5e-9;
```

Total mass:

```
> M[tot]:= M[d]+m[cr];
```

$$M_d := 0.11118\ 10^{-6}$$
$$m_{cr} := 0.45\ 10^{-8}$$
$$M_{tot} := 0.11568\ 10^{-6}$$

Hollow Cantilever Resonance Frequency:

First normal eigenfrequency mode:

```
>omega:= sqrt(1.875^4*k/3/M[tot]):
```

The final frequency in Hertz is:

```
>f[hollow]:= evalf(1/2/Pi*omega);
```

$$f_{hollow} := 34027.$$

Resonance Frequency of a solid cantilever (For comparison)

```
> f[solid]:= evalf(1/2/Pi*sqrt(1.875^4*E[SiN]*I_solid/(rho[SiN]*A[tot]*L+m[cr])/L^3));
```

$$f_{solid} := 31242.$$

A5. Construction of a 3D Coupled Fluid-Structure Interaction Model in CFDACE™

A5.1. Construction of a 3D Microchannel Structure in CFDGEOM

In this section we proceed to the drawing of a 25µm x 500µm x 10mm fluidic channel surrounded by a solid elastic region of 2mm x 2mm x 10mm for the study of fluid-structure interaction in elastic media. For the pressures applied (~1 atm) deformation is small enough (<50μm) that a 2mm-thick solid slab can be considered as an infinite medium. Furthermore, the physics of the problem offers a vertical symmetry plane at the very center of the fluidic channel. Therefore, only one half of the channel and of the solid block covering it needs to be modeled.

In order to fully specify the geometry in CFDGEOM, one must first draw the geometry, then construct the mesh. Finally, the different surface created must be named and their material and geometric properties defined.

This work has been performed using CFDGEOM version 2004. Some basic knowledge of CFDACE maybe required prior to following this protocol. The reader can get quickly familiarized with the software's basic operation (3-button mouse operation, viewing tools, object picking, etc.) through the CFDACE tutorials (available on-line).

The procedure yielding the meshed geometry, in its three distinct steps, is the following:

A5.1.1. Device Drawing

Far from the channel inside the solid region, displacements and strains are assumed to vanish. We can take computational advantage of that observation by creating a solid region with several compartments. The compartments closest to the channel will be assigned a finer mesh and the ones far from the deformed region a coarser one. Axially the geometry and also the mesh will be invariant.

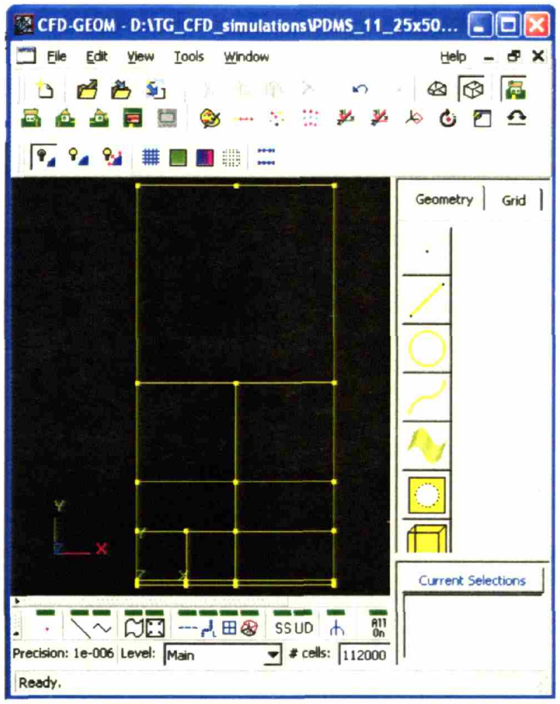

Precision: 1e-006 Level: Main # cells: 112000

Ready.

Figure A5.1: Cross section view of the device geometry in CFDGEOM. In the z-direction, the channel is simply a 10mm long extrusion of the cross-section. The fluidic channel is the bottom left rectangle. Other rectangle are modules of different mesh size.

1- Point Creation: In CFDGEOM, click on the "geometry" tab and select the "point creation options/ coordinates-screen pick". Enter the following points as the 2D vertices of the surface cross-section (the dimensions are in meters):
   a. Base line: (0,-2.5e-5,0), (2.50e-4,-2.5e-5,0), (5e-4,-25e-6,0), (0.001,-2.5e-5,0)
   b. y=0 line: (0,0,0), (2.5e-4,0,0), (5e-4,0,0), (0.001,0,0)
   c. 1st line: (0,2.5e-4,0), (2.5e-4, 2.5e-4,0), (5e-4, 2.5e-4,0), (0.001, 2.5e-4,0)
   d. 2nd line: (0, 5e-4,0), (5e-4, 5e-4,0), (0.001, 5e-4,0)
   e. 3rd line: (0,0.001,0), (5e-4, 0.001,0), (0.001, 0.001,0)
   f. 4th line: (0,0.002,0), (5e-4, 0.002,0), (0.001, 0.002,0)
2- Line Creation: In the "geometry" tab, select the "line\ create polyline" option. Link all points together through lines as in Fig. A5.1;

The basic 2D geometry is now created. For the sake of simplicity, we take advantage of CFDGEOM's drawing features to mesh the cross-section and later to extrude it to create the 3rd dimension.

A5.1.2. Mesh Generation

Contrary to the FEMLAB software, meshing in CFDGEOM has to be performed entirely manually. The user can choose between two types of meshes: structured (composed of rectangular units) or unstructured (composed of polyhedra). In CFDACE v2004, the grid deformation algorithm accepts only structured meshes and we shall therefore proceed with that option.

Edge Creation

A structured mesh is defined in CDFGEOM by first specifying the number of grid points at the edges and then by extrapolating that grid to a surface. The mesh to be constructed will be coarse and optimized for a quick solution. Finer meshes can be created later for higher resolution of the solution.

3- In the "grid" tab, select the "structured edge options\ create-edit edges". Do the following:
    a. On the channel level, select the channel's side walls and the two other lines in the solid region one by one. They are 25 μm high lines located at x-position 0, 250, 500 and 1000 μm. For each of these lines, enter a "# grid points" in the parameter tab of 9. Click apply,

4- Repeat the "create-edit edges" action with the other edges in the cross-section according to the diagram provided in Fig. A5.2;

For each edge, grid points do not have to be equidistant. For the upper edges and the one on the far side, a better matching between the cell is obtained by placing a higher concentraiton grid points on a given edge closer to the fluidic channel. This grid distribution is specified in CFDGEOM the following way:

5- For each edge to transform, select "structured edge options\ create-edit edges". In the parameter tab, enter a power law distribution with a value of 1.5. The position of the edges to modify in such a way is provided in Fig. A5.2. On the diagram, a + besides the number of grid points means a "forward" power law while a – sign implies a "backward" power law. The orientation of these edges (+ or -) may vary according to the order in which they were drawn in step 2. It is therefore easier to remember that the grid distribution must display a higher concentration of points closer to the fluidic channel;

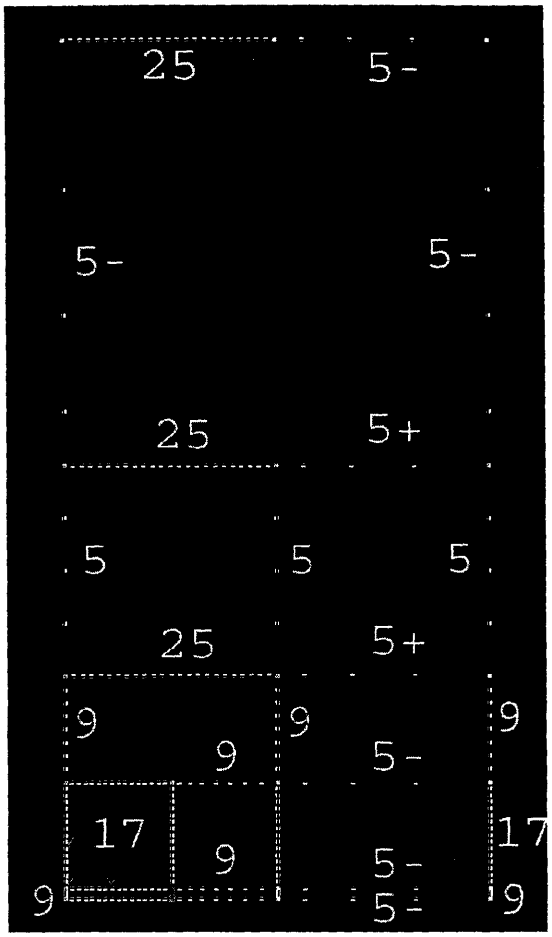

Figure A5.2: Structure of the edge grid of the mesh. The numbers indicate the number of grid point on the neighboring edge. A + sign indicates a forward 1.5 power law while the – sign indicates a backward one.

Surface specification

Once all edges are created, surfaces must be specified everywhere as the basis of the future 3D grid.

6- In the grid tab of CFDGEOM's main window, select "structured face options\ faces from edges". For each surface in the cross-section (there are 11 in total and they are all rectangular), perform the following:
   a. Pick all edges necessary to make one face of the surface. Accept the selection using the middle mouse button,
   b. Repeat for the 3 other surface edges. Once the last edge selected is accepted, a white cross appears in the surface, indicating that it is recognized as a meshed surface,
   c. Repeat for all surfaces in the cross section.

The device's cross section is now fully defined. To view the structured mesh, make sure the faces are not blanked and toggle the grid on using the icon on top of the main drawing window.

Cross-Section Extrusion

The advantage of performing the cross-section extrusion to form the channel is that the lateral edge grid points and surfaces are automatically created. Only the back side surface remains to be completed manually. The procedure is the following:

7- In the "grid" tab, select "structured face options/ face via extrusion".
    a. Select all edges created so far and accept using the middle mouse button,
    b. Enter the extrusion distance 0.01 (10 mm),
    c. Specify the number of edge grid points in "# points" to 101,
    d. Click "apply". The 3D structure is created.
8- Select now all the side edges (# points = 101) and distribute them according to a power law of 1.3 (see item 5) with the highest concentration of points towards the inlet (z=0);
9- To complete all outside surfaces of the geometry, repeat item 6 for the back surfaces of the devices;

The deformation is indeed greater closer to the inlet and an uneven distribution of grid points at z=0 is therefore desirable. At this point, all surfaces, both inner and outer, should be marked with a white cross indicating that CFDGEOM recognizes them as such (make sure to toggle off face blanking to observe them).

Volume Block Specifications

The volume blocks must now be delimited so that they can later be associated with either a fluidic or an elastic solid domain in the solver. There are 11 rectangular blocks in this geometry. Each one of them must be specified in the following way:

10- In the "grid" tab, select the "structured block options\ block from faces"
    a. In a way similar to the surface specification, select all surfaces pertaining to a block's rectangular sidewall. Accept the selection using the middle mouse button,
    b. Select all 5 other block surfaces the same way, making sure that each surface selected is adjacent to the previous one (not all orders work). Once the final surface is selected, purple lines converging the block's center appears, confirming that the block has been created,
    c. Repeat with all of the 11 blocks in this geometry.

Volume and Surface Condition Specifications

The final step in the geometry creation consists in assigning to each domain and surface geometric and material properties that will later be used in the solver. To proceed:

11- Bring up the larger toolbar under the viewing window and select the "BC/VC editor" tab;
    a. Select "Model\Volume" in the 3D geometry model tree
        i. Select the block corresponding to the fluidic channel and enter the properties: Type: "fluid", Material: "water", Name: "Channel". Click apply,
        ii. Using the ctrl key, select all 10 remaining blocks. Enter the properties: Type: "Solid", Material: "PDMS", Name: "Solid". Click apply.
    b. Select "Model\Surface" in the geometry model tree
        i. Select the channel end surface at z=0. Type: "inlet", Name: "Inflow",
        ii. Select the opposite channel end at z=10. Type: "Outlet", Name: "Outflow",
        iii. Using the ctrl key, select all other surfaces pertaining to both ends of the channel. Type: "Wall", Name: "Ends",
        iv. Select the channel bottom (at y=-2.5e-5) Type: "Wall", Name: "Channel_Bottom",
        v. Using the ctrl key, select the two surfaces adjacent to the channel bottom wall (at y=-2.5e-5). Type: "Wall", Name: "no_disp" (these walls will bear a no displacement boundary condition in the solver),
        vi. Select the channel top and right (x=2.5e-4) surfaces. Type: default, Name: "deform_upper" and "deform_side" (these surfaces will be allowed to deform in the solver),
        vii. Select all other interior surfaces in the solid. Type: "default", Name: "interfaces",
        viii. Select the channel's left surface (x=0) and all surfaces in the plane x=0 along the left side of the channel. Type: "symmetry", Name: "symm_line" (a symmetry boundary condition will be applied to that plane),
        ix. Select all surfaces pertaining to the top wall (y=0.002) and the right side wall (x=0.001). Type: "Wall", Name: "Free_disp" (these walls will be unconstrained surfaces).

The geometry construction is now finished and must be exported to CFDACE to specify the physics occurring in the system.

12- To view the number of cells in the current model, select "tools\model info". The current model consists of 11 domains totalizing 112000 rectangular 3D cells;

Saving the file

13- First save the whole structure as a geometry file (.GGD) by selecting "file\save" in the main menu;

14- Repeat the procedure to save the file as a .DTF file, containing all the information required for the solver to operate;
    a. Select "file\save as DTF".

The .DTF file can later be opened in CFDACE to continue with the specification of the fluid-structure coupling on the geometry.

A5.2. Walkthrough to build Fluid-Structure interaction models in CFDACE

Prerequisites: This walkthrough assumes that the structure is already created, meshed, with the volume and boundary conditions labeled in CFDGEOM (previous section). The model has then to be saved as a .DTF file and this file must be opened in CFDACE. This walkthrough will only be exact in CFDACE V2004.

The general procedure presented below describes how to perform fluid flow coupling to elastic deformation in the medium surrounding the channel. The algorithm in CFDACE uses a grid deformation module as described in section 5.2.5.

To achieve structural analysis such as the ones presented in Fig. 5.2 and 5.4 one needs to process the solver solution in the CFDVIEW module. Operating CFDVIEW is fairly straight forward and it will not be described here. Several tutorials, however, already exist to learn how to operate this piece of software.

A5.2.1. Step by Step Description of CFDACE Solver Programming

15- In the "PT" tab, activate "Flow", "Grid Deformation (Deform)" and "Stress";
16- Under "MO" with subtab:
    a. "Shared": Title your model (optional),
    b. "Deform": Autoremeshing scheme: Select Solid body elasticity analogy,
17- Under the "VC" tab:
    c. Under VC setting mode "property":
        i. Select the solid deformable part of the device and click group to lump them together (not to have to enter properties for each of them individually). Name your material with the same name specified in CFDGEOM (here: PDMS),
        ii. In subtab "Structure", enter the PDMS young modulus (E=7.5e5 Pascals) and the poisson ration (nu=0.4999, CFDACE does not take 0.5 as a value),
        iii. In the VC setting mode, select "liquid" for the "fluid subtype",
        iv. Select the fluid part of the device (the channel) and name your fluid with the same name as in CFDGEOM in the "material" section,
        v. In the "phys" subtab, set the density to 1 kg/m^3 such that any mass flux can be interpreted as a volumetric flow rate,

vi. In the “fluid” subtab, enter the viscosity of water (mu=0.001 Pa s),

d. Under “VC” with VC setting mode “stress”, make a group with the deformable solids.

i. Click on activate stress,

ii. In element options, select enhanced elements,

18- Under the “BC” tab, specify the BC type, the deform and stress types the following way (it is convenient to group all BCs of the same type together first):

e. For fixed boundaries which cannot move (e.g. plama sealed interfaces), select “BC type = wall”, “deform=prescribed displacement”, “stress=prescribed displacement” (leave the three directions, x,y and z checked),

f. For outer wall which are free to move, such as the side walls and the top of the device, select “BC type = wall”, “deform=prescribed displacement”, “stress=free”,

g. For solid-solid interfaces, select “BC type = interface”, “deform=prescribed, displacement”, “stress=free”,

h. For the symmetry line, select “BC type = symmetry”, “deform=prescribed displacement”, there is no option for stress,

i. For channel outside walls where the stress solution is not activated, select “BC type = wall”, “deform=prescribed displacement”, there is no option for stress,

j. For the ends of the channel (i.e. walls in the same plane as the inlet and outlet), it is sometimes more realistic to constrain the z-displacement in the device as if the channel were attached to the rest of a PDMS device. To do so, select “BC type = wall”, “deform=prescribed displacement”, “stress=prescribed displacement” (unclick the x and y direction to free them, leave the z direction clicked on). Otherwise, for freely moving end walls, select stress=free,

k. For outlet, select “flow=fixed pressure” (fixed to 0) ,“BC type = outlet”, “deform=prescribed displacement”,

l. For inlet, select “BC type = inlet”, “flow=fixed pressure” (fixed to the imposed pressure P, say 1e5 Pascals) , “deform=prescribed displacement”,

m. For Liquid-solid interfaces, select “BC type = interface”, “deform=implicit displacement”, “stress=load”, under the submenu, click on “implicit pressure”,

19- Under the “IC” tab

n. Select “Flow” and set the axial velocity W to 1e-6, just to help convergence,

20- Under the solver controller (“SC”) tab:

o. Under “iter” (iterations) enter

i. “Max iterations”: several thousands (say 4000). This will depend on the size of the mesh,

ii. “Coupling frequency iterations”: set to 100 (it has to be enough to allow significant convergence of the flow solution, but too much will slow down the general solving),

p. “Spatial”: select “Central” with a blending of 0.1,

q. “Solvers”: set the number of sweeps to 100 for velocity, 500 for pressure, 200 for grid deformation and 2000 for stress. You can modify these if you see any message in the output file saying that the solver has not reached convergence or that a variable was unable to be updated. When the problem is very large, it is recommended to set the pressure solver to AMG.

r. “Relax”: For the average problem, it can be left as is.

i. If negative volumes appear in the output (an error occurring when the cells of the mesh have large aspect ratios), the relaxation for pressure can be set to around 0.3,

ii. The grid deformation relaxation can also be lowered to 0.3. This will significantly slow down the convergence but negative volumes are less likely to appear,

s. “limits”: Were always left untouched

t. “adv”:

i. Make sure that the “maximum available memory” input is always bigger than the problem size,

ii. Under “Gd deformation” set the “BC node interpolation” to “solver”. This appears to solve most negative volumes problems,

21- In the ouput “OUT” tab

u. Under “print” click on the “mass flux summary”. You can also have access to certain integral quantities, such as area, volumetric flow or mass flux” at the interfaces by clicking the “BC Integral Output” box. If so, you need to create a .FMT file using Notepad with the same name as the .DTF file you are running and located in the same folder. If you don’t provide it, CFDSolver will give an error message and a help file on how to create such a .FMT file. The template is easy to understand. Interesting quantities to monitor are channel volume, total pressure for at walls and volumetric flow rate,

  v. Under "Graphic" select the variables you need to post process your simulation:
    i. I recommend as a minimum, Velocity vector, Static pressure, Displacement, Cartesian Stress tensor, Cartesian Strain tensor,

22- Under the "RUN" tab
  w. Click on "Submit to solver" to solve your model. Click on "output" and "View Residual" to open these windows. They are invaluable to monitor the progress of your solution and to debug it.

References

1. A. J. Tudos, G. A. J. Besselink, R. B. M. Schasfoort, Trends in miniaturized total analysis systems for point-of-care testing in clinical chemistry, *Lab on a Chip* 1, pp. 83 (2001).

2. D. R. Meldrum, M. R. Holl, Microscale bioanalytical systems, *Science* 297, pp. 1197 (Aug 16, 2002).

3. D. R. Walt, Miniature analytical methods for medical diagnostics, *Science* 308, pp. 217 (Apr 8, 2005).

4. L. Hood, J. R. Heath, M. E. Phelps, B. Y. Lin, Systems biology and new technologies enable predictive and preventative medicine, *Science* 306, pp. 640 (Oct 22, 2004).

5. H. Zhang, X. J. Li, D. B. Martin, R. Aebersold, Identification and quantification of N-linked glycoproteins using hydrazide chemistry, stable isotope labeling and mass spectrometry, *Nature Biotechnology* 21, pp. 660 (Jun, 2003).

6. H. Kitano, Systems biology: A brief overview, *Science* 295, pp. 1662 (Mar 1, 2002).

7. P. K. Sorger, A reductionist's systems biology - Opinion, *Current Opinion in Cell Biology* 17, pp. 9 (Feb, 2005).

8. K. M. Carr, K. Rosenblatt, E. F. Petricoin, L. A. Liotta, Genomic and proteomic approaches for studying human cancer: Prospects for true patient-tailored therapy, *Human Genomics* 1 (2), pp. 134 (2004).

9. A. D. Weston, L. Hood, Systems biology, proteomics, and the future of health care: Toward predictive, preventative, and personalized medicine, *Journal of Proteome Research* 3, pp. 179 (Mar-Apr, 2004).

10. H. Lodish *et al.*, *Molecular Cell Biology, 5th ed.* (WH Freeman and Co, New York, 2004), pp. 973.

11. S. Gaudet *et al.*, A compendium of signals and responses triggered by prodeath and prosurvival cytokines, *Mol Cell Proteomics* Epub (ahead of print) (2005).

12. R. S. Hotchkiss *et al.*, Rapid onset of intestinal epithelial and lymphocyte apoptotic cell death in patients with trauma and shock, *Crit. Care Med.* 28, pp. 3207 (2000).

13. K. A. Janes *et al.*, A high-throughput quantitative multiplex kinase assay for monitoring information flow in signaling networks - Application to sepsis-apoptosis, *Molecular & Cellular Proteomics* 2, pp. 463 (Jul, 2003).

14. S. Gaudet, Personal Communication, (2005).

15. J. El-Ali, S. Gaudet, A. Gunther, P. K. Sorger, K. F. Jensen, Cell stimulus and lysis in a microfluidic device with segmented gas-liquid flow, *Analytical Chemistry* 77, pp. 3629 (Jun 1, 2005).

16. B. N. Kholodenko, Hoek, J.B., Quantification of Short Term Signaling by the Epidermal Growth Factor Receptor, *J. Biol. Chem.* 274, pp. 30169 (1999).

17. K. E. Petersen, Silicon as a Mechanical Material, *Proceedings of the IEEE* 70, pp. 420 (1982).

18. A. Manz *et al.*, Design of an Open-tubular Column Liquid Chromatograph Using Silicon Chip Technology, *Sensors and Actuators B-Chemical* 1, pp. 249 (1990).

19. S. C. Terry, J. H. Jerman, J. B. Angell, A Gas Chromatographic Air Analyzer Fabricated on a Silicon Wafer, *IEEE Trans. Electron Devices* ED-26, pp. 1880 (1979).

20. A. Manz, N. Graber, H. M. Widmer, Miniaturized Total Chemical-Analysis Systems - a Novel Concept for Chemical Sensing, *Sensors and Actuators B-Chemical* 1, pp. 244 (1990).

21. A. Manz *et al.*, Micromachining of Monocrystalline Silicon and Glass for Chemical-Analysis Systems - a Look into Next Century Technology or Just a Fashionable Craze, *Trac-Trends in Analytical Chemistry* 10, pp. 144 (May, 1991).

22. K. F. Jensen, Microreaction engineering - is small better?, *Chemical Engineering Science* 56, pp. 293 (2001).

23. J. Knight, Microfluidics: Honey, I shrunk the lab, *Nature* 418, pp. 474 (Aug 1, 2002).

24. H. A. Stone, S. Kim, Microfluidics: Basic issues, applications, and challenges, *Aiche Journal* 47, pp. 1250 (Jun, 2001).

25. P. J. A. Kenis, Whitesides, G.M., Microfabrication Inside Capillaries Using Multiphase Laminar Flow Patterning, *Science* 285, pp. 83 (2 July 1999, 1999).

26. W. G. Stroock AD, Ajdari A, Patterning flows using grooved surfaces, *Anal. Chem.* 74, pp. 5306 (October 15 2002, 2002).

27. E. A. Schilling, A. E. Kamholz, P. Yager, Cell lysis and protein extraction in a microfluidic device with detection by a fluorogenic enzyme assay, *Analytical Chemistry* 74, pp. 1798 (Apr 15, 2002).

28. P. Mitchell, Microfluidics- downsizing large-scale biology, *Nature* 19, pp. 717 (August 2001, 2001).

29. D. Beebe, Physics and applications of Microfluidics in biology, *Annu. Rev. Biomed. Eng.* 4, pp. 261 (2002).

30. Y. Xia, Whitesides, G.M., Soft Lithography, *Annu. REv. Mater. Sci.* 28, pp. 153 (1998).

31. G. M. Whitesides, Ingber, D.E., Soft Lithography in Biology and Biochemistry, *Annu. Rev. Biomed. Eng.* 3, pp. 335 (2001).

32. G. M. Whitesides, Stroock, A.D., Flexible Methods For Microfluidics, *Physics Today*, pp. 42 (June 2001, 2001).

33. D. C. Duffy, J. C. McDonald, O. J. A. Schueller, G. M. Whitesides, Rapid prototyping of microfluidic systems in poly(dimethylsiloxane), *Analytical Chemistry* 70, pp. 4974 (Dec 1, 1998).

34. M. A. Unger, H. P. Chou, T. Thorsen, A. Scherer, S. R. Quake, Monolithic microfabricated valves and pumps by multilayer soft lithography, *Science* 288, pp. 113 (Apr 7, 2000).

35. T. Thorsen, S. J. Maerkl, S. R. Quake, Microfluidic large-scale integration, *Science* 298, pp. 580 (Oct 18, 2002).

36. J. W. Hong, V. Studer, G. Hang, W. F. Anderson, S. R. Quake, A nanoliter-scale nucleic acid processor with parallel architecture, *Nature Biotechnology* 22, pp. 435 (Apr, 2004).

37. B. Zhao, J. S. Moore, D. J. Beebe, Surface-directed liquid flow inside microchannels, *Science* 291, pp. 1023 (Feb 9, 2001).

38. J. Lahann, Jensen, K.F., Langer, R.S., A New Method toward Microengineered Surfaces Based on Reactive Coating, *Angewandte Chemie* 40, pp. 3166 (2001).

39. V. Linder, Verpoorte, E., Thormann, W., de Rooij, N., Sigrist, H., Surface Biopassivation of Replicated Poly(dimethylsiloxane) Microfluidic Channels and Application to Heterogeneous Immunoreaction with On-Chip Fluorescence Detection, *Anal. Chem.* 2001, pp. 4181 (2001).

40. S. Zhang, Whitesides, G.M., Rich, A., Biological surface engineering: a simple system for cell pattern formation, *Biomaterials* 20, pp. 1213 (1999).

41. A. Folch, Toner, M., Microengineering of Cellular Interactions, *Annu. Rev. Biomed. Eng.* 02, pp. 227 (2000).

42. R. Kane, Ingber, D.E., Whitesides, G.M., Patterning proteins and cells using soft lithography, *Biomaterials* 20, pp. 2363 (1999).

43. J. R. Sydor *et al.*, Chip-based analysis of protein-protein interactions by fluorescence detection and on-chip immunoprecipitation combined with mu LC-MS/MS analysis, *Analytical Chemistry* 75, pp. 6163 (Nov 15, 2003).

44. J. Moorthy *et al.*, Microfluidic tectonics platform: A colorimetric, disposable botulinum toxin enzyme-linked immunosorbent assay system, *Electrophoresis* 25, pp. 1705 (Jun, 2004).

45. J. S. Rossier, H. H. Girault, Enzyme linked immunosorbent assay on a microchip with electrochemical detection, *Lab on a Chip* 1, pp. 153 (2001).

46. A. Bernard, B. Michel, E. Delamarche, Micromosaic immunoassays, *Analytical Chemistry* 73, pp. 8 (Jan 1, 2001).

47. U. B. Nielsen, M. H. Cardone, A. J. Sinskey, G. MacBeath, P. K. Sorger, Profiling receptor tyrosine kinase activation by using Ab microarrays, *Proceedings of the National Academy of Sciences of the United States of America* 100, pp. 9330 (Aug 5, 2003).

48. U. B. Nielsen, B. H. Geierstanger, Multiplexed sandwich assays in microarray format, *Journal of Immunological Methods* 290, pp. 107 (Jul, 2004).

49. A. M. Jorgensen, K. B. Mogensen, J. P. Kutter, O. Geschke, A biochemical microdevice with an integrated chemiluminescence detector, *Sensors and Actuators B-Chemical* 90, pp. 15 (Apr 20, 2003).

50. X. Michalet *et al.*, Quantum dots for live cells, in vivo imaging, and diagnostics, *Science* 307, pp. 538 (Jan 28, 2005).

51. J. K. Jaiswal, H. Mattoussi, J. M. Mauro, S. M. Simon, Long-term multiple color imaging of live cells using quantum dot bioconjugates, *Nature Biotechnology* 21, pp. 47 (Jan, 2003).

52. A. A. Deniz *et al.*, Ratiometric single-molecule studies of freely diffusing biomolecules, *Annual Review of Physical Chemistry* 52, pp. 233 (2001).

53. K. B. Mogensen, H. Klank, J. P. Kutter, Recent developments in detection for microfluidic systems, *Electrophoresis* 25, pp. 3498 (Nov, 2004).

54. K. B. Mogensen, J. El-Ali, A. Wolff, J. P. Kutter, Integration of polymer waveguides for optical detection in microfabricated chemical analysis systems, *Applied Optics* 42, pp. 4072 (Jul 1, 2003).

55. K. B. Mogensen *et al.*, A microfluldic device with an integrated waveguide beam splitter for velocity measurements of flowing particles by Fourier transformation, *Analytical Chemistry* 75, pp. 4931 (Sep 15, 2003).

56. K. Cottier, M. Wiki, G. Voirin, H. Gao, R. E. Kunz, Label-free highly sensitive detection of (small) molecules by wavelength interrogation of integrated optical chips, *Sensors and Actuators B-Chemical* 91, pp. 241 (Jun 1, 2003).

57. M. Wiki, R. E. Kunz, Wavelength-interrogated optical sensor for biochemical applications, *Optics Letters* 25, pp. 463 (Apr 1, 2000).

58. R. L. Rich, D. G. Myszka, Advances in surface plasmon resonance biosensor analysis, *Current Opinion in Biotechnology* 11, pp. 54 (Feb, 2000).

59. M. Malmqvist, Biospecific Interaction Analysis Using Biosensor Technology, *Nature* 361, pp. 186 (Jan 14, 1993).

60. C. K. O'Sullivan, G. G. Guilbault, Commercial quartz crystal microbalances - theory and applications, *Biosensors & Bioelectronics* 14, pp. 663 (Dec, 1999).

61. E. Y. Okahata Y., Kinetic Measurements of DNA Hybridization on an Oligonucliotide-Immobilized 27-MHz Quartz Crystal Microbalance, *Analytical Chemistry* 70, pp. 1288 (1998).

62. H. Sota *et al.*, A versatile planar QCM-based sensor design for nonlabeling biomolecule detection, *Analytical Chemistry* 74, pp. 3592 (Aug 1, 2002).

63. V. N. Hung, T. Abe, P. N. Minh, M. Esashi, High-frequency one-chip multichannel quartz crystal microbalance fabricated by deep RIE, *Sensors and Actuators a-Physical* 108, pp. 91 (Nov 15, 2003).

64. C. Ziegler, Cantilever-based biosensors, *Analytical and Bioanalytical Chemistry* 379, pp. 946 (Aug, 2004).

65. R. Raiteri, M. Grattarola, H. J. Butt, P. Skladal, Micromechanical cantilever-based biosensors, *Sensors and Actuators B* 79, pp. 115 (2001).

66. A. Gupta, D. Akin, R. Bashir, Detection of bacterial cells and antibodies using surface micromachined thin silicon cantilever resonators, *Journal of Vacuum Science & Technology B* 22, pp. 2785 (Nov-Dec, 2004).

67. J. Fritz *et al.*, Translating biomolecular recognition into nanomechanics, *Science* 288, pp. 316 (Apr 14, 2000).

68. T. P. Burg, S. R. Manalis, Suspended microchannel resonators for biomolecular detection, *Applied Physics Letters* 83, pp. 2698 (Sep 29, 2003).

69. H. G. Craighead, Nanoelectromechanical systems, *Science* 290, pp. 1532 (Nov 24, 2000).

70. S. R. Quake, A. Scherer, From micro- to nanofabrication with soft materials, *Science* 290, pp. 1536 (Nov 24, 2000).

71. C. Wofsy, B. Goldstein, Effective rate models for receptors distributed in a layer above a surface: Application to cells and biacore, *Biophysical Journal* 82, pp. 1743 (Apr, 2002).

72. D. G. Myszka, X. He, M. Dembo, T. A. Morton, B. Goldstein, Extending the range of rate constants available from BIACORE: Interpreting mass transport-influenced binding data, *Biophysical Journal* 75, pp. 583 (Aug, 1998).

73. M. Furuki, J. Kameoka, H. G. Craighead, M. S. Isaacson, Surface plasmon resonance sensors utilizing microfabricated channels, *Sensors and Actuators B-Chemical* 79, pp. 63 (Sep 25, 2001).

74. H. A. Stone, A. D. Stroock, A. Ajdari, Engineering flows in small devices: Microfluidics toward a lab-on-a-chip, *Annual Review of Fluid Mechanics* 36, pp. 381 (2004).

75. R. J. Green, M. C. Davies, C. J. Roberts, S. J. B. Tendler, Competitive protein adsorption as observed by surface plasmon resonance, *Biomaterials* 20, pp. 385 (Feb, 1999).

76. H. Lu *et al.*, Microfluidic Shear Devices for Quantitative Analysis of Cell Adhesion, *Analytical Chemistry* 76, pp. 5257 (September 15, 2004).

77. P. A. Auroux, D. Iossifidis, D. R. Reyes, A. Manz, Micro total analysis systems. 2. Analytical standard operations and applications, *Analytical Chemistry* 74, pp. 2637 (Jun 15, 2002).

78. J. M. Brockman, B. P. Nelson, R. M. Corn, Surface plasmon resonance imaging measurements of ultrathin organic films, *Annual Review of Physical Chemistry* 51, pp. 41 (2000).

79. P. Schuck, Use of surface plasmon resonance to probe the equilibrium and dynamic aspects of interactions between biological macromolecules, *Annual Review of Biophysics and Biomolecular Structure* 26, pp. 541 (1997).

80. Y. Okahata *et al.*, Kinetic measurements of DNA hybridisation an an oligonucleotide-immobilized 27-MHz quartz crystal microbalance, *Analytical Chemistry* 70, pp. 1288 (Apr 1, 1998).

81. C. A. Savran, T. P. Burg, J. Fritz, S. R. Manalis, Microfabricated mechanical biosensor with inherently differential readout, *Applied Physics Letters* 83, pp. 1659 (Aug 25, 2003).

82. G. MacBeath, S. L. Schreiber, Printing proteins as microarrays for high-throughput function determination, *Science* 289, pp. 1760 (Sep 8, 2000).

83. W. M. Deen, *Analysis of Transport Phenomena* (Oxford University Press, New York, Oxford, 1998), pp.

84. L. L. H. Christensen, Theoretical analysis of protein concentration determination using biosensor technology under conditions of partial mass transport limitation, *Analytical Biochemistry* 249, pp. 153 (Jul 1, 1997).

85. R. W. Glaser, Antigen-Antibody Binding and Mass-Transport by Convection and Diffusion to a Surface - a 2-Dimensional Computer-Model of Binding and Dissociation Kinetics, *Analytical Biochemistry* 213, pp. 152 (Aug 15, 1993).

86. B. Goldstein, D. Coombs, X. Y. He, A. R. Pineda, C. Wofsy, The influence of transport on the kinetics of binding to surface receptors: application to cells and BIAcore, *Journal of Molecular Recognition* 12, pp. 293 (Sep-Oct, 1999).

87. R. A. Vijayendran, D. E. Leckband, A quantitative assessment of heterogeneity for surface-immobilized proteins, *Analytical Chemistry* 73, pp. 471 (Feb 1, 2001).

88. B. K. Lok, Y. L. Cheng, C. R. Robertson, Protein Adsorption on Crosslinked Polydimethylsiloxane Using Total Internal-Reflection Fluorescence, *Journal of Colloid and Interface Science* 91, pp. 104 (1983).

89. M. J. Madou, *Fundamentals of Microfabrication: The Science of Miniaturization* (CRC Press, Boca Raton, Fla., 2002), pp. 723.

90. J. Happel, H. Brenner, *Low Reynolds Number Hydrodynamics*. P. Hall, Ed., International Series in the physical and chemical engineering sciences (Englewood Cliffs, N.J., 1965), pp. 553.

91. N. de Mas, A. Gunther, M. A. Schmidt, K. F. Jensen, Microfabricated multiphase reactors for the selective direct fluorination of aromatics, *Industrial & Engineering Chemistry Research* 42, pp. 698 (Feb 19, 2003).

92. Z. H. Fan, D. J. Harrison, Micromachining of Capillary Electrophoresis Injectors and Separators on Glass Chips and Evaluation of Flow at Capillary Intersections, *Analytical Chemistry* 66, pp. 177 (Jan 1, 1994).

93. R. K. Shah, A. L. London, *Laminar flow forced convection in ducts*. H. J. Irvine TF, Ed., Advances in heat transfer (Academic Press, 1978), pp. 477.

94. M. B. Elowitz, M. G. Surette, P. E. Wolf, J. B. Stock, S. Leibler, Protein mobility in the cytoplasm of Escherichia coli, *Journal of Bacteriology* 181, pp. 197 (Jan, 1999).

95. R. Polzius, E. Diessel, F. F. Bier, U. Bilitewski, Real-time observation of affinity reactions using grating couplers: Determination of the detection limit and calculation of kinetic rate constants, *Analytical Biochemistry* 248, pp. 269 (Jun 1, 1997).

96. M. L. Yarmush, D. B. Patankar, D. M. Yarmush, An analysis of transport resistances in the operation of BIAcore(TM): Implications for kinetic studies of biospecific interactions, *Molecular Immunology* 33, pp. 1203 (Oct, 1996).

97. E. Papoutsakis, D. Ramkrishna, Conjugated Graetz Problems .1. General Formalism and a Class of Solid-Fluid Problems, *Chemical Engineering Science* 36, pp. 1381 (1981).

98. G. M. Brown, Heat of Mass Transfer in a Fluid in Laminar Flow in a Circular or Flat Conduit, *Aiche Journal* 6, pp. 179 (1960).

99. M. Abramowitz, I. A. Stegun, *Handbook of Mathematical Functions* (Dover Publications, New York, 1970), pp. 1046.

100. R. B. Bird, W. E. Stewart, E. N. Lightfoot, *Transport Phenomena, 2nd edition* (J.W. Wiley, 2002), pp. 895.

101. C. J. Hsu, Exact solution to entry-region laminar heat transfer with axial conduction and the boundary condition of the third kind, *Chemical Engineering Science* 23, pp. 457 (1968).

102. T. Mason, A. R. Pineda, C. Wofsy, B. Goldstein, Effective rate models for the analysis of transport-dependent biosensor data, *Mathematical Biosciences* 159, pp. 123 (Jul, 1999).

103. H. Y. Rhee, R. Aris, N. R. Amundson, *First-order partial differential equations: volume 1 and 2*, Physical and Chemical Sciences (Prentice Hall, New Jersey, 1989), pp. 540.

104. J. Cazes, R. P. W. Scott, *Chromatography Theory* (Marcel Dekker, 2002), pp. 473.

105. B. Catimel *et al.*, Kinetic analysis of the interaction between the monoclonal antibody A33 and its colonic epithelial antigen by the use of an optical biosensor - A comparison of immobilisation strategies, *Journal of Chromatography A* 776, pp. 15 (Jul 25, 1997).

106. R. P. W. Scott, *Liquid Chromatography Column Theory* (John Wiley & Sons, 1992), pp. 279.

107. T. Gervais *et al.*, paper presented at the Micro Total Analysis Systems 2005, Boston, MA 2005, accepted for publication.

108. T. P. Burg, Suspended Microchannel

Resonators for Biomolecular Detection, Massachusetts Institute of Technology (2005).

109. T. Gervais, K. F. Jensen, Mass Transport and Surface Reactions in Microfluidic Systems, *Chemical Engineering Science* Accepted for Publication (2005).

110. Y. W. Huang, V. K. Gupta, A SPR and AFM study of the effect of surface heterogeneity on adsorption of proteins, *Journal of Chemical Physics* 121, pp. 2264 (Aug 1, 2004).

111. D. Ross, T. J. Johnson, L. E. Locascio, Imaging of electroosmotic flow in plastic microchannels, *Analytical Chemistry* 73, pp. 2509 (Jun 1, 2001).

112. M. Malmsten, Ellipsometry studies of the effects of surface hydrophobicity on protein adsorption, *Colloids and Surfaces B: Biointerfaces* 3, pp. 297 (1995).

113. M. Mrksich, G. M. Whitesides, in *Poly(Ethylene Glycol).* (1997), vol. 680, pp. 361-373.

114. G. Hammes, *Thermodynamics and Kinetics for the Biological Science* (Wiley-Interscience, New York, 2000), pp. 163.

115. C. A. Savran, S. M. Knudsen, A. D. Ellington, S. R. Manalis, Micromechanical detection of proteins using aptamer-based receptor molecules, *Analytical Chemistry* 76, pp. 3194 (Jun 1, 2004).

116. T. Thundat, E. A. Wachter, S. L. Sharp, R. J. Warmack, Detection of mercury vapor using resonating microcantilevers, *Applied Physics Letters* 66, pp. 1695 (1995).

117. M. Maute *et al.*, Detection of volatile organic compounds (VOCs) with polymer-coated cantilevers, *Sensors and Actuators B* 58, pp. 505 (1999).

118. H. Sota *et al.*, A Versatile Planar QCM-Based Sensor Design for Nonlabeling Biomolecule Detection, *Analytical Chemistry* 74, pp. 3592 (2002).

119. J. K. Gimzewski, C. Gerber, E. Meyer, R. R. Schlittler, Observation of a Chemical-Reaction Using a Micromechanical Sensor, *Chemical Physics Letters* 217, pp. 589 (Jan 28, 1994).

120. S. P. Timoshenko, J. N. Goodier, *Theory of elasticity* (McGraw-Hill, ed. 3rd, 1970), pp. 567.

121. D. Sarid, *Scanning Force Microscopy: with applications to Electric, Magnetic and Atomic Forces* (Oxford University Press, New York, Oxford, ed. Revised Edition, 1994), pp. 263.

122. G. Y. Chen, R. J. Warmack, T. Thundat, D. P. Allison, A. Huang, Resonance response of scanning force microscopy cantilevers, *Review of Scientific Instruments* 65, pp. 2532 (1994).

123. T. P. Burg. (2005).

124. S. D. Senturia, *Microsystem Design* (Kluwer Academic, Boston, 2001), pp. 689.

125. J. C. Lotters, W. Olthuis, P. H. Veltink, P. Bergveld, The mechanical properties of the rubber elastic polymer polydimethylsiloxane for sensor applications, *Journal of Micromechanics and Microengineering* 7, pp. 145 (Sep, 1997).

126. A. Y. Fu, H. P. Chou, C. Spence, F. H. Arnold, S. R. Quake, An integrated microfabricated cell sorter, *Analytical Chemistry* 74, pp. 2451 (Jun 1, 2002).

127. K. Hosokawa, K. Hanada, R. Maeda, A polydimethylsiloxane (PDMS) deformable diffraction grating for monitoring of local pressure in microfluidic devices, *Journal of Micromechanics and Microengineering* 12, pp. 1 (Jan, 2002).

128. E. Delamarche, H. Schmid, B. Michel, H. Biebuyck, Stability of molded polydimethylsiloxane microstructures, *Advanced Materials* 9, pp. 741 (Jul 4, 1997).

129. C. Y. Hui, A. Jagota, Y. Y. Lin, E. J. Kramer, Constraints on microcontact printing imposed by stamp deformation, *Langmuir* 18, pp. 1394 (Feb 19, 2002).

130. S. K. Murthy, A. Sin, R. G. Tompkins, M. Toner, Effect of flow and surface conditions on human lymphocyte isolation using microfluidic chambers, *Langmuir* 20, pp. 11649 (Dec 21, 2004).

131. A. S. Kantak, B. K. Gale, Y. Lvov, S. A. Jones, Platelet function analyzer: Shear activation of platelets in microchannels, *Biomedical Microdevices* 5, pp. 207 (Sep, 2003).

132. H. Song, R. F. Ismagilov, Millisecond kinetics on a microfluidic chip using nanoliters of reagents, *Journal of the American Chemical Society* 125, pp. 14613 (Nov 26, 2003).

133. M. A. Holden, S. Kumar, A. Beskok, P. S. Cremer, Microfluidic diffusion diluter: bulging of PDMS microchannels under pressure-driven flow, *Journal of Micromechanics and Microengineering* 13, pp. 412 (May, 2003).

134. H. G. Poulos, E. H. Davis, *Elastic solutions for soil and rock mechanics*. T. W. Lambe, Ed., Series in Soil Engineering (John Wiley & sons, 1974), pp. 411.

135. M. H. Sadd, *Elasticity : theory, applications, and numerics* (Elsevier Butterworth Heinemann, Amsterdam, Boston, 2005), pp. 461.

136. T. Gervais, K. F. Jensen, Mass Transport and Surface Reactions in Microfluidics Systems, *Chemical Engineering Science* Accepted for Publication (2005).

137. T. Gervais, C. H. Tsau, J. El-Ali, S. R. Manalis, K. F. Jensen, paper presented at the 9th International Conference on Miniaturized Systems for Chemistry and Life Sciences (uTAS), Boston, MA 2005.

138. T. Gervais, J. El-Ali, A. Guenther, K. F. Jensen, Flow-Induced Deformation of Shallow Microfluidic Channels, *Lab on a Chip* Submitted for Publication (2005).

139. J. C. Venter *et al.*, The sequence of the human genome, *Science* 291, pp. 1304 (Feb 16, 2001).

140. J. Wang, G. D. Liu, M. R. Jan, Ultrasensitive electrical biosensing of proteins and DNA: Carbon-nanotube derived amplification of the recognition and transduction events, *Journal of the American Chemical Society* 126, pp. 3010 (Mar 17, 2004).

141. X. H. Gao, W. C. W. Chan, S. M. Nie, Quantum-dot nanocrystals for ultrasensitive biological labeling and multicolor optical encoding, *Journal of Biomedical Optics* 7, pp. 532 (Oct, 2002).

142. Y. Arntz *et al.*, Label-free protein assay based on a nanomechanical cantilever array, *Nanotechnology* 14, pp. 86 (Jan, 2003).

143. P. Fortina, L. J. Kricka, S. Surrey, P. Grodzinski, Nanobiotechnology: the promise and reality of new approaches to molecular recognition, *Trends in Biotechnology* 23, pp. 168 (Apr, 2005).

144. L. Graetz, Über die Wärmeleitungsfähigkeit von Flüssigkeiten, *Ann. Phys. Chem.* 1, pp. 79 (1883).

145. A. Varma, M. Morbidelli, *Mathematical Methods in Chemical Engineering* (Oxford University Press, New York, 1997), pp. 690.